A 3D PHOTONIC SENSOR-INTEGRATED TISSUE MODEL FOR STRAIN SENSING

by

Sarah J. Geiger

A dissertation submitted to the Faculty of the University of Delaware in partial fulfillment of the requirements for the degree of Doctor of Philosophy in Materials Science and Engineering

Spring 2019

A 3D PHOTONIC SENSOR-INTEGRATED TISSUE MODEL

FOR STRAIN SENSING

by

Sarah J. Geiger

Approved: _____
Darrin Pochan, Ph.D.
Chair of the Department of Materials Science and Engineering

Approved: _____
Levi Thompson, Ph.D.
Dean of the College of Engineering

Approved: _____
Douglas J. Doren, Ph.D.
Interim Vice Provost for Graduate and Professional Education

I certify that I have read this dissertation and that in my opinion it meets the academic and professional standard required by the University as a dissertation for the degree of Doctor of Philosophy.

Signed: _____

Xinqiao Jia, Ph.D.
Professor in charge of dissertation

I certify that I have read this dissertation and that in my opinion it meets the academic and professional standard required by the University as a dissertation for the degree of Doctor of Philosophy.

Signed: _____

Juejun Hu, Ph.D.
Professor in charge of dissertation

I certify that I have read this dissertation and that in my opinion it meets the academic and professional standard required by the University as a dissertation for the degree of Doctor of Philosophy.

Signed: _____

Matthew Doty, Ph.D.
Member of dissertation committee

I certify that I have read this dissertation and that in my opinion it meets the academic and professional standard required by the University as a dissertation for the degree of Doctor of Philosophy.

Signed: _____

Randall Duncan, Ph.D.
Member of dissertation committee

ACKNOWLEDGMENTS

It was difficult to comprehend the depth and breadth of the knowledge and experience that I gained over these past 6 years until I started to write it all down. Looking back on this work, I am so grateful for the contributions of all of the people whose guidance and support have led me to this achievement.

Choosing to pursue my doctorate in the Materials Science and Engineering department here at UD was one of the best choices I have made. Choosing my research project was even easier, in spite of the challenges that came with it. Dr. Juejun Hu and Dr. Xinqiao Jia have provided me with challenging work, valuable feedback, and a focused path towards graduation. Their kindness and patience through the many challenges we faced in this project were invaluable. Thank you also to my committee members, Dr. Duncan and Dr. Doty, for the invaluable advice and assistance you have provided me throughout this work. Dr. Duncan for keeping the biology in my project sound and focused, and Dr. Doty for reaching out to me personally and keeping me on track when I needed extra guidance.

My labmates created an environment of teamwork, collaboration, and mutual support that truly inspired my growth as an engineer. Very little of the work presented here would have been possible without my research partner, Jerome, who worked tirelessly to optimize the devices we needed for our project. Thank you, Jerome, for your incredible adaptability and patience, and all of the times you repeated yourself for me over Webex. Also from the Hu group, Qingyang, Tony, Lan, Hongtao, Yi,

Misha, Bin, Tian, and all the rest, thank you for your hard work and support. Qingyang, thank you for your valuable design input on the aging project, and for patiently answering all of my theoretical questions. Lan, thank you for paving the way for our project with the original flexible sensors, and thank you to both you and Hongtao for your kindness and warmth over the years. Tony, thank you for bringing me down to earth whenever I was worried and trying to learn how to pronounce "I'm starving" in Chinese with me. I hope one of us got it right.

From the Jia group, I have to thank Aidan, and also Kevin and Shuang for teaching me how to be a good fibroblast parent. The closest I had come to cell culture before this project was looking at a leaf under a microscope in 10th grade, so without you I would have been lost. Of course, I also have to thank Brad, Eric, He, Anitha, Olivia, Jiyeon, Xiaoyu, Hanyuan, Apoorva, and Anthony. Each of you has made life at UD so enjoyable, from the group dinners and potlucks to the excellent lab music choices and office conversations. Brad, I will always hear epic music whenever someone discusses interfacial polymerization, thanks to those TA videos.

Thank you also to all of the professors that I learned from in class and worked with as a TA. Dr. Zide, thank you for bearing with my messy handwriting in Quantum Mechanics, it was my favorite class. For all the professors I TA'ed 302 for: Drs. Doty, Zide, Martin, Shah, Mackay, Jia, Chase, and Johnson; and all the students I TA'ed with, thank you for letting me see the other side of the desk and connect with students through teaching and grading. I have a whole new appreciation for everything you do.

I also have to thank many staff members; Kathy, Christine, Naima, and Lisa for keeping myself and the whole department on track. I can't imagine how the department could function without such an amazing team supporting us. Charlie, thank

you for being an amazing safety officer. You make learning about all the ways to avoid dying at work as fun as that can be.

The cleanroom staff here at UD have made amazing mentors. Kjeld has been someone who I could always talk to about the challenges I was facing with my fabrication work. The UDNF staff, Cory, Iulian, Scott, Paul, and Kevin have done an amazing job of not only running a state-of-the-art facility, but also showing that they investing time in their students' projects and futures. Kevin in particular has been an amazing mentor and friend. I am not sure that I could have fully honed the skills and confidence that it took to take control of my work and plan for my career without him.

My classmates, especially both Erics, Bo, and Nicolas, thank you for your companionship as we tackled classes and choosing research groups together. It is always a bit challenging to be the only girl in a room, but you made me feel like I belonged in that office with you in our first year. Eric, thank you for being a dance nerd with me, and Bo thank you for all of the good talks. I am lucky to know you both.

Other friends in the department that I need to thank are Tess, Mike, Jimmy, Xiangyu, and Mukund. You have filled my life with so many good times that I can't possibly count them all. Even though we might be moving apart this year, I know you are always there for me (and vice versa) and that I can still look forward to our lifelong friendships.

Another group of UD friends that I need to thank are the 'Blues Hens.' The times I spent dancing with you all were the best. Especially Fiona, Bri, Clarence, Josh, Kayleigh, and Mark all of whom taught and DJed and kept the club going. We had an amazing group of people and I will always treasure those times.

I also need to thank everyone at Newark KMAI for excellent nights of training that kept me grounded and focused. Special thanks to Master Brown, who always welcomes me back to the studio no matter how long it has been. Tang Soo!

Thank you to my out-of-town friends, Heather, Julie, and Jo for always being down for a good conversation and quality time together. And thank you Amy for the amazing friendship and for giving me a home away from home in Boston with Big Kitty, Kittypants, and Mrs. Puff.

Finally, I need to thank my family. To my father, thank you for getting me used to college campuses at such a young age, challenging me with books and puzzles, and encouraging my curiosity. I am excited to become 'Dr. Geiger, II.' To my mother, thank you for teaching me to balance my life and also for filling my world with color. You showed me how powerful it is to create something the world has never seen before. To my sister, thank you for passing down your books, stuffed animals, sense of humor, and status as a True Sci Fi nerd to me. You have taught me strength, the importance of taking breaks, and have shown me how to raise an amazing child. To my nephew, thank you for making me feel like the coolest person in the world. Never stop asking questions.

The last members of my family to thank are Jin Bao (the bunny), Hey Buddy (the cat), and Bryan (the fiancé). Bryan, you have filled everyday life with warmth, calm, and love which has seen me through a lot of difficult days. Your intelligence and dedication to your work (and your cat) inspire me every day. Here at UD we have built a great foundation for our future. I can't wait to see where life takes us.

TABLE OF CONTENTS

LIST OF TABLES

LIST OF FIGURES

ABSTRACT

The study of wound healing and wound healing therapies is motivated by the need to prevent the formation of thick scar tissue in pathologically healing wounds and tissues that rely on their elasticity and modulus to perform their function, such as cardiac and vocal fold tissues. The development of *in vitro* platforms that can detect cell-induced strain in mimics of healing wounds has expanded our understanding of the mechanical, chemical, and physical cues that drive wound healing. However, these platforms are limited in their resolution, dimensionality, and ability to gather information about changes in strain throughout thick, opaque tissue models. In this work we describe the development of flexible, deterministically buckled 3D photonic device arrays that are designed and fabricated to meet the specific spatial, temporal, and strain resolution requirements needed for the detection of cell-induced strains in a millimeters-thick tissue model.

A polymer or silicone-clad $Ge_{23}Sb_7S_{70}$ chalcogenide glass resonant cavity array is selected for this application, as high-quality chalcogenide glasses devices can be deposited at low temperatures onto flexible and cytocompatible substrates. However, the reliability of these and other highly sensitive chalcogenide glass devices is affected by their aging-induced structural relaxation. The refractive index shifts resulting from this relaxation are on the same order of magnitude as the index shifts used to small-scale strain with our device arrays. In order to overcome this limitation, we develop and demonstrate a high-precision refractometry technique that tracks small changes in

the refractive index of $Ge_{23}Sb_7S_{70}$ chalcogenide glass, down to 10^{-5} RIU. This technique allows us to both identify the aging mechanism in this glass with high accuracy and compare different index stabilization methods to optimize our device processing.

The expected performance of these arrays was tested both through finite element modeling and a proof-of-concept *in vitro* experiment. In the modeling experiments, PDMS buckled geometries were deformed in cardiac graft tissue-like environments. From these experiments we showed that devices embedded in these materials could easily detect small, localized changes in stiffness theoretically caused by limited perfusion of growth factor throughout this model. *In vitro,* an SU-8 clad, symmetrically buckled device was exposed to a contracting collagen gel, and the device response as a result of this deformation was analyzed.

These deterministically buckled arrays of polymer or silicone-clad chalcogenide glass resonant cavities demonstrate sensitivity to relevant strains in 3D cell culture platforms, excellent ease of use, and the potential for a wide range of applications. This technique can be used as a standalone, low cost, plug-and-play local strain gauge for use in soft material systems. Thus, this technique's flexibility both in terms of its deformability and range of applications easily surpasses other methods of *in vitro* force or strain detection.

Chapter 1

INTRODUCTION

1.1 Wound Healing

The reduction of scar tissue is of great concern in compliant tissues whose functions rely on their mechanical properties, such as the tissue around joints, cardiac muscle, and the vocal folds. In Dupuytren's disease, excessive scar tissue forms in the hand, in some cases leading to complete immobilization of the finger joints [1, 2]. Cardiac tissue does a poor job of regenerating after cardiac arrest, in which decreased oxygenation of tissue causes widespread cell death [3-5]. The thick scar tissue that is left behind often weakens the surrounding tissue, leading to future heart injury. In the vocal fold, vocal misuse, surgery, or intubation can lead to the production of a thick scar on the otherwise very soft tissue [6, 7]. This changes the ability of the folds to vibrate to produce sound, sometimes leading to loss of voice in the patient.

The formation of a scar is the result of the activity of myofibroblasts, which are an activated form of the fibroblast; a restorative cell type responsible for maintaining the structural integrity of the extracellular matrix (ECM). In normal tissue, the ECM Is under tension from all directions. However, if a tissue is damaged, fibroblasts will sense changes in tension in their environment, as well as the release of growth factors, such as TGF-β, by macrophages in the wound. The fibroblasts' initial response to these stimuli is to invade the wound bed and fill it with ECM components including collagen [8, 9].

Collagen, along with other ECM components such as fibrin and elastin, gives our tissue its elasticity. Collagen is formed by bundles of fibrils that have a triple helix structure consisting of two or more strands of procollagen. These thick bundles of fibrils make up collagen fibers, which can then crosslink to form a fibrous, protein-rich network.

The traction forces that fibroblasts generate in order to invade the wound further stiffen the local ECM, which finally induces the differentiation of fibroblasts into myofibroblasts. Myofibroblasts develop stronger, more aligned cytoskeletal actins that enable them to actively contract tissue in order to close the wound. This contraction causes the local increases in strain and stiffness that produce a scar. Scar development, in theory, is halted when myofibroblasts no longer sense lines of tension in the now-healed wound and clear the tissue by undergoing apoptosis. However, in the case of the formation of excessively thick scar tissues, the myofibroblasts continue contracting the tissue longer than necessary [9, 8].

1.2 3D *in vitro* Tissue Models

In order to better study the physical, chemical, and biological factors that promote or deter scarring, the development of 3D *in vitro* models provides a low-cost and more easily controlled platform to do so than *in vivo* animal models. In particular, the use of artificial hydrogel tissue models is beneficial in that they allow the engineer to chemically tune the mechanical properties of the hydrogel such as stiffness and degradability, as well as introduce different cell types or biological signals. Thus, the effects of physical, biological, and chemical factors on the behavior of fibroblasts in the model can be decoupled through experimentation [10-12].

When using these platforms to study wound healing or other strained tissues, it is useful to be able to track the changes in local strain or stiffness throughout the tissue model to understand the strains or stiffness that may be the cause or result of cell activity. There are a number of methods used to detect strain or stiffness in *in vitro* tissue models, however the dimensionality, resolution, and cost of current techniques limit their usefulness.

1.3 Strain Sensing *in vitro*

1.3.1 2D Strain Detection

The detection of the strain imparted on a 2D substrate by contractile cell types such as fibroblasts has been studied for the past 40 years, starting with the use of wrinkling polymer films [13]. In these studies, cells are cultured on a soft, thin substrate such as PDMS, and the magnitude and shapes of patterns generated in the wrinkling of the film are tracked. From this method scientists developed 2D traction force microscopy (TFM), in which the deformable substrate is patterned with microns-size latex beads whose positions are tracked with microscopy [14, 15]. This method, and the subsequent advancements in 2D-TFM, allowed much higher-resolution deformation tracking as compared with wrinkling films. The culture of cells on micropillar arrays is another 2D method used to detect cell-generated forces. Micropillar substrates allow the user to control the surface area of possible cell adhesion sites by changing the diameter of the pillars [16, 17]. In deformable substrate techniques such as wrinkling films, 2D-TFM, and micropillar deflection assays, knowing the elastic properties of the substrate enables calculation of the magnitudes of the forces output by cells or cell protrusions from the local strain to the substrate.

However, in the past 12 years, 2D models have been increasingly regarded as physiologically irrelevant. The morphological characteristics of cells cultured in 2D vs. 3D are quite different, with 3D cultured cells showing more similar behavior and geometry to cells *in vivo* [18, 19]. For example, the bodies of cells in 3D tend to be more extended with narrower protrusions than cells cultured in 2D. The differences in cell geometry, number of adhesions, and size of adhesions, change the contractile behavior of these cells significantly.

1.3.2 3D Strain Detection

The best-established 3D methods of tracking strain or stiffness changes *in vitro* include collagen contraction assays and 3D traction force microscopy. In a collagen contraction assay, fibroblasts are mixed with a collagen precursor solution. As the solution gels, cells remain distributed in 3D throughout. These gels are either released from their culture wells to float or are tethered to a mechanical support [20-22]. Information about the activity of the fibroblasts is determined from the change in shape of the gel (Figure 1). Alternatively, gels can be tethered to a strain gauge to get information about the sum of cell-generated forces or strain imparted on the gel as a whole [23].

3D-TFM is the highest resolution technique for tracking cell-induced strain on a hydrogel *in vitro.* In this technique fluorescent beads are embedded in the hydrogel along with the cell culture. Then, similarly to 2D-TFM to a 3D model, tracking the changes in position of fluorescent beads distributed throughout a cell-populated hydrogel using confocal microscopy [24-26].

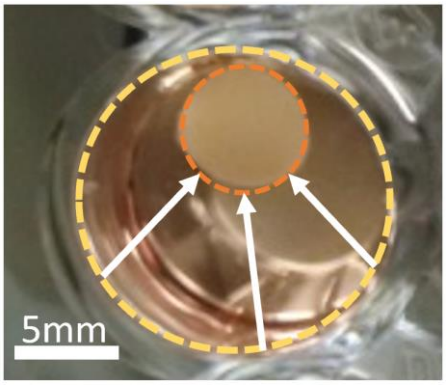

Figure 1: The change in diameter of a collagen gel from original (yellow line) to deformed (orange line) geometry gives information about the activity level of cells within the gel.

While these methods provide information about deformation in 3D *in vitro* models, they have a number of limitations. Collagen contraction assays provide only one datapoint per sample and are limited to primarily collagen as the cell scaffold material. 3D-TFM is limited by the penetration depth of confocal microscopy, which is approximately 300 μm. 3D-TFM is also best suited to studies of few or single cells, as it is very expensive and time-consuming to scan larger areas.

It is often relevant to study strain or stiffness changes throughout millimeter's thick tissue models, for example when developing a graft tissue which must have a thickness and mechanical properties similar to the damaged tissue it is replacing. Thick *in vitro* models also allow us to observe the effects of diffusion-induced gradients in the tissues that may limit the transportation of oxygen or growth factors to different points in the gel [27, 28].

Thicker tissue models also ensure that cells cultured in hydrogels held in traditional tissue culture wells are isolated from the much stiffer glass or plastic

surroundings, which may affect the amount of tension cells can generate in different regions of the tissue. Gradients or layered changes in mechanical or chemical properties of the hydrogel may also be controlled throughout the experiment in order to study how these gradients drive cell migration or other behavioral differences [29, 11].

1.3.3 Stiffness Detection

In order to map stiffness changes instead of strain, methods such as force indentation (for instance atomic force microscopy) or Magnetic Resonance Elastography (MRE) can be used on 3D *in vitro* models. Indentation methods provide information about the surface of the hydrogel and are only useful to analyze thick tissue models after the experiment has been ended and the tissue is cross-sectioned [30-32]. MRE is perhaps the only non-destructive technique that is not limited by the thickness of the model. It takes advantage of the differences in the changes of relaxation time of the nuclear magnetic resonances of water in tissue in response to magnetic pulses to determine local differences in tissue or hydrogel mechanics [33-36]. However, MRE is an extremely expensive and time-consuming technique.

1.4 Summary

Lacking is a technique which can track relevant spatial and temporal changes in local stiffness or strain in a thick *in vitro* tissue model. More specifically, an ideal platform would be non-destructive and able to track minute-by-minute changes in strain or stiffness in a several millimeters thick model. This technique must have the spatial resolution and sensitivity necessary to detect changes due to the activity of 10’s to 1000’s of cells.

In this work, a buckled photonic sensor array is developed that is sensitive to tissue-scale strain and that can be easily distributed in 3D throughout a millimeter's thick hydrogel-based tissue model. As will be demonstrated in later chapters, the resolution, dimensionality, and ease of use of our sensors are well suited for the detection of tissue-scale strain and has distinct benefits over all other techniques.

First, I discuss the motivation behind the selection of an integrated, waveguided photonic sensor platform for this application. Then I discuss the design of this device array in terms of its material choices. Then, in response to issues with device stability due to aging effects on chalcogenide glass refractive index, I discuss the development and application of a novel resonant refractometry technique capable of detecting aging-induced index changes in chalcogenide glass down to 10^{-6} refractive index units (RIU). I then show that the proposed buckled sensor array is capable of strain and stiffness detection with the appropriate spatial, temporal, and strain resolution for stiffness mapping in a Finite Element Model (FEM) of a cardiac graft tissue model. Finally, I demonstrate that this device can be used in mapping local strain in tethered, contracting collagen gels populated with neonatal dermal human fibroblasts (NDHF).

Chapter 2

PHOTONIC SENSING

2.1 Waveguided Photonics

Of great importance to the function of these devices is the use of guided wave optics to deliver light to the photonic sensing element. Guided wave optics describes the use of structures called 'waveguides' that trap and guide light as a result of transverse variations in their refractive index. The geometry of a waveguide is a fiber, slab, channel, or ridge of higher refractive index 'core' material surrounded by lower refractive index 'cladding' material. The ability of a structure to be an effective waveguide depends on the refractive index contrast between core and cladding, its width and thickness, and the wavelength of the input light. Light that is efficiently trapped and guided within a waveguide is said to propagate in the form of a 'mode'; a cross-sectional distribution of the energy profile of the wavefront (Figure 2A).

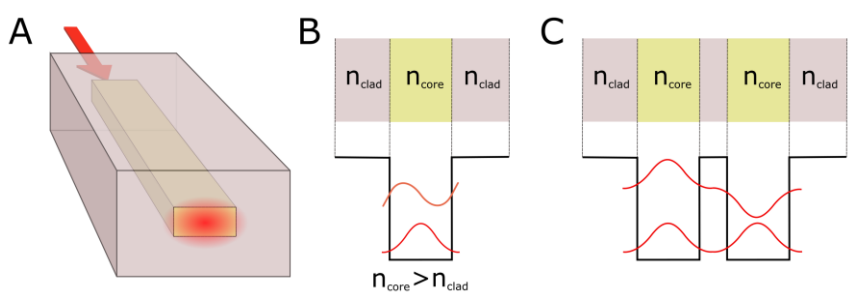

Figure 2: Schematic of A) modal confinement within a slab waveguide, B) The modeling of mode confinement as a quantum well, and C) mode coupling between waveguides.

The confinement of a mode within a waveguide can be modeled as a potential well, with the depth of the well determined by the index contrast, and with Schrodinger's equation describing the energy distribution of the mode or modes that can be trapped within the well (Figure 2B). The modes trapped within the waveguide are not perfectly confined, and so if another waveguide is brought in close enough proximity to the first, the modes may tunnel or couple between the two wells (Figure 2C). We can take advantage of this coupling to deliver light to any number of photonic structures along a waveguide.

2.1.1 Waveguide Coupling

Light can be coupled into a waveguide through a number of methods, the most common of which are butt-coupling and grating-coupling. In butt-coupling, the input optical signal is delivered to the waveguide with a lensed tip optical fiber that focuses light down to a spot on the order of the cross-sectional area of the waveguide. The sensor chip is cleaved or diced such that the cross section of the end of the waveguide is exposed with a smooth facet. The input fiber is then brought in close proximity and perpendicular to the waveguide facet, and light is coupled in directly.

Grating coupling offers significantly more flexibility in optical alignment. A grating coupler is a periodic 1D array of low and high refractive index regions patterned at the end of a waveguide. Figure 3 shows the side profile of a typical grating coupler.

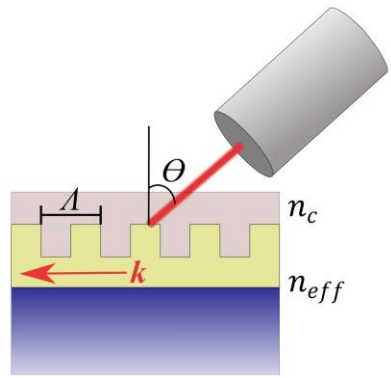

Figure 3: Side profile of an input laser source shining with incident angle Θ on a grating coupler with period Λ, effective index n_{eff}, cladding index n_c. The wavevector of the light coupled into the grating is k.

The period (Λ) of the grating is optimized for the wavelength of light it is intended to couple and the refractive indices of the grating materials. The input signal is shone downwards onto the device at an angle Θ:

$$\frac{1}{\Lambda} = \frac{n_{eff}}{\lambda} - \frac{n_c \sin\theta}{\lambda} \tag{1}$$

Where n_{eff} is the effective index of the grating, and n_c is the top cladding index.

2.2 Waveguided Photonic Sensors

2.2.1 Resonant Cavity Sensors

A resonant cavity, or resonator, is a structure in which an optical signal is enhanced by constructively interfering with itself. The simplest form of a resonator is a Fabry-Perot cavity, in which light is trapped between two imperfect reflectors. The length of this cavity and reflectivity of the boundaries dictate the wavelengths of light that can exit this cavity. In this example, the wavelength must meet the condition $\lambda = L/N$, in which L is the cavity length, and N is a modal integer. When this condition is

met, the light exiting the cavity will constructively interfere with itself, yielding a maximum in the output transmission signal.

Resonant cavity geometries of interest to our application include the Bragg cavity resonator and ring resonator. A Bragg cavity resonator is similar to a Fabry-perot cavity in that a standing wave is generated between two parallel reflectors that make up the cavity. However, in a Bragg cavity resonator, each reflector is made up of periodic layers of high and low refractive index, with a longer high-RI region in the center forming the cavity. Another version of a Bragg cavity, a 'zero-length' cavity which will be discussed further in Chapter 5, lacks the longer high-RI region in the center. This limits the number of wavelengths that can be transmitted from the cavity to, ideally, a single wavelength.

In a ring resonator, the cavity takes the form of a ring or disc. Light is coupled into and out of the ring with one or more bus waveguides and propagates around the inner circumference of the ring in a 'whispering gallery'-like mode. In this case L is the circumference of the ring. The ring resonator is in general simpler to fabricate than the Bragg cavity, which will be discussed later in this text, however the tradeoff is the significantly larger size of the ring resonator, which takes up a 2D region orders of magnitude greater than the width of the bus waveguide.

2.2.2 Sensing Theory

When applied as a sensing element, a resonator is exposed to changes in its environment that change its effective refractive index. This in turn changes the wavelengths that are trapped in or transmitted from the cavity (Figure 4).

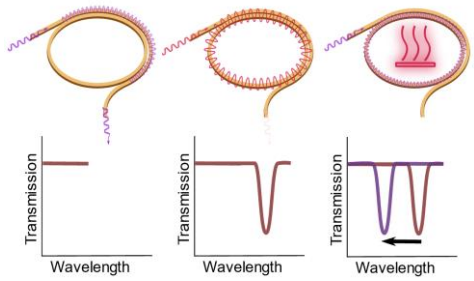

Figure 4: Schematic showing the resonant condition of a ring resonator, and the change in that condition as a result of perturbation, here due to the application of heat.

When characterizing a resonator response, we define its resonant wavelength, resonant wavelength shift, free spectral range, finesse, and quality factor.

For example, the resonant wavelength (λ_r) of a ring resonator is defined by:

$$\lambda_r = \frac{n_{eff}L}{N}, N \in Z^+ \tag{2}$$

And its change in resonant wavelength ($\Delta\lambda_r$) by:

$$\Delta\lambda_r = \frac{n_{eff}}{n_g} \cdot \lambda_r \tag{3}$$

In which n_{eff} is the modal effective index of the resonator, L the length of the cavity, and n_g the modal group index. The resonant wavelength and wavelength shift are determined experimentally as the location of peaks in the transmission spectra. The group index, or relative group velocity of light within the sensor, is calculated from the Free Spectral Range (FSR), which is experimentally determined as the spacing between resonant peaks in the transmission spectra:

$$FSR = \frac{{\lambda_r}^2}{n_g L} \tag{4}$$

The effective index, or relative phase velocity of light within the sensor, is then calculated from equation (2).

The resolution of a resonator is determined by its smallest distinguishable shift in resonant wavelength. This is in part determined by the 'sharpness' of the resonance peak, which is described by the quality factor, or Q-factor. Experimentally, the Q-factor is defined by:

$$Q = \frac{\omega_o}{\Delta\omega} \tag{5}$$

Where the ω is the width of the peak at half its extinction ratio. The higher the Q-factor, the greater the energy stored within the cavity during resonance. The Q of the resonant cavity is also dependent on the coupling efficiency of the wavelength of interest into the cavity. The Q-factor can be considered the sum of an intrinsic and extrinsic Q-factor, with the intrinsic Q_{in} determined by the quality of the cavity, and the extrinsic Q_{ex} determined by the coupling efficiency into the cavity.

$$\frac{1}{Q_{tot}} = \sum \frac{1}{Q} = \frac{1}{Q_{in}} + \frac{1}{Q_{ex}} \tag{6}$$

A cavity can also be characterized by its finesse, F, given by:

$$F = \frac{FSR}{\Delta\omega} \tag{7}$$

It is sometimes useful to distinguish between the Q-factor and F of a cavity because they different information about the loss mechanism in the cavity. In particular Q is dependent while F is independent of the cavity length.

2.3 Photonic Sensors for Strain Detection

The resonant wavelength of a resonator can be affected by a number of different conditions, including changes in temperature, exposure to radiation, and the

mechanical strain placed on the device. The relationship between resonant wavelength and temperature is linear:

$$\Delta\lambda_r = \kappa\Delta T \tag{8}$$

And may be applied in conjunction with photothermal spectroscopy, in which the optical absorption signature of molecules in close proximity to the sensor can be detected as increases in temperature at the absorption wavelengths. Exposure to radiation, for instance near-bandgap light, may induce photobleaching or darkening, which are characterized by shifts towards lower or higher refractive index, respectively, of the core waveguide material that indicate that the material is being driven towards a different thermodynamically stable state [37]. Finally, the application of strain to the bonds within the waveguide material changes its refractive index on the molecular level, leading to a linear relationship between strain and resonant wavelength. Physical strain also changes the geometry of the resonant cavity, inducing other linear changes in the effective index of the resonator [38].

Choosing the example of a ring resonator strain sensor as shown in our group's work on stretchable photonics, the change in resonant wavelength as a result of applied strain can be reduced to [39]:

$$d\lambda_r = \frac{\lambda_r}{n_g L}\int_0^{2\pi}[C_r \cdot \sigma_r(L) + C_\theta \cdot \sigma_\theta(L)] \cdot R d\theta \tag{9}$$

In which C_r and C_Θ are constants describing the material and geometric effects of tangential (Θ) and radial (r) stress on the resonant wavelength, and R is the original radius of the ring. These constants are defined as:

$$C_\theta = n_{eff}\frac{\partial\varepsilon_L}{\partial\sigma_\theta} + \frac{\partial n_{eff}}{\partial\sigma_\theta} \text{ and } C_r = n_{eff}\frac{\partial\varepsilon_L}{\partial\sigma_r} + \frac{\partial n_{eff}}{\partial\sigma_r} \tag{10}$$

The application of this theory to real-world devices shows that there is a linear relationship between increasing tensile strain on the ring and a positive wavelength shift [39].

For our application, in which we care specifically about the strain response of our resonators, it is important to decouple its strain response from the device's response to temperature, radiation, or other effects. In this case it is necessary to either have excellent control over the device environment in order to reduce large changes in temperature and illumination, or to be able to perform calibration experiments to account for those changes. Photochemical absorption can be limited by ensuring that the waveguide cladding is thick and impenetrable to gas or liquid. A key and challenging design criterium for a strain sensor is that, in order to be sensitive to strain, the device must be flexible.

2.4 Flexible Waveguided Photonics

2.4.1 Applications

Most waveguided photonic sensors are fabricated with traditional semiconductor manufacturing techniques on stiff 2D substrates. However, several flexible waveguided photonic platforms have been developed. In general, in order to make a waveguide flexible, scientists will choose to either fabricate it from all inherently flexible materials such as polymers or hydrogels or will leverage creative design criteria to flex inherently stiff materials. Besides strain detection, the development of flexible waveguided photonics is largely driven by the need for optoprobes, wearable sensors, and disposable photonics.

Optoprobes are *in vivo* light delivery systems intended for use with optogenetics or photodynamic therapy. In optogenetics, cells are modified with proteins called ‘opsins’ which can be triggered with light to induce different types of cell activity. Photodynamic therapy is the photoactivation of drugs delivered to the point of interest in diseased tissue, usually cancer. For these applications optoprobes must be able to penetrate millimeters to centimeters into living tissue without causing scarring, be flexible enough to move with the tissues they target, and deliver high power visible or NIR light to the tissue [40, 41].

Wearable photonic sensors may take the form of conformal epidermal sensors, or sensors that can be woven into clothing or worn as an accessory such as a bracelet. A wealth of electronic epidermal sensors have been developed for medical applications, for example monitoring the biological factors in sweat or tears, a patient’s heartbeat, or exposure to harmful chemicals [42]. The superior sensitivity of photonic sensors is starting to be leveraged for these applications. In particular, the stretchability required of epidermal sensors is a challenge for waveguided photonics, which will be discussed later.

Compatibility with roll-to-roll manufacturing is another major driving factor in the development of disposable flexible waveguided photonics [43-47]. Roll-to-roll manufacturing is widely used in the electronic/semiconductor device industry to mass produce solar cells and other devices on large flexible sheets to drive down product costs.

2.4.2 Materials

2.4.2.1 Inorganic Materials

In spite of their low flexibility, thin Si/SiO_2 probes are the most widely used optogenetic probes, since they have good optical confinement and can be fabricated in thin, less invasive geometries. In general, inherently stiff materials can be made flexible if machined to a few hundred nanometers thickness. While some semiconductor or glass waveguide materials may be used free-standing, they are generally leveraged in conjunction with a flexible handler or cladding material, which I will discuss in a later section [48, 40] . Many potential flexible waveguides materials exist that are much more inherently flexible and biocompatible than inorganic materials.

2.4.2.2 Hydrogels

Hydrogels are by far the most biocompatible optoprobe candidate. Hydrogels and biopolymers more closely match the chemical and mechanical properties of living tissue and so are less likely be recognized as foreign bodies to protective cell types. Hydrogels can be a good choice for implant materials because they allow local cells to invade and interact directly with the optical component. This reduces the likelihood of forming thick scar tissue around the implant that can significantly impede the penetration depth of the optical signal. However, hydrogels are especially more difficult to fabricate in smaller dimensions with low enough loss for high resolution light delivery, since their refractive index is close to that of living tissue [49, 50].

Often hydrogels can also be degraded by cells, eliminating the need for surgery to remove the implant after the therapy is completed. Hydrogel waveguides have been

fabricated from agarose and gelatin to yield biodegradable waveguides [49, 51]. PEG hydrogel waveguides have been implanted in mice to enhance insulin secretion via optogenetics [52, 53]. All-silk platforms can be made by using a silk hydrogel cladding that has been incorporated into bovine muscle [54].

2.4.2.3 Polymers

Polymer waveguide platforms are best suited for the development of low-cost wearable or disposable sensors, which can be fabricated with methods compatible with molding and stamping techniques. Photoactive acrylates or epoxies that can be bought as proprietary photoresists or adapted from known formulations are still the most popular polymeric waveguide materials as they are easily patterned using established lithography techniques and have relatively high refractive indices [45, 55-59]. Silicones such as PDMS are also popular waveguide or flexible substrate materials since they are easily molded, thermally stable, chemically inert, and biologically compatible, and as such are easy to integrate with other materials [60-64]. Alternative polymers such as paralyne C and polyimides have also been used as flexible waveguides [65].

Benefits of polymer waveguides include their inherent flexibility, low-temperature processing, and refractive index tunability. The large degree of freedom in C-C or Si-O bonds, and the variability of the degree of crosslinking allow polymers to undergo elastic deformation. Polymers can bend, stretch, and conform to 3D surfaces, making polymers an excellent choice for epidermal sensors, roll-to-roll processing techniques, and in vivo applications.

Drawbacks of the use of polymer waveguides are their lower index contrast and need for larger waveguide dimensions, which constrain their use in photonic designs such as diffractive optical elements, photonic crystals, and metamaterials [66]. These limitations can be overcome by hybridizing inorganic and organic materials in photonic structures.

2.4.2.4 Hybrid Material Platforms

In order to leverage the excellent optical properties of semiconductors and glass as well as the flexibility and biocompatibility of organic materials, the development of hybrid material platforms for flexible waveguided photonics in many cases offers the best of both worlds. The specific challenges of incorporating a stiff core material onto a softer cladding material include selecting compatible process conditions for both materials and shielding the more brittle material from excess stress.

One of the biggest challenges when selecting compatible processes for hybrid core and cladding flexible photonics platforms is the need for mechanical stability when patterning the stiffer material. Patterning techniques such as Ebeam or photolithography are often required to define the thin, low-roughness waveguides made possible by the use of inorganic core materials such as glass. Several devices have been designed that overcome this limitation by holding the flexible cladding or substrate material on a stiff substrate while patterning the core, and then releasing it [67, 68]. Conversely, a few stiff materials exist that can be transferred to flexible substrates using nanomembrane transfer techniques, stamping, or stenciling [69, 70].

In order to shield stiff materials from excess bending stress, our group and others have leveraged use of a neutral-axis design, in which thick, symmetrical top and bottom cladding materials shield the central core waveguide material from both the tensile and compressive stress imparted on the top and bottom of the bent material stack [38, 71]. In order to shield stiff waveguides from being damaged by stretching, our group has demonstrated that serpentine waveguide geometries and the patterning of stiffer islands throughout the stretchable substrate material can efficiently protect glass materials from excess strain [39].

In this work, we develop our flexible resonator arrays with a hybrid material platform, in which the cladding is made from a flexible epoxy resin, and the core is made from high-index chalcogenide glass. The processing and design choices made for the integration of these materials will also be discussed.

Chapter 3

MATERIAL SELECTION

3.1 $Ge_{23}Sb_7S_{70}$ Chalcogenide Glass

3.1.1 Optical Properties

For the core waveguide material for the flexible strain sensor array demonstrated in this thesis, $Ge_{23}Sb_7S_{70}$ (GSS) chalcogenide glass was selected. A chalcogenide glass is a solid amorphous compound consisting of sulfur, selenium, or tellurium from the chalcogen group of the periodic table. The chalcogen components are typically networked with elements such as arsenic, indium, or in our case germanium and antimony. The short-range structure of GSS is made up of long chains of sulfur, which are linked tetragonally to germanium atoms and pyramidally to antimony. GSS, as well as most chalcogenide glasses, is transparent in the NIR, with a transparency window ranging from 1000 nm to approximately 6000 nm.

This transparency window makes GSS and other ChGs particularly attractive for applications in chemical sensing, with these wavelengths able to access typical vibrations of chemical bonds. Our group has demonstrated the use of ChGs for this application. Light evanescent from the resonant cavity is absorbed by the local molecules, changing the output transmission of the cavity [72, 73].

The refractive indices of chalcogenide glasses tend to be greater than 2, greater than SiO_2 which is perhaps the most widely used NIR transparent waveguide material. Chalcogenide glasses including GSS also have high Kerr nonlinearity, meaning that

the index of the glass can be changed by interacting with high intensity light. Our group has characterized the nonlinear properties of GSS and found its nonlinear refractive index to be on the same order of magnitude as silicon, $(0.93 \pm 0.08) \times 10^{-18}$ m^2/W, with far superior two-photon absorption coefficient and propagation losses [74]. These nonlinear characteristics of chalcogenide glasses also make them promising candidates for all-optical signal processing [75, 76] and nonlinear frequency generation [77, 72, 78, 79], and may be leveraged in the patterning of waveguides using femtosecond laser writing [80-82].

3.1.2 Processing

Another major benefit of working with chalcogenide glasses are their compatibility with standard microfabrication techniques. ChGs have a wide range of state-of-the-art applications in optics and photonics. They can be easily processed into a wide range of photonic devices such as waveguides [83-92], Bragg gratings [93, 94], resonators [95-99], lenses [100-104], omnidirectional reflectors [105-107], and photonic crystals [108-111]. Our group has demonstrated the patterning of GSS and other As-based chalcogenides with photolithography, ebeam lithography, reactive ion etching, and stamping techniques.

ChGs such as GSS also have low deposition temperatures, which expand the types of processing that they can be compatible with. More specifically, thermally evaporated chalcogenide glass can be deposited on substrates at room temperature, which enables patterning on less conventional substrates such as polymers and 2-D materials. This significantly expands the use of ChGs to applications in packaging, conformal epidermal sensing, high-speed data communications, and more. In

additional to more conventional substrates such as silicon, SiO_2, and CaF_2 [95, 112, 97, 110, 113], our group has patterned GSS on substrates such as polyimide, PDMS, and photoresists for applications in flexible and stretchable photonics [114, 38, 115].

We select GSS as our waveguide core material for our application for its high refractive index and low temperature processing. It is key for our application to encase our sensors in flexible and cytocompatible polymer materials. Most polymers have refractive indices between 1 and 2, therefore the selection of a glass with a higher RI allows for good optical confinement within the waveguides in the device array and minimizes insertion loss into the material. Polymers have glass transition temperatures on the order of less than 200 °C, therefore the selection of a glass that can be deposited at lower temperatures is necessary. In our studies we select SU-8 epoxy resin or PDMS silicone as our flexible cladding material.

3.2 SU8 Photoresist

3.2.1 Material Properties

SU8 is an epoxy-based photoresist consisting of tetramers of bisphenol A novolac epoxy suspended in a solution of cyclopentanone and triarylsulfonium hexafluroantimonate salt. As with most photoresists, SU-8 is deposited by spin coating at speeds on the order of 1000 rpm. A baking step then removes excess solvent from the resist. This resist is patterned by select exposure to UV light or electron beam, which converts the salt to an acid that opens the epoxy rings, which then crosslink. The un-crosslinked resist can be dissolved away.

SU8 is a well-established resist developed by IBM in 1989. It is highly impervious to liquids. After crosslinking, its Young's modulus is approximately 4.02

GPa. Depending on the formulation and process conditions, SU8 can be coated and patterned at thicknesses from hundreds of nanometers to hundreds of microns at high aspect ratios. These mechanical properties have made SU8 well-suited for a number of MEMs, molding, and other structural component applications. With a refractive index of 1.57, it has itself been utilized as waveguide optical components as well as cladding material for a number of photonics applications.

3.2.2 Cytocompatibility

The cytocompatibility of SU8 is well-established in the literature. In order to confirm that SU8 coated photonics are equally cytocompatible, we performed a cytotoxicity study of a sol-gel processed TiO_2 sensor by culturing human mesenchymal stem cells (hMSCs) both in conformal contact with the sensor materials, and nonconformal contact [116].

In this study, Thin films of TiO_2 were deposited on bare silicon wafer via the sol-gel process. SU-8 2002 photoresist was spin coated on select samples to simulate sensor encapsulation in SU8. The samples were then cleaved and suspended in cell culture inserts above hMSCs cultured in a 12-well plate. Bare silicon wafer was also included in the study as an additional test substrate. Three chips of each sample were included in the study, and three empty trans-well membranes were included in control wells.

Bone marrow-derived hMSCs (Lonza) were seeded in a 12-well plate at a seeding density of 5,000 cells/cm^2, and precultured for 2 days before adding the sensor materials to the trans-well membranes (Millipore, 0.4 μm pore size). All hMSCs used in these experiments were passage 6. Media (mesenchymal stem cell

maintenance media, Lonza) was changed every two days. As shown in Figure 5, hMSCs proliferated over the following six days of the study, after which the cell monolayer became confluent, prohibiting further cell growth.

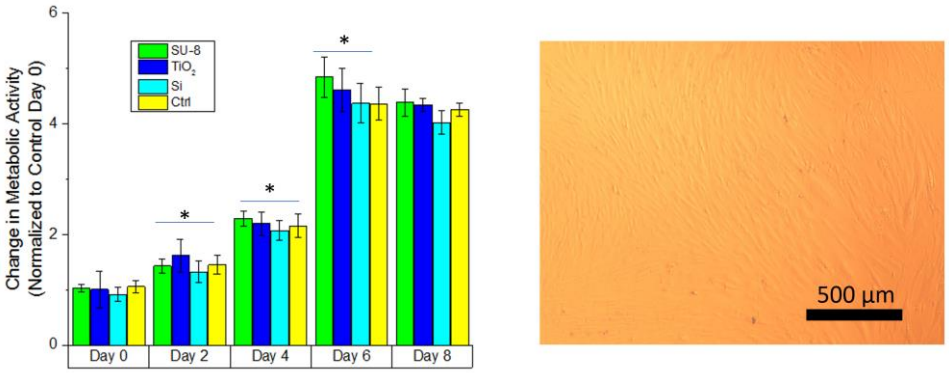

Figure 5: Plot: Change in metabolic activity of hMSCs in nonconformal contact with sensor materials over 8 days. No statistically significant difference in metabolic activity between the different groups was observed on any given day. Statistically significant increase in metabolic activity was observed in all groups on Days 2-6. Image: hMSCs on Day 8 showing confluence in the well below the trans-well membrane containing TiO_2-coated wafer

On each day, no statistically significant difference was found between test samples and control groups. The metabolic activity of hMSCs increased significantly ($p < 0.01$) after the culture was initiated until cells reached confluence. By day 8, the average number of cells in all testing groups increased by approximately four folds from day 0, confirming that the SU-8 and TiO_2 films did not compromise the proliferative potential of hMSCs.

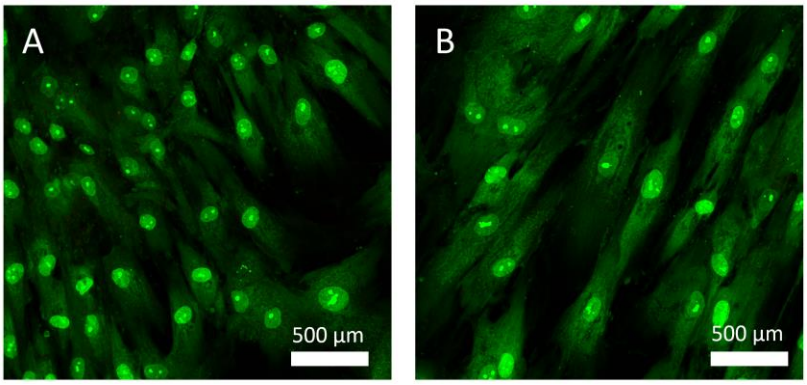

Figure 6: Results of live/dead staining hMSCs after 10 days in conformal contact with sensor materials. A) Results of this staining of cells cultured on a SU8-clad TiO_2-coated silicon wafer. B) Cells cultured on top of TiO_2-coated silicon.

In this experiment, chips of sensor materials 0.36 cm^2 were placed in the bottom of a cell culture well. 50 µL suspensions of 20,000 hMSCs each were pipetted on top of the wafers, and then incubated for 2 hours to allow cells to attach before additional media was added. After 10 days cells were washed with PBS and a solution of SYTO13 (live) and propidium iodide (dead) was used to perform a live/dead assay. The results were imaged with an LSM 710 confocal microscope (Figure 6). From these results we observe that hMSCs plated directly on the sensor materials attached, adopted a spindle-shaped morphology and maintained a high viability with little to no cell death. Collectively, our results confirmed the cytocompatibility of our sensor materials.

3.3 PDMS

3.3.1 Material Properties

PDMS, or polydimethyl siloxane is an elastomeric silicone with a Si-O backbone bearing methyl or vinyl groups bound to the in-chain and terminal silicon. In the standard proprietary formulation, Sylgard 184, a base agent of primarily dimethyvinyl terminated dimethyl siloxane is crosslinked with a curing agent containing dimethyl methylhydrogen siloxane and a platinum catalyst, among other components, typically in a 10:1 ratio[117]. Curing at room temperature is slow, and the PDMS can be degassed and/or processed by spin coating or other methods before accelerating the cure with a baking step. PDMS can be spin cast at thicknesses from few microns to millimeters [39, 118]. Depending on the base to curing agent ratio and curing temperature, the elastic modulus of PDMS can range from slightly less than 1MPa to a few MPa [118, 30]. Its refractive index ranges from approximately 1.44 at visible wavelengths to 1.42 at telecom wavelengths [119].

3.3.2 Cytocompatibility

The cytocompatibility of PDMS is well-established, and is widely applied in implants, cell culture systems. It is considered a cytocompatibility ‘control’ by the National Heart, Lung, and Blood Institute. The surface chemistry of PDMS can be altered with plasma treatments in order to control cell adhesion or the adsorption of proteins to its surface for applications in cell culture [120].

3.4 ChG-polymer photonics

Our group has previously leveraged the mechanical and optical properties of GSS ChG and SU8 photoresist in hybrid platforms for a number of photonics

applications. Besides applying SU8 as a cladding material for many of our group's planar devices, the Hu group has also used SU8 to pattern stiff regions to hold devices on stretchable PDMS substrates, and as a part of a multilayer device stack with polyimide to minimize strain in a bendable photonic chip [38, 39]. In this work, we utilize SU8 for its low index, cytocompatibility, liquid-resistance, and flexibility to both clad and provide mechanical support for our proof-of-concept GSS resonator strain sensors. In Chapter 6, we demonstrate the alternate use of PDMS as the cladding material for our devices in Finite Element Models of our buckled structures, and further propose modifying our waveguide geometry to account for the increased flexibility and stretchability.

Chapter 4

DEVICE STABILITY

As discussed previously, a number of conditions besides strain can affect the resonant condition of a cavity, unless calibrated for or accounted for in the device design. Besides these conditions, ChG also experiences sub-T_g structural relaxation. This relaxation changes the refractive index of the glass on the order of the sensitivity of our devices, which can be misinterpreted as a false signal. In this section I will demonstrate a resonant cavity refractometry technique capable of detecting refractive index changes down to 10^{-6} RIU. This study reveals that the refractive index change of the glass due to aging tends to follow stretched exponential behavior, with stretch exponents and rate of index change dependent on initial glass treatment. Thermally annealed devices show the best stability, suggesting that thermal annealing is the appropriate post-deposition treatment method for obtaining stable ChG films.

4.1 Glass Aging

Glasses are inherently thermodynamically metastable. The thermodynamic instability and excess free enthalpy of glasses below their glass transition temperature (T_g) leads to physical aging effects over time as the glass structure relaxes towards a more thermodynamically stable state [121-124]. Concurrent with glass aging are changes to the structural, mechanical, thermal and optical properties of glasses, and thus understanding the aging process is essential to both fundamental glass science and practical applications involving glass materials. The earliest observation of glass

aging was measured by Joule, who tracked the zero-point displacement of a thermometer over time [125]. Today, physical aging of glasses is traditionally measured by tracking changes in enthalpy loss or fictive temperature of the glass using differential scanning calorimetry (DSC), with experiments often spanning decades. These experiments have shown that enthalpy relaxation proceeds by a stretch exponential (Kohlrausch) function defined by a Kohlrausch exponent, β, with the form:

$$e^{-(\frac{t}{\tau})^{\beta}} \tag{11}$$

Values of β for glass materials tend to fall on or near select 'magic numbers' that correspond with the axiomatic Phillips fields-free diffusion-to-traps model of structural relaxation, initially derived from charge diffusion experiments [126, 127]. These magic numbers are predicted theoretically by assuming that the structural relaxation mechanism is dependent on the effective dimensionality (d) of the configuration space in which the diffusion occurs:

$$\beta = \frac{d}{d+2} \tag{12}$$

Of particular interest for network glasses are β = 3/5 and β = 3/7. β = 3/5 corresponds to a system where d = 3, undergoing structural relaxation dominated by short-range forces, while β = 3/7 corresponds to d = 3/2, signals a system dominated by a mixture of short and long-range forces. In chalcogenide glass short range forces are said to indicate relaxation between covalent bonds, while a mixture of short- and long-range forces indicate interchain relaxation of the glass [126, 128, 129].

4.2 ChG Aging

4.2.1 Aging Mechanisms

ChGs are known for their large capacity for compositional alloying. This unique attribute allows continuous modification of their network structures and thus presents them as an ideal system for investigating the impact of network topology on physical aging [130]. Constraint within the glass matrix is typically quantified by the number of Lagrangian constraints per atom (n_c), with the ideally constrained ChG matrix having $n_c = 3$. This is related to the average coordination number, Z, bonds per atom, with a critically constrained ChG matrix having Z = 2.4. Above Z = 2.4, the glass network is over-constrained and aging effects are less energetically favorable. Below Z = 2.4, aging can proceed at ambient conditions at expedited rates, making these glass materials unsuitable for applications where material stability is necessary [131-133].

In addition, the relatively weak chemical bonding between chalcogens and other atoms as compared to those in oxide glasses implies that aging of ChG is strongly dependent on the processing history and storage conditions of the glass. For instance, exposure to light near the bandgap of the glass causes photobleaching (or photodarkening) and light-assisted aging [37]. Annealing below the glass transition temperature (Tg) allows them to settle to a more thermodynamically favorable state [134, 132, 37, 135]. Exposure to air leads to water absorption or oxide formation on the surface of the glass [136-139]. Therefore, understanding the interplay between glass processing and aging kinetics is an important topic for ChGs.

4.2.2 Previous Aging Experiments

Despite the recognized importance of understanding and quantifying the aging process in ChGs (as well as other optical glasses), few experiments have directly tracked the optical property evolution of glasses over time. A main technical challenge lies in the small magnitude of the changes. Changes of the real part of the refractive indices due to aging are usually in the order of 10^{-3} to 10^{-4} (refractive index unit or RIU), comparable to the resolution of classical thin film optical measurement techniques such as ellipsometry or prism coupling. Moreover, the relaxation of some glasses can take decades to stabilize. The result of this is the limited set of optical aging measurements reported in literature. Many involve scattered optical measurements spaced out over years in order to observe any significant changes with these techniques [133, 134, 140, 141]. The limited resolution also excludes precise quantification of the aging kinetics. Furthermore, the reported measurements were performed on films exposed to environmental conditions that do not mirror the storage and geometry of real ChG devices.

One commonly adopted procedure enabling the study of slow material (or device) aging or degrading processes within an acceptable timeframe is accelerated aging test, where the kinetics of the process is expedited by exposing the subject material to elevated temperatures. Glass aging follows non-Arrhenius behavior below Tg, and thus at different temperatures different thermodynamically stable states of the glass are accessed and the selection of an appropriate aging temperature is not straightforward [142-146]. In actual photonic devices where ChGs are inevitably used alongside other materials, the situation is further complicated as heat treatment can

result in significant thermal stress which further modifies the equilibrium states the glass relax towards at different temperatures [147].

4.3 Novel Experiment Design

Here we quantified the aging kinetics of ChG thin films and its dependence on processing conditions using resonant cavity refractometry [112, 95]. In resonant cavity refractometry, the changes in the optical characteristics of a cavity are tracked via its resonant wavelength shift. Previous resonant cavity refractometry techniques track the optical changes of a single cavity over time, in most cases describing only the stability of the resonator as a whole and not capturing the changes in the cavity material itself [93, 148]. Prior work on resonant cavity refractometry investigated photosensitivity in ChG-based resonators, which indicates a photosensitive refractive index change in the order of 10^{-2}. The approach used, however, is not adequately precise for aging studies as aging of cladding materials can also contribute to resonance drift and interfere with the refractive index change quantification [95].

In this technique, tiny refractive index changes in a ChG are monitored through tracking the resonant wavelength shifts of optical cavity arrays of four ChG devices. Each array undergoes different processing conditions before aging is tracked. Since the resonant wavelength of an optical cavity with high quality factor (Q-factor) can be determined with picometer-level accuracy, the technique features exceptional resolution to refractive index changes (down to 10^{-5} RIU and below [95, 112]) ideal for probing the kinetics of aging processes. Furthermore, the technique also measures aging of ChG when the material is deployed in a functional photonic device and therefore the results are immediately relevant to device applications based on ChGs.

4.4 Experimental Details

In this study, we chose $Ge_{23}Sb_7S_{70}$ (GSS, bulk composition) as our model system since it is relevant to our application. Its average coordination number is Z = 2.53, thus the network should be somewhat overconstrained and age slowly. It has a Tg of 311°C [149], much higher than common As-based ChGs (the Tg's of As_2S_3 and $As_{40}Se_{60}$ are 210°C and 187°C [150, 137], respectively), which implies reduced aging at room temperature essential for practical device applications. The refractive index of thermally evaporated GSS is approximately 2.22 at 1550nm, and the expected composition post-evaporation is $Ge_{23}Sb_{11}S_{66}$ [151]. Fig. 9(A) schematically illustrates the layout of the micro-ring cavity device used for refractometry measurements.

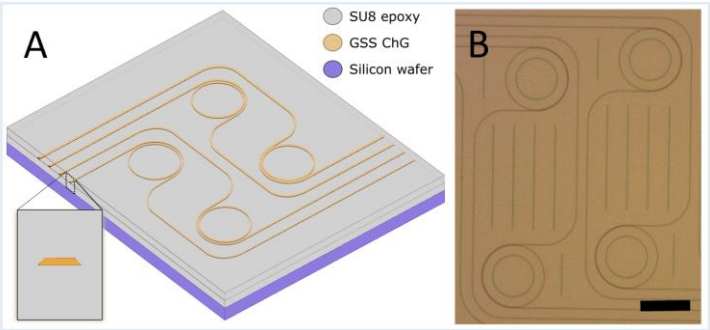

Figure 7: A) 3D perspective drawing of the device arrays used in this experiment. B) Optical microscope image of the device chip (Scale bar 300 µm). Reprinted with permission from ref [152], Optics Materials Express.

4.4.1 Fabrication

The waveguides and micro-ring resonators were fabricated using electron beam lithography and a lift-off technique [153]. We select lift-off over etching because lift-off yields a pristine glass surface without excess materials (e.g. fluorine

sidewall coatings [96]) that can complicate the analysis. First, a silicon wafer coated with 150 nm oxide was cleaned in Nanostrip 2X® at 80 °C for 5 minutes and rinsed thoroughly in DI water. The wafer was then treated for 30 s with oxygen plasma to improve SU-8 adhesion. 2 µm of SU-8 was spin cast onto the wafer as the bottom cladding layer and soft-baked for 1 minute at 95 °C. This layer was then exposed to 100 mW/cm^2 UV using a Neutronix-Quintel NXQ8006 mask aligner and baked for an additional 150 s at 95 °C. Additional lines were patterned in the regions between devices to aid liftoff, as seen in Fig. 7(B). Next, 500 nm of LOR 5A liftoff resist was spin cast on top of the SU-8 under-cladding and baked for 5 minutes at 150 °C. This was followed by 280 nm of CSAR ARP-6200.09, baked for another 5 minutes at 150 °C. Following electron beam patterning with a Vistec EBPG5200ES, the CSAR resist was developed for 60 s in AR-600-546 developer. The exposed LOR was developed for approximately 35 s to realize a good undercut profile. 250 nm thick GSS was deposited onto the device pattern via thermal evaporation, and the remaining resist and excess glass were lifted off in NMP at 75 °C for approximately 2 minutes. Another 2 µm layer of SU-8 was spun and crosslinked as a top cladding layer using the methods described previously.

We specifically design the waveguide to be symmetrically cladded with SU-8 epoxy to serve two purposes. We have experimentally proven that SU-8 acts as an excellent barrier to moisture in the ambient environment, thereby preventing humidity change from interfering with the measurement. More importantly, as the symmetric waveguide only consists of two materials, ChG and SU-8, we can readily isolate the index change induced by the ChG core.

4.4.2 Resonant Cavity Refractometery Theory

Confinement factors in the ChG core (Γ_{ChG}) and SU-8 cladding (Γ_{SU8}) change with varying waveguide widths and the corresponding resonant wavelength shift ($\Delta\lambda_r$) is given by:

$$\Delta\lambda_r = \frac{\Gamma_{ChG} \times \Delta n_{ChG} + \Gamma_{SU8} \times \Delta n_{SU8}}{n_g} \times \lambda_r \tag{13}$$

Where n is the index of the waveguide core (ChG) or cladding (SU8) and n_g is the group index, given by:

$$n_g = \frac{{\lambda_r}^2}{FSR \times L} \tag{14}$$

where FSR, or Free Spectral Range, of the resonator corresponds to resonant peak spacing in the wavelength domain, and L is the length of the resonant cavity.

Here we take advantage of the linear relationship between the confinement factor and effective index change of the waveguide mode in order to extrapolate the index change of the glass itself. The core and cladding confinement factors for TE and TM modes in each waveguide geometry were determined by FDTD simulations, shown in Fig. 10. The waveguide profiles analyzed are extracted from SEM images of true device cross-sections. Sidewall angles were approximately 65°.

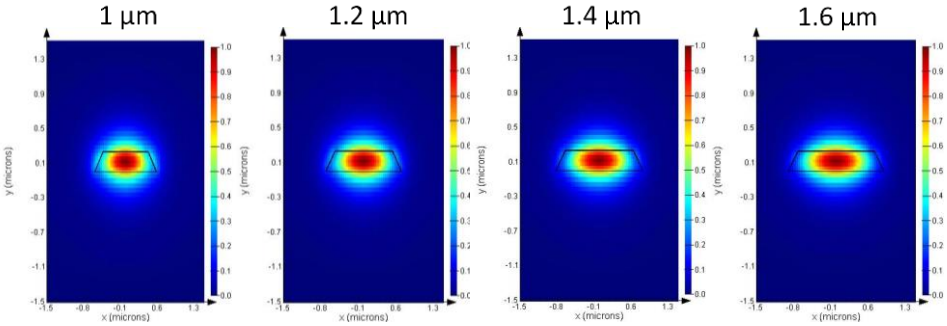

Figure 8: TE mode profiles for each waveguide simulated with FDTD. The labeled widths are the approximate width of each waveguide at ½ its thickness. Reprinted with permission from ref [152], Optics Materials Express.

Here we define the normalized confinement factor in the ChG core as:

$$\Gamma_{norm} = \frac{\Gamma_{ChG}}{\Gamma_{ChG}+\Gamma_{SU8}} \tag{15}$$

These values are shown in Fig. 11. Small differences in the waveguide profile geometry due to variations in the liftoff resist profile led to the error shown in the average confinement factor.

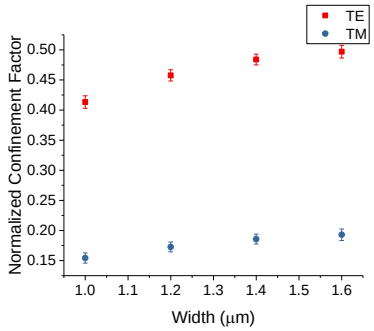

Figure 9: Average calculated normalized confinement factor for each waveguide width and polarization. Reprinted with permission from ref [152], Optics Materials Express.

We note that $\Gamma_{ChG} + \Gamma_{SU8}$ is a function of waveguide width and in general does not equal to unity due to the slow light effect [154]. Eq. 3 then can be re-written as:

$$\frac{n_g}{\lambda_r} \cdot \frac{\Delta\lambda_r}{\Gamma_{ChG} + \Gamma_{SU8}} = \Gamma_{norm} \times \Delta n_{ChG} + (1 - \Gamma_{norm}) \times \Delta n_{SU8}$$
$$= (\Delta n_{ChG} - \Delta n_{SU8}) \times \Gamma_{norm} + \Delta n_{SU8} \quad (16)$$

The equation indicates that for each waveguide width, $\frac{\Delta\lambda_r}{\Gamma_{ChG}+\Gamma_{SU8}}$ linearly scales with Γ_{norm} of the waveguide. By plotting $\frac{\Delta\lambda_r}{\Gamma_{ChG}+\Gamma_{SU8}}$ versus the normalized confinement factor, we can therefore extrapolate the refractive index change of the ChG core at $\Gamma_{norm} = 1$.

4.4.3 Measurement Setup

In this study, we track the aging of three groups of devices, each patterned on one chip with identical fabrication protocols but treated with unique initial conditions. The devices were covered with thick opaque tape (Scotch 'Super 33+' Vinyl Electrical Tape) throughout the aging measurements in order to isolate the observed aging effects from photobleaching of the GSS glass [155]. One group of devices was photo-saturated under a broadband halogen lamp used for microscope illumination for 96 hours with a power flux of 4.45 mW/cm2, determined at 635 nm with a thermal power meter, before covering the device chip with tape and starting aging measurements. The refractive index change of ChG in this group was also tracked during photo-saturation. The next group was covered and measured immediately after cladding, receiving no additional treatment before beginning the study. The final device group was covered

immediately and annealed for two hours at 130 °C before beginning aging measurements.

In order to isolate the aging-induced index change from thermal effects, temperature dependent wavelength shifts (TDWS) of ChG resonators with different waveguide widths were determined on a separate set of calibration devices with identical configurations. The device chip was placed on a temperature-controlled stage, and the peak shift was measured at multiple temperatures between 18 °C and 25 °C. The device was left to stabilize for one hour at each temperature before measurement. We also made sure that index drift resulting from aging during the entire experiment was much smaller than the measured thermo-optic index change. As an example, the temperature-dependent resonant wavelength shifts (TDWS) of each measured calibration device are plotted in Fig. 12. The average TDWS was -0.072 ± 0.005 nm/°C for the TE device modes and -0.150 ± 0.009 nm/°C for the TM device modes. The data point to thermo-optic coefficients of (6.16 ± 0.59) × 10^{-5} /°C for GSS and -(2.13 ± 0.14) × 10^{-4} /°C for SU-8, on the same order of magnitude as prior reports [156, 157, 97].

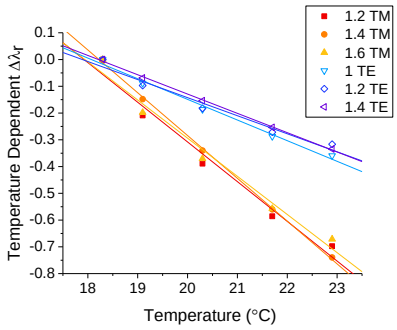

Figure 10: TDWS of each calibration device with respect to room temperature (18.3 °C). Reprinted with permission from ref [152], Optics Materials Express.

During aging measurements, the temperature of the stage at each measurement is recorded. In our data analysis, we compensate for the temperature response of each device using the measured TDWS of the calibration device with the same geometry.

4.5 Results

During photo-saturation, TE and TM mode confinement factors from four devices with varying widths were analyzed per measurement, calculated from resonant peaks near 1570 nm. The changes in the devices' effective indices versus confinement factors is plotted in Fig. 13(A). The calculated Δn_{ChG} versus exposure dose, extrapolated from the intersection of each best fit line with the $\Gamma_{norm} = 1.0$ axis, is plotted in Fig. 13(B). The error bars in Fig. 11(B) and Figs. 12 through 14 indicate the standard deviation of the calculated $\Gamma_{norm} = 1.0$ intercept with the $\frac{n_g}{\lambda_r} \cdot \frac{\Delta\lambda_r}{\Gamma_{ChG}+\Gamma_{SU8}}$ axis. During photo-saturation, the effective index of the GSS decreased and was well fit with a stretch exponential function with a β of 0.495 ± 0.017. The rate constant of this relaxation was a dose of 560 ± 51.1 J/cm2, which corresponded to approximately 36 hours of photo-saturation. This stretch exponent is also in keeping with a similar study done by Knotek et al. on $Ge_{24.9}Sb_{11.6}S_{63.5}$ in which the β = 0.45 for films exposed to several different light intensities at 532 nm [93]. The limit of this fit equation as dose approaches infinity was -(4.596 +/- 0.137) × 10^{-2} RIU.

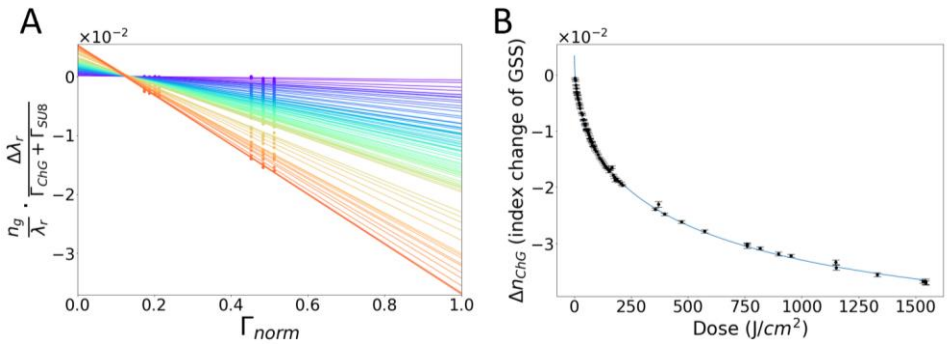

Figure 11: A) Change in left-hand-side of Eq. 16 versus normalized confinement factor (defined by Eq. 15) during photo-saturation. Data in purple is fit from the earliest time point and red corresponds to the last measurement taken. B) The change in GSS refractive index vs exposure dose of broadband light. Reprinted with permission from ref [152], Optics Materials Express.

During the aging study of the photo-saturated device, the effective index increased instead of decreased, and changed at a much lower rate than during photo-saturation. Aging of this device was tracked for 32 days. The results, shown in Fig. 14, were best fit by a stretch exponential with $\beta = 0.685 \pm 0.064$ and $\tau c = 12.4 \pm 2.2$ days. The maximal value of the index change as determined by the limit of the stretch exponential fit was $(1.335 +/- 0.095) \times 10^{-3}$ RIU.

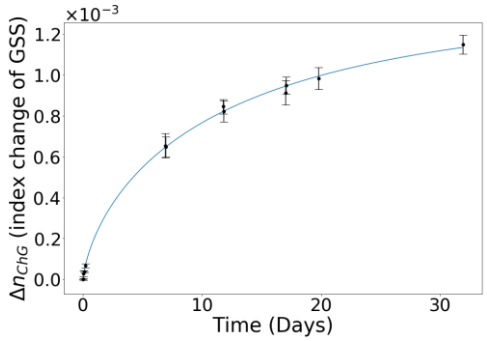

Figure 12: Refractive index change of GSS as a function of time during aging of photo-saturated devices. Reprinted with permission from ref [152], Optics Materials Express.

The sample that underwent no annealing or photo-saturation prior to beginning the aging study showed the most rapid decrease in Δn_{ChG} during aging. This data, shown in Fig. 15, was fit best by a stretch exponential function with $\tau_c = 32.5 \pm 3.0$ days and $\beta = 0.653 \pm 0.027$. The limit of the refractive index change for this sample was calculated to be -(8.428 +/-0.248) × 10^{-3} RIU.

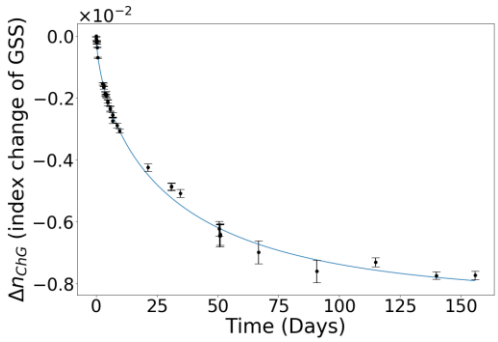

Figure 13: Refractive index change of GSS as a function of time during aging of untreated devices. Reprinted with permission from ref [152], Optics Materials Express.

In Fig. 16, we observe that the annealed sample showed the smallest change in Δn_{ChG} vs time of all three samples. Over the 18-day time course of this experiment, the data was best fit by an exponential fit instead of a stretch exponential, with $\tau_c = 1.42 \pm 0.25$ days. The limit of index change for this sample was -(1.731 +/- 0.094) × 10^{-4} RIU.

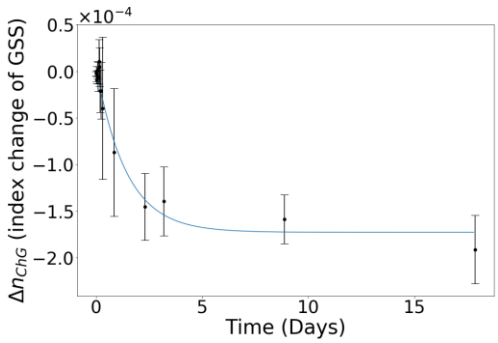

Figure 14: Refractive index change of GSS as a function of time during aging of annealed devices. Reprinted with permission from ref [152], Optics Materials Express.

4.6 Discussion

Overall, aging behavior of both devices that did not undergo heat treatment had stretch coefficients between 0.65 and 0.7, closest to the stretch exponent of 0.6 which indicates structural relaxation driven by short range forces. This is consistent with a previous report by Knotek et al., who studied aging-induced shifts in the optical bandgap of a $Ge_{24.9}Sb_{11.6}S_{63.5}$ based glass with similar composition [136]

During photo-saturation, the stretch coefficient was closer to $\beta = 0.43$, which would indicate a mixture of short and long-range forces driving index change. The result also suggests that light illumination can produce a structural state significantly

different from that in thermally treated but unexposed glasses. Photobleaching, the typical result of exposing many Ge-based ChGs to near-bandgap light, occurred as indicated by the decrease in refractive index. However, the increase in refractive index during aging of this device is somewhat unexpected. The origin of the index increase will be a subject for future studies.

The results from the annealed film are not fit well by a stretch exponential function. This is possibly because the magnitude of the error relative to the glass index change is quite large, with error in many measurements comparable to the index shift. Overall this device had the minimum predicted index change, approximately an order of magnitude less than that of the photo-saturated device.

These studies were all continued past the time frame reported in this report, and further decrease in n_{eff} was observed for the annealed device, however we chose to omit these data points because we observed significant discontinuities in the aging behavior of all three device arrays after a prolonged spike in the storage temperature of the samples. In general, the standard deviation in the calculated $\Gamma_{norm} = 1.0$ intercept for all studies tended to increase over time. For example, calculated error in the ΔnChG of the annealed device for early timepoints was as low as 2.5×10^{-6}, while towards the end of the study the error ranged from 3 to 8×10^{-5}.

4.7 Summary

In summary, the change in GSS index over time of the photo-saturated and untreated devices reported in this letter showed good agreement with the Phillips-free axiomatic diffusion to traps model of relaxation, with β values indicating structural relaxation proceeding in response to short range forces within the glass. Photo-

saturation of GSS may occur by a somewhat different mechanism, as its β-value is closer to 0.49. The thermally annealed glass exhibits the smallest index drift in the order of 10^{-4}, suggesting that proper heat treatment is the preferred method to stabilize the optical response of ChG devices. The study shows that resonant cavity refractometry can be used as a precise method to extract the aging kinetics of ChG over a relatively short time frame. In addition to shedding light on the aging mechanism, the results also establish the baseline aging behavior of glass undergoing different processing conditions critical for practical photonic device applications based on these materials.

Chapter 5

DEVICE DESIGN

In the previous chapters we showed that flexible SU8 or PDMS-clad GSS ChG photonic resonators can be applied in cytocompatible configurations with good optical performance, and that the aging-induced refractive index changes in their materials can be stabilized with annealing. In order to apply these sensors to detect *in vitro* tissue-scale strain, we deterministically design the device array geometry, resonator characteristics, and measurement method to capture minute-to-minute changes in local strains imparted on a mm's thick hydrogel tissue model by groups of 10s-1000's of contractile cells. The fabrication of a proof-of-concept device is then demonstrated.

5.1 Target Resolution

From both single-cell 3D TFM and whole collagen gel contraction studies we see that, typically, the amount of force output by a single contractile cell is on the order of 100's of pN to 10's of nN [25, 23, 158, 159]. The niche in resolution that we refer to as 'tissue-scale' is the detection of the activity of 10's of cells or more. Therefore, in this study our target force resolution is a few nN's to μN's. Since the typical cell body of contractile cell types is on the order of a few 10's of microns in diameter, we choose the ideal spatial resolution, or measurement spacing, to be between 100 μm and 1 mm spacing of measurements in X, Y, and Z throughout a tissue model. We aim to perform measurements with a minute-by-minute frequency, a timescale comparable to other in vitro strain detection techniques.

5.2 2D Array Geometry

We design a device array that can be patterned with traditional photo- and e-beam lithography techniques on a 2D substrate before distributing the devices in three dimensions by buckling. In Fig. 15(A) is a bird's eye view of the proposed sensor chip.

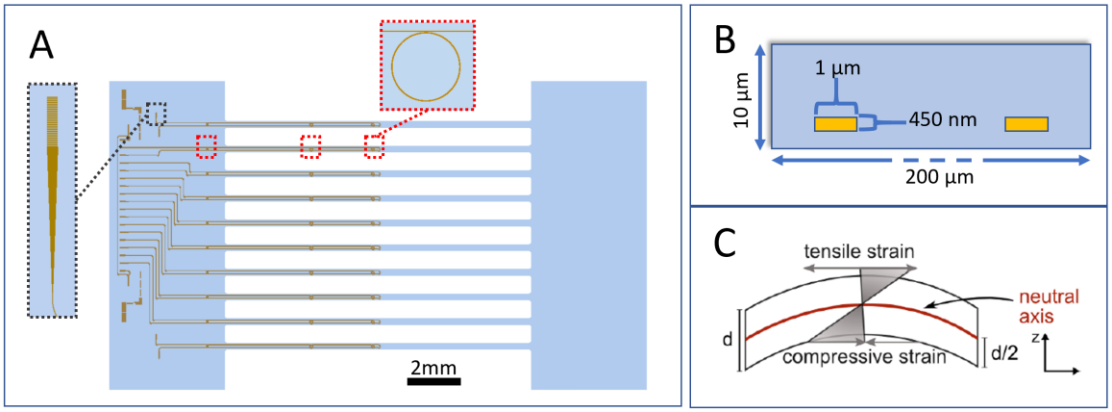

Figure 15: The proof-of-concept device array. A) The layout of the 2D chip design with insets showing the location of the ring resonators and grating couplers. Blue indicates SU8, orange the GSS glass. B) The side profile of one of the sensor strips, not to scale. C) The single neutral-axis theory that defines the region of zero strain in a bent, structure of homogeneous material.

Either SU8 photoresist or PDMS serves as the bottom and top layers of this device array, and act both as a cladding material and structural support. This sensor chip consists of two edge platforms that are used to both stabilize the device array after buckling and also hold input and output grating couplers that guide light into and from each waveguide.

In the center is the device array itself, patterned in strips (10 in this example), each bearing a single waveguide that delivers light to a number of resonant cavities along its length. In this particular array design we utilize grating couplers for light delivery. On the device strip we add a 180° bend at the end of the waveguide such that the input and output grating couplers can be accessed on the same end of the device. Each strip, in order to span millimeters- to centimeters-thick hydrogel tissue models when buckled, is on the order of 1-2 cm long.

The selection of the appropriate resonator design for a given application is a tradeoff between ease of fabrication and the desired sensor density within the tissue model, which will be discussed in section 5.4.1.

5.3 Strain Resolution

On top of the lower cladding layer, which is at least 2 μm thick for good optical confinement, is patterned the GSS grating couplers, waveguides, and resonators, which are then clad by one or more additional layers of the cladding material. The side profile of a proof-of-concept device strip is shown in Figure 15B. What is important to note is that in this example we select a thinner under-cladding than top cladding, in this example placing the device plane 2 μm from the bottom of a 10 μm stack.

We select this position in order to expose the device to bending strain. At the exact center of our device stack exists at neutral plane, shown in Figure 15C. During buckling of the sensor bridge the tensile strain experienced by the top of the device stack cancels out with the compressive strain at the bottom of the device stack at this

plane. The equation describing the strain (ε) experienced by a device positioned off this neutral plane is:

$$\varepsilon = \frac{y}{R} \tag{17}$$

Where y is the distance of the device from the neutral plane, and R is the radius of curvature of the buckled device stack. A negative y indicates that the device is below the neutral plane in a region of compressive strain.

The selection of the cladding material also effects the device strip's in-plane stretchability, which further contributes to the strain experienced by the device. PDMS has over a 1000 times lower elastic modulus than SU-8, which increases the expected strain transfer between the strain in the device's environment and the devices themselves by approximately the same order of magnitude.

The use of a more stretchable material, however, also introduces further design challenges. Previously we have demonstrated stretchable GSS waveguides with good performance on PDMS by patterning the waveguides with a serpentine structure [39]. This significantly increases the substrate area needed for the device. Furthermore, the ring resonators in these stretchable devices could not withstand the same amount of stretch as the serpentine waveguides, and so were patterned on SU-8 islands to shield them from excess stretch. In this application, where the extreme stretchability of the resonant cavity is necessary, we require the use of sub-wavelength grating waveguides and resonant cavities. Subwavelength grating waveguides (SGWs) consist of small segments of the waveguide material separated by spacings far less than the wavelength of light propagating along the waveguide direction [160]. If the spacing is not sufficiently small, these gratings may have the characteristics of a grating coupler or reflector. The necessary spacing (Λ) is determined by:

$$n_B < \frac{1}{2}\frac{\lambda}{\Lambda} \tag{18}$$

Where n_B is the index of the modes confined within the SGW, referred to as Bloch-Floquet modes, the nature of which were derived by Bloch from Floquet's study of 1D periodic partial differential equations in 1929 [161].

5.4 Spatial Resolution

5.4.1 Resonator Design

The resonator design selected determines the spatial resolution and ease of fabrication of the device array. As discussed in Chapter 2, three resonator geometries that have potential for our application include ring, Bragg, and zero-length cavity resonators. The ease of fabrication of these types of devices is generally determined by their minimum lateral dimension. If any kind of stretchable, sub-wavelength waveguide and resonator design is required, then the grating spacing in the waveguide is the minimum dimension. If the waveguides are uniform, then the trade-off becomes more complex.

In a ring resonator the minimum lateral dimension is the single coupling gap between the bus waveguide and ring, which is generally close to the same width as the waveguide. The ring resonator, however, has the largest surface area of these devices. Our group has optimized 450 nm thick GSS ring resonators with diameter 30 μm or greater in order to minimize bending loss, which have demonstrated sensitivities to strain on the order of 0.01% [96, 38].

The use of ChG Bragg cavity resonators is also well established. However, the minimum dimension of a Bragg cavity is the period of the grating, which must be precisely patterned in order to get a good quality resonator. Bragg cavity resonators

optimized for our material system are the same width as a waveguide. They can either be patterned parallel to the waveguide in order to couple the signal in and out, as in a ring resonator, or within the waveguide itself. In the first scenario resonance within the Bragg cavity is observed as a minimum in the transmission spectra, and in the second a maximum. Bragg or similar nanobeam cavities have shown increased sensitivity to strain in previous works, on the order of 1E-4 to 1E-7 % depending on the geometry of the cavity [162, 163].

In order to distinguish between the output signals of multiple ring or Bragg cavity resonators with the same bus waveguide, we fabricate the devices to have different cavity lengths. If the lengths are varied enough, each cavity will have a distinct FSR that can be distinguished on the transmission spectrum. For example, in order to fabricate a series of GSS ring resonators with 1 nm differences in FSR at 1550 nm, it is necessary to change the ring radius in approximately 5 μm increments. For Bragg cavity resonators, changing the length of the central cavity by only approximately 2.5 μm is sufficient for 1 nm differences in FSR at 1550 nm.

The need for different radii means that multiplexing ring resonators in our application necessitates increasing the width of the strips bearing the sensors, which increases their invasiveness in the cell culture platform. This is not the case for Bragg cavity resonators. When multiplexing multiple Bragg or ring resonant cavities per waveguide, typically more than five devices become difficult to distinguish from the output spectra. The higher the Q of the resonators, the more peaks would be distinguishable on the device spectra.

The use of a zero-length cavity resonator requires high-precision fabrication in order to generate a single, distinct resonant wavelength peak for each device. In these

devices the minimum dimension is both the grating spacing and the cavity length. The single resonant peak allows the user to potentially pattern as many zero-length cavities that can fit along a given waveguide. Each zero-length cavity can be tuned to operate at a given wavelength by changing the period of the cavity to meet the condition [164]:

$$a = \frac{\lambda_o}{2 \times n_{eff}} \tag{19}$$

5.4.2 Deterministic Buckling

The 2D geometry shown in Figure 15 is buckled into a 3D device array by releasing the whole structure from the substrate and sliding the edge pieces together to span a distance, *x*. Figure 16A shows an overview of the buckling process. For a buckle with uniform thickness, this results in a symmetric buckle geometry in which the center point of each strip is lifted to a maximum height in the *z*-direction that depends on the buckled strip length and the span of the buckle in x. The shape and absolute value of curvature of this buckle shape is shown in Figure 16B.

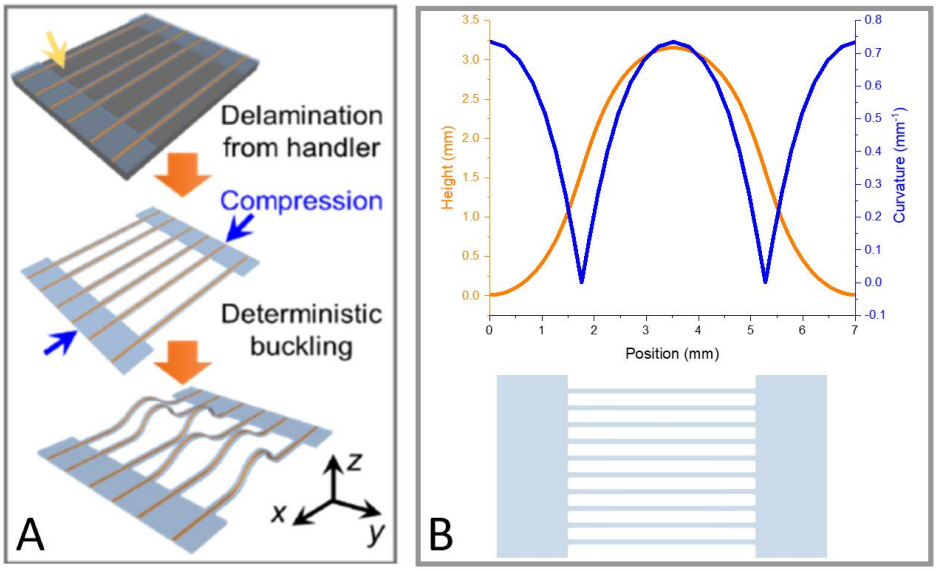

Figure 16: The 2D device is delaminated and buckled into 3D. A) An overview of the buckling process. B) The shape and absolute value of curvature of a symmetric buckled device strip.

The shape of this buckle follows a nonlinear beam buckling theory [165] that assumes that the beam is isotropic, nonlinear, free from initial stress, and undergoes only a compressive load in the direction of the buckle span that is less than the material's yield stress. We also assume a weightless beam.

During large deformation:

$$EI\frac{d^2\alpha}{ds^2} + F\frac{dh}{ds} = 0 \tag{20}$$

In which E is the modulus of the beam, I its cross-sectional moment of inertia, α the angle of deflection, s the arc length, h the height of the beam, and F the load applied to the beam as show in Figure 17.

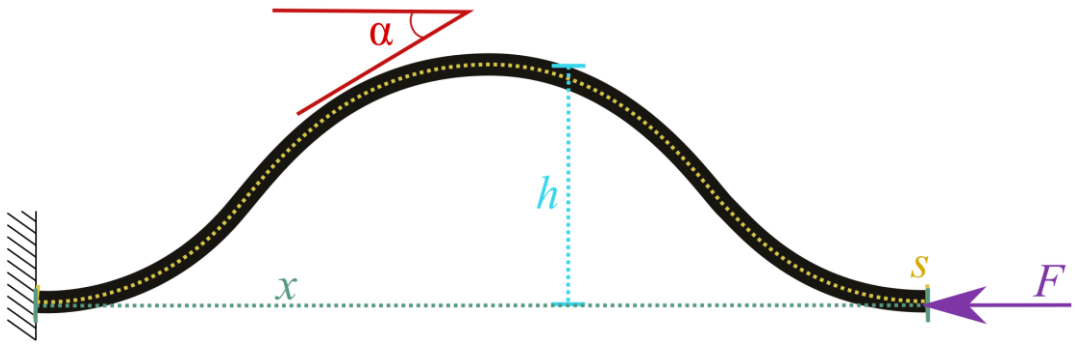

Figure 17: Schematic of the notations used to describe a beam undergoing large deformation nonlinear buckling.

The buckle profile is defined by:

$$x(\varphi) = \frac{1}{k}[2E(\varphi, p_o) - F(\varphi, p_o)] \text{ and } h(\varphi) = \frac{2p_o}{k}[1 - \cos\varphi] \tag{21}$$

For $0 \leq \varphi \geq 2\pi$

Where $k^2 = F/EI$ and $p_o = \sin(\alpha_o/2)$. In this equation, E and F are elliptical integrals. After applying boundary conditions:

$$x(0) = h(0) = 0 \text{ and } h'(0) = h'(2\pi) = 0 \tag{22}$$

The length (L_{tot}) of the buckle is calculated as:

$$L_{tot} = \int_0^{2\pi} \sqrt{x'(\varphi)^2 + h'(\varphi)^2} d\varphi = \frac{4K(p_o)}{k} \tag{23}$$

And the span in x:

$$L = \frac{1}{k}[2E(2\pi, p_o) - F(2\pi, p_o)] \tag{24}$$

By inputting the desired buckle length and span, we can calculate p_o and k in order to calculate the symmetric buckle shape (Figure 17B).

If all buckles in our device array experienced the same type of deformation, this would lead to large areas within our tissue model that are not interrogated by

sensors. In order to get a more uniform device distribution, we can modulate the top cladding thickness of each buckle to get asymmetrically buckled device strips. In Figure 18 we show a buckle shape that results in thickness variation along the buckle from a thickness *t* to 1.2*t*.

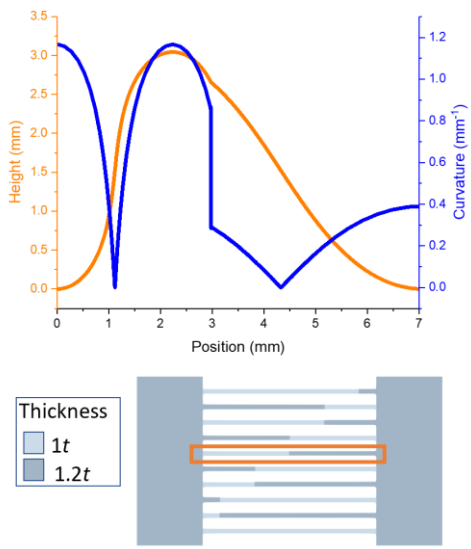

Figure 18: The derived asymmetric shapes of a buckles with total length 1 cm and span 7 mm. The thickness contrast is 1:1.2, with the thinner segment closest to x = 0 mm. Half of the strip is 1.2*t* thickness.

The total length of these two sections is given by:

$$L_{tot} = l_1 + l_2 = \frac{1}{k_1} F(\Phi, p_1) + \frac{1}{k_2}[4K(p_2) - F(\varphi, p_2)] \tag{25}$$

With height:

$$h(\varphi) = \begin{cases} \frac{2p_1}{k}[1 - \cos\varphi], \ 0 \le \varphi \le \Phi \\ \frac{2p_1}{k}[1 - \cos\Phi] + \frac{2p_1}{k}[\cos\Phi - \cos\varphi], \ \Phi \le x \le 2\pi \end{cases} \tag{26}$$

and x-position:

$$x(\varphi) = \begin{cases} \frac{1}{k_1}[2E(\varphi,p_1) - F(\varphi,p_1)], \ 0 \le \varphi \le \Phi \\ \frac{1}{k_1}[2E(\varphi,p_1) - F(\varphi,p_1)] + \frac{1}{k_2}[2[E(\varphi,p_2) - E(\Phi,p_2)] - [F(\varphi,p_2) - F(\Phi,p_2)], \ \Phi \le x \le 2\pi \end{cases} \quad (27)$$

We can then calculate p_1, p_2, Φ, k_1, and k_2 from these equations given the total length, segments lengths, and thickness variation desired.

5.5 Temporal Resolution

An additional resolution requirement that we want to meet is rapid device interrogation that allows us to take minute-by-minute measurements. In tissue model studies it is ideal to perform 3 each of biological and technical repeats alongside positive and negative controls to demonstrate statistically significant differences between sample conditions. In theory this would require us to measure nine or more device arrays at a time. Assuming 10 buckles per array, in order to be able to take measurements of all devices in all arrays once every hour with a single laser, the length of time it takes to scan each device must be less than one minute. For minute-to-minute measurements, we require measurement times on the order of few seconds.

The temporal resolution of our measurements is in part determined by the scanning speed of our laser source, which must scan over a sufficiently broad wavelength range in order to pick up the signals of all the devices along each buckle. Two device design considerations that we can leverage to increase measurement speed are the design of resonators cavity lengths such that we can minimize the spacing between peaks of interest, thereby reducing the range of wavelengths that we need to

scan, and reduction of alignment time to each waveguide with the use of a substrate-bonded fiber bundle that does not require manual alignment to each device.

Optimization of arrayed wavelength gratings with time division multiplexing may also be used to scan multiple waveguides at once [166, 167]. Or, assuming we work with a single laser source but multiple waveguides, we can also use programmed optical switching and measurement software to cycle between devices and/or device arrays. With all of these considerations optimized, we expect that the measurement time could be reduced to seconds per waveguide, allowing us to take minute-by-minutes measurements with this proposed device design.

5.6 Proof-of-Concept Device Fabrication

5.6.1 On-Chip Processing

In order to demonstrate a functional proof-of-concept device with relatively simple fabrication, we selected ring resonators patterned in a device array with a symmetrically buckled geometry. The GSS ring resonators ranged from 30 to 50 μm in diameter and were patterned on SU-8 device strips 200 μm wide and 1 cm long. The thickness of the overall device stack was 10 μm, with the sensors patterned 3 μm below the neutral axis.

Basic principles of fabricating these devices were developed in the University of Delaware Cleanroom in 120 DuPont Hall prior to the establishment of Dr. Hu's research group at MIT. Here the design and UV lithography patterning conditions of the SU-8 cladding layers were optimized using a Karl Suss MA6 mask aligner. The GSS resonators were patterned using a single-layer liftoff resist, RD6, with a photomask and ABM mask aligner system. However, it was determined that these

techniques did not produce devices with sufficiently high quality, and the fabrication was instead continued with fabrication facilities at MIT by my collaborator Jerome Michon. The optimized processing of these devices is described in more detail in Appendix B.

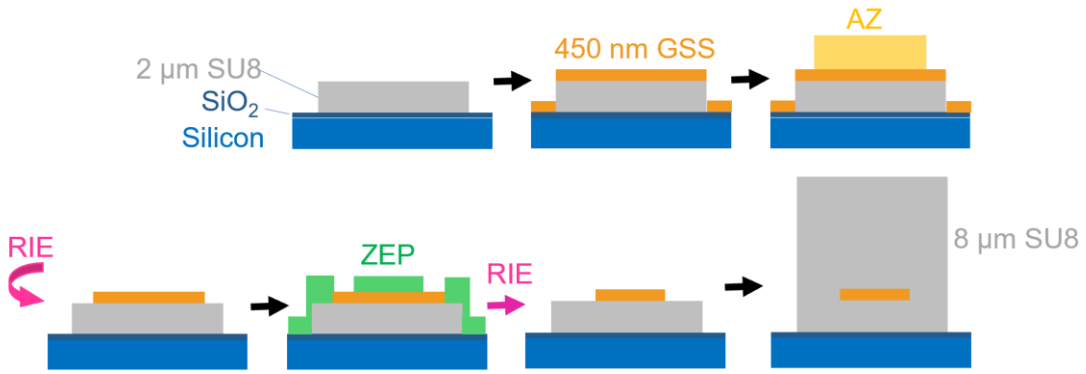

Figure 19: General processing summary for 2D device fabrication.

Figure 19 shows a schematic of this processing procedure. SU8 cladding layers are defined by photomasks using UV lithography, and the GSS is deposited using thermal evaporation. These processes are described in more detail in section 4.4.1. Low resolution AZ resist protects the glass in the location where the waveguides will be patterned, while ICP/RIE using a fluorine etch chemistry removes excess GSS from the edges of the SU8. This allows HF to more readily remove the devices from the substrate, as will be described in the next section. Higher resolution Ebeam resist is then used to define the waveguides, which are again etched with RIE before applying the top cladding layer.

5.6.2 Device Peel-Off

Initial device peel-off conditions were optimized at the University of Delaware. Initial attempts to get free-standing devices involved patterning device arrays on substrates such as glass and silanized silicon. Dissolution of a glass handler with HF solutions was difficult to control, as was holding the device on a handler while dissolving the glass. Patterning devices on silanized wafers to decrease adhesion of the SU8 undercladding caused premature peel-off, as the devices tended to float off the substrate during resist development steps. Finally, a procedure which involved patterning the devices on oxide-coated wafers was selected. In order to remove the final devices from their substrate, the oxide was partially dissolved in HF until the corners of the SU8 began to lift off. The sample was the rinsed and the device covered with water soluble wave-solder tape, which was then used to peel off the device from the substrate. The dissolution of the tape was best in slightly acidified water, with low HCl concentration.

These conditions were further optimized for best reproducibility by collaborator Jerome Michon at MIT. In particular the reproducibility of the partial dissolution of the oxide was optimized by selecting a lower concentration HF solution, 12.5% HF. Device cracking during delamination with the water soluble tape was reduced by using a multilayer tape stack to minimize stretching of the tape during peel-off, which had been straining our devices to their fracture point. This tape stack is then used to attach the device to a handler, with device edges adhered to the handler with Kapton tape. The tape is dissolved with 5% HCl, and the device buckled on-handler. Figure 20 shows images of each device buckling step.

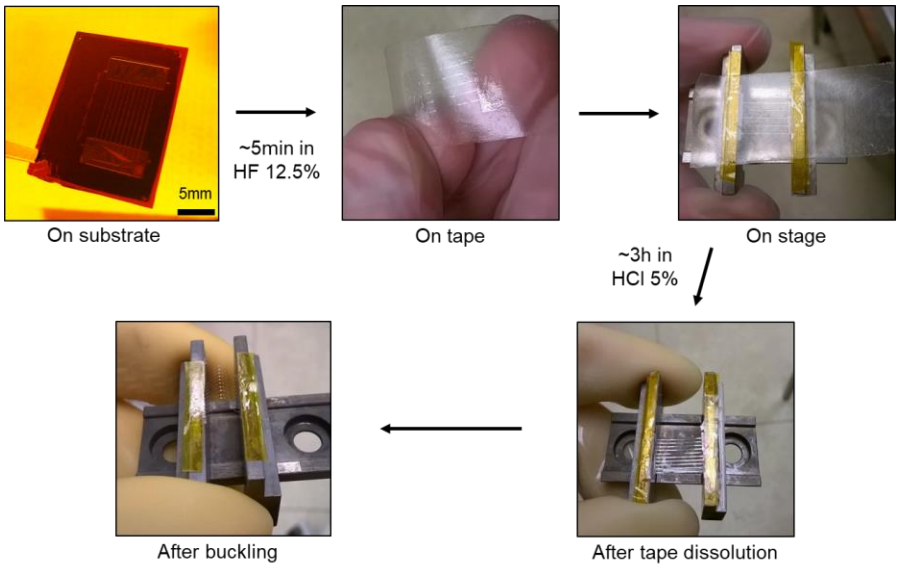

Figure 20: Images of the procedure for device delamination and buckling. Courtesy Jerome Michon.

With robust fabrication protocols established for these proof-of-concept devices, their performance and sensitivity to cell-induced strains was established through finite element modeling and strain-tracking experiments *in vitro*.

Chapter 6

FINITE ELEMENT MODELING OF DETERMINISTICALLY BUCKLED DEVICES

In order to demonstrate the sensitivity of these deterministically buckled sensor arrays to *in vitro* deformations, finite element models of SU-8 buckles were compared to the proof-of-concept fabricated device response to compression between stainless steel blocks. Then, to utilize FEM to simulate a relevant *in vitro* environment, PDMS buckles were subjected to expected deformations and stiffness changes in a cardiac graft tissue-like material system. COMSOL Multiphysics 4.3b with the structural mechanics module was used to perform these modeling experiments.

6.1 Shape

In order to interrogate a mm's thick graft tissue model, four symmetric and asymmetric buckles with 1.4 cm lengths and spans of 1 cm were also modeled. Small thickness variations in these 1.4 cm long buckles, variations of 1.2*t* or less, were found to be more than adequate for significant displacement of the maximum height of the asymmetrical buckles from the center of their span. Furthermore, we selected these geometries because greater thickness variations lead to sharp transitions between thin and thick buckled regions, the meshing of which was difficult to resolve in COMSOL. The buckle thickness selected was also limited by ability of COMSOL to resolve the step between thin and thick regions on such high aspect-ratio structures, therefore 20-24 μm buckle thicknesses were selected for these models even though we had

experimentally demonstrated buckles with 10 μm thickness. The four shapes chosen are plotted in Fig 21.

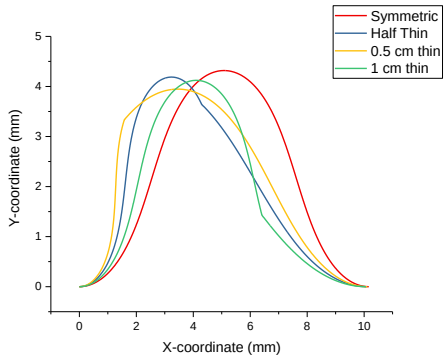

Figure 21: The four buckle shapes used in the cardiac graft tissue-model.

6.2 Device Compression Experiments

The compression of buckle shapes between two metal blocks was performed with 2D modeling. The edge faces of each buckle were fixed to the edge faces of the lower block with rigid connector physics in COMSOL. The bottom of the lower block and the edge faces of the buckle were constrained in all 3 dimensions and not allowed to rotate. The top block made point contact with the highest point of the buckle and its motion was constrained in all but the z-direction. The bottom face of the buckle and top face of the lower block, and the top face of the buckle and bottom face of the upper block were modeled as contact pairs. The mesh on these boundaries was refined in order to improve convergence of their contact. In order to compress the buckle, the top block was lowered in z by a prescribed displacement. Friction was not applied to this model, and all materials were considered linear elastic and isotropic.

6.2.1 Symmetric Buckle Compression

In Figure 22 is shown the results of compressing the symmetric buckle shape by different displacements, In Figure 22A is shown the buckle shape before and after displacement, and in 22B is the calculated strain of a device 3 μm below the neutral axis of the buckle at the midpoint of the buckle at each deformation.

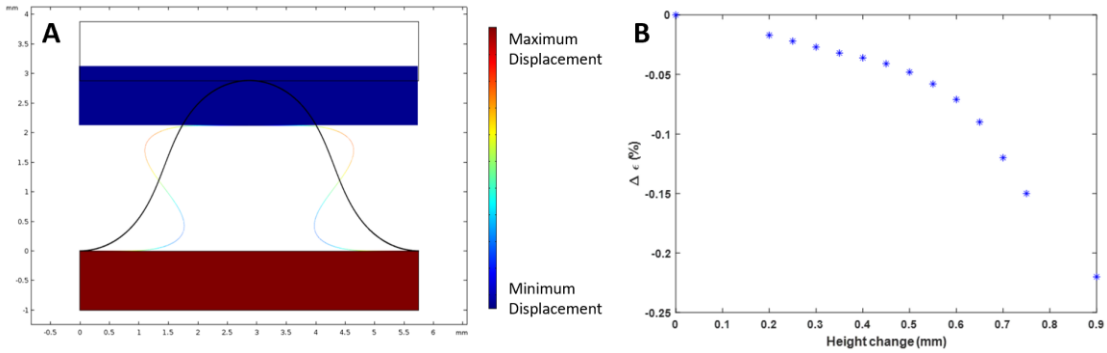

Figure 22: Simulation results used in the calibration experiment. A) The deformed (color) shape of the symmetric buckle (original shape in black), displaced by a block 0.7 mm in the z-direction. B) The calculated strain at the midpoint of the original buckle versus the displacement of the block.

6.2.2 Symmetric Calibration Test

These simulation results were compared to experimental results in order to determine the strain sensitivity of our devices. In this test, an array of 1 cm long symmetrically buckled device strips is fixed to its holder at a 7 mm device span. Each strip is 200 μm wide and 10 μm thick. As in the previous chapter, the device response to temperature is characterized before and accounted for during the experiment. In this experiment we track the resonant peak shift of a device at the top of the buckle.

A motorized stage with a piezoelectric actuator (TRA25CC, Newport) is used to lower a metal block over the buckle array until it comes into point contact with the top of the buckles. It is then incrementally lowered by the same distances as in the simulation studies. Figure 23 shows the device resonant peak shift versus displacement, averaged over the devices tested.

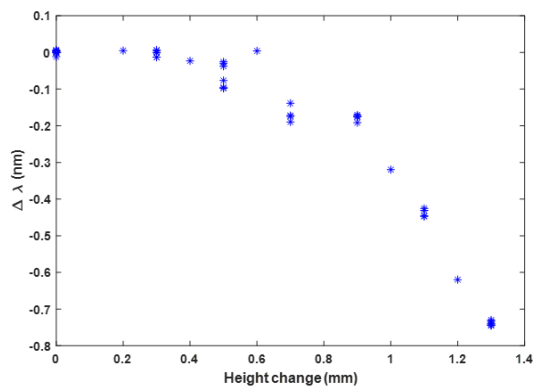

Figure 23: Experimentally determined resonant peak shift versus displacement of a symmetrically buckled proof-of-concept device. Error bars (~10 pm) are too small to be seen.

One limitation of this technique is that the small variations in the buckle shape that result from manually placing it on a holder mean that we have to experimentally determine the "0" height at which the block starts compressing the buckle. An alternative calibration that accounts for this will be discussed in the next section. From these data we can compare the strain determined by the simulation experiments, and experimentally determined peak shift as a result of the deformation of the proof-of-concept device. A linear relationship, $\Delta\lambda = 3.2 \cdot \Delta\epsilon - 0.04\, nm,$ between peak shift and strain is observed, plotted in Figure 24.

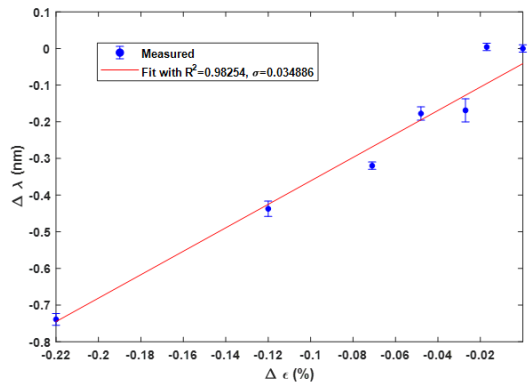

Figure 24: The determined peak shift vs strain of the calibration device.

6.2.3 Accounting for Variations in Shape

While the calculated error in these data is on the order of 0.03%, this calibration method is further limited by the assumption that the shape of the calibration device buckle spans precisely 7 mm. Since the device array is loaded on the sample holder by hand, we estimate that the variations in buckle shape contribute additional error to the estimate of the strain on the order of 1%.

An all-optical calibration method was therefore developed that was independent of variations in the initial buckle shape. Two aspects of the device fabrication and buckling are controlled with high precision. The first is the Ebeam patterning of the devices, which allows us to know the spacing between devices along a waveguide with sub-micron accuracy. Secondly, we rely on precisely machined spacers in order to control the span of the buckle being held on its handler. Therefore, the change in span with the substitution of different spacers is also known with great accuracy. In this experiment, the change in peak position of at least two resonators after changing between one spacer (*a*) to another (*b*) is used to calculate the change in

strain at the device in response to changes in the buckle span. This result is utilized to calculate the buckle length and the devices' positions along that length.

First, due to the linear relationships between resonant peak shift and strain, and buckle curvature and strain, we can define the following relationship with notation *a* and *b* designating the two different shapes due to changing the buckle span:

$$\frac{\Delta\kappa_a}{\Delta\kappa_b} = \frac{\Delta\lambda_a}{\Delta\lambda_b} \tag{28}$$

This can be substituted into a system of equations that can be solved for each buckle's length, span, and the changes in those lengths and spans at different deformations. The system of equations that can be solved using this relationship is:

$$\begin{cases} L_1 - L_{tot} = \Delta span_1 = \Delta span_2 \\ L_1 = \frac{1}{k_1}[2E(2\pi, p_1) - F(2\pi, p_1)] \\ L_2 = \frac{1}{k_2}[2E(2\pi, p_2) - F(2\pi, p_2)] \\ L_{tot} = \frac{4K(p_1)}{k_1} = \frac{4K(p_2)}{k_2} \\ \Delta L_{a-b} = \int_{\phi_a}^{\phi_b} \sqrt{x_1'(t)^2 + h_1'(t)^2}dt = \int_{\phi_a}^{\phi_b} \sqrt{x_2'(t)^2 + h_2'(t)^2}dt \\ \frac{\Delta\kappa_a}{\Delta\kappa_b} = \frac{\Delta\lambda_a}{\Delta\lambda_b} \end{cases} \tag{29}$$

6.2.4 Force/Strain Sensitivity Determination.

The resolution of peak shift vs strain experienced by resonators along the device strips is high, however what we aim to study by integration of this device into 3D cell culture systems is the deformation of a hydrogel which then deforms the buckle. Due to the rather extreme modulus mismatch between the hydrogel and our device, we do not expect this strain transfer to be near unity. Rather, from the geometry of the buckle, as well as the Young's modulus of the strip/cladding material

(E_{clad}) and of the material in which it is embedded (E_{gel}), we can calculate the minimum Young's modulus that we expect to be able to deform the buckle ($E_{min,gel}$):

$$E_{min,gel} \geq \frac{48}{5}\frac{Rt^3}{L^4}E_{clad} \tag{30}$$

The derivation of this equation in in Appendix C. Where R is the bending radius, t the thickness, and L_{tot} the length of the buckle segment. Geometrical parameters are illustrated in Figure 25.

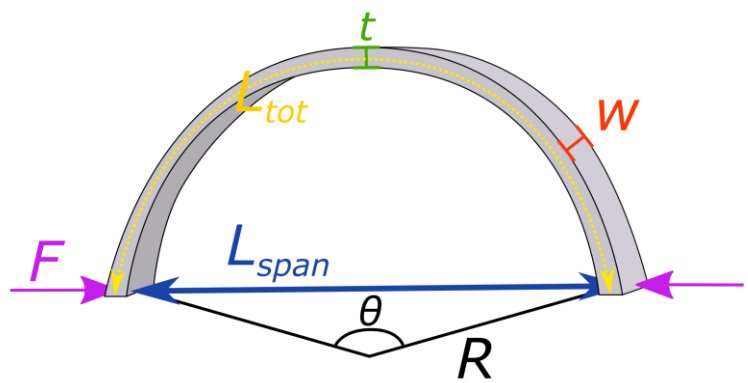

Figure 25: Geometric parameters used to calculate the sensitivity of these devices.

We can also calculate the minimum force detectable by our devices from these parameters as well as the minimum detectable peak shift, $\Delta\lambda_{min}$, the strain-optical coefficient, α, determined from the calibration study in Section 6.22, and the device distance from the neutral plane, y, defined in Section 5.3.

$$\Delta F_{min,clad} = \frac{E_{clad}wt^3}{10R} \cdot \frac{\Delta\lambda_{min}}{\alpha y} \tag{31}$$

The change in strain in the hydrogel that is detected as a result of this force is equal to:

$$\Delta\epsilon_{gel} = \frac{4}{5}\frac{t^3}{yL^2} \cdot \frac{E_{clad}}{E_{gel}} \cdot \frac{\Delta\lambda}{\alpha} \tag{32}$$

Substituting typical geometrical parameters: $w = 10\ \mu m$, $t = 10\ \mu m$, $y = 3\ \mu m$, and $R = 1\ mm$, as well as the experimentally determined $\alpha = 3.2\ nm/\%$, the minimum force detectable on an SU-8 buckle with modulus 4.02 GPa, is 419 nN. For a PDMS buckle with typical modulus of 2.6 MPa, the minimum detectable force is 271 pN, an impressive sensitivity, higher than almost all other force detection techniques. The minimum change in strain in the hydrogel that can be detected from an SU8-clad sensor embedded in 1 kPa hydrogel with the same geometric parameters is 0.34% strain, while the same value for a PDMS buckle is 2.2×10^{-4} % strain.

These analyses show the impressive sensitivity predicted for buckles experiencing primarily bending strain, however, some of the expected deformations of these buckles cause them to experience changes in length. In the next section, an example of buckle deformation in stretched FEM of cardiac graft tissue models is utilized to demonstrate a possible real-world application of these devices, and further demonstrate their sensitivity to relevant material parameters and deformations.

6.3 *In vitro* Cardiac Graft-like Finite Element Model

Heart disease is the leading cause of death worldwide according to the CDC. A major contributor to these statistics is the inability of heart tissue to repair injury without the formation of thick scar tissue, which leads to future heart failure. One solution to this problem is the development of artificial graft tissues densely populated with relevant cell types, such as cardiomyocytes and cardiac fibroblasts, that can be placed over the wound to aid healing. The ideal cardiac graft tissue would have tens of square centimeters of surface area, approximately 1 cm thickness, and contain an

aligned, healthy population of mature cardiac cells [3]. The alignment and development of the cells is typically accomplished by tethering the tissue model to PDMS posts [168], or through the application of cyclic stretch of 5-10% strain to the tissue construct [169, 170].

6.3.1 Limitations of Current Graft Tissue Models

The development of these replacement tissues is severely limited by the difficulty of perfusing thick tissue constructs with oxygen and media, which maintains cell viability. Lack of active perfusion can lead to cell death in all but the outer 100μm of the tissue model [171]. In order to combat these issues, scientists have developed a number of perfusion methods [172, 173], some of which incorporate artificial vasculature [173, 174]. Often the effectiveness of perfusion can be tested by perfusing a factor that increases the contractility of the cell type being studied, which is characterized either through its ability to contract or stiffen the tissue model [175, 28], or more traditionally by observing changes in cell morphology or expression of phenotype-specific genetic markers [176].

In one study, collagen models of human umbilical veins with varying rat-derived MSC seeding densities undergoing cyclic or static stretch were compared. Overall the difference in tensile strength between ‘overpopulated’ (and therefore nutrient-starved) models and those with a lower initial seeding density of MSC’s after one week was approximately threefold, as determined by uniaxial tensile testing, in which the sample was stretched at a rate of 1%/s until failure [175]. The difference in the rate of surface area contraction of floating collagen gels populated with mouse-derived MSC’s of different fibrillar density was studied by Serpooshan et al [28]. The

contraction rate increased by approximately 13%/day with a 3% reduction in fibrillar density. Other studies have shown that the combination of both cyclic stretch and the perfusion of tissue models with contraction-stimulating factors enhances differentiation of cardiac fibroblasts to myofibroblasts [177, 178] or increases strain induced by cardiomyocytes [179] better than either cyclic stretch or perfusion alone.

6.3.2 Experiment Design

In this work, we aim to analyze the mechanical and sensing response of the sensor array via analytical modeling and FEM and verify that the sensor can be applied to stiffness gradient detection in cardiac graft tissue models. In our FEMs we utilize the COMSOL Multiphysics 4.3b Solid Mechanics module to encase the four buckle shapes shown in Figure 21 in rectangular volumes of hydrogel-like material. The thin regions of each buckle are swept with a rectangular geometry 20 μm thick by 20 μm wide. The thicker regions are 24 μm thick. We choose a larger than necessary width and thickness in order to enable meshing of the step between the thin and thick segments.

In order to mimic the cyclic strain typically imposed on cardiac graft tissue models, the whole gel is strained by 10% in the z-direction. The base of the hydrogel, and each end face of the buckle are modeled as fixed constraints. The top face of the gel undergoes a prescribed displacement in the z-direction of 10% of the gel height. For the purposes of this experiment, the ‘hydrogel’ is modeled as an isotropic, linear elastic material. We make this choice because the 10% strain imparted on the material is within the linear elastic regime of many hydrogels. Figure 26 shows a model of a symmetric buckle undergoing this deformation. The black frames indicate the initial

geometry of the buckled strip and hydrogel block, and the colored regions the deformed geometry.

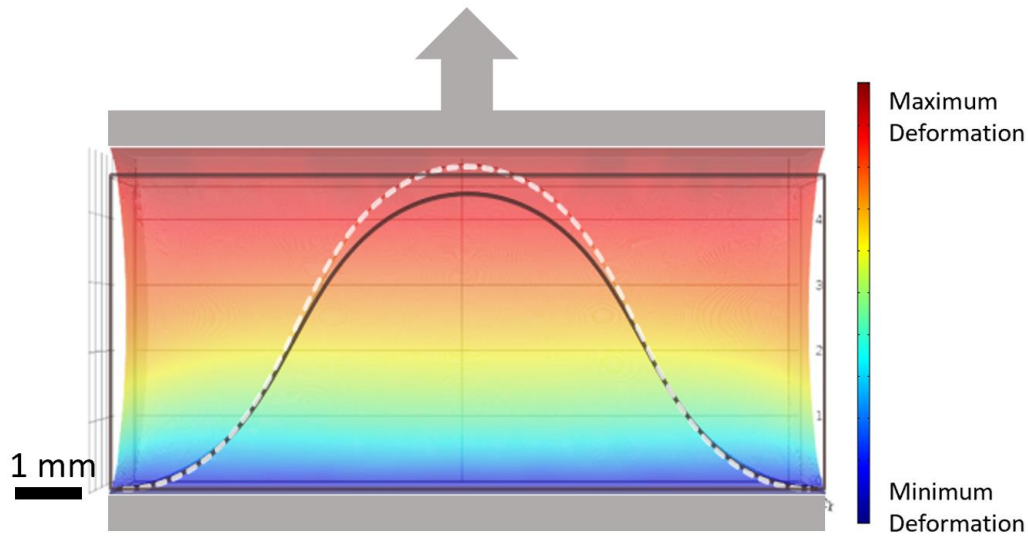

Figure 26: Deformation of a symmetric buckle in a 240 Pa hydrogel-like FEM stretched by 10%.

We vary the stiffness of the environment between 240 Pa and 1200 Pa to mimic the modulus of a valvular interstitial cell-populated poly(ethylene glycol) tissue model from the literature with a tunable modulus ranging from that of damaged (or developing) and healthy cardiac tissue [180] and observe the differences in local strain experienced along each buckled device strip in each environment. In our first study we compare the deformation of the buckle in blocks of different uniform modulus. The purpose of the study is to show that the strain variation detected by the sensors can provide precise information about the stiffness of the hydrogel matrix the sensors are

embedded in. In the second, we impose a radial gradient in x and y on the modulus of each environment, with the highest modulus in the exact center of the gel. This design is selected to model the effects of the perfusion of growth factor from a central vasculature in the gel. In this study we do not model the geometry of the vasculature, and instead study of the effects of perfusion from an idealized dimensionless vasculature. This locally increases the contractility of local fibroblasts and as a result increases the modulus of the gel at the center point. For simplicity, we do not induce a gradient due to diffusion of media or oxygen from the outside of the gel block. These gradients are defined by an error function and diffusion coefficient determined by Kihara, et al. for a collagen hydrogel (2.7×10^{-6} mm^2/s), a typical platform for the development of tissue models.

$$E(x,y) = (E_{max} - E_{min}) * (1 - \frac{\mathrm{erf}(abs(\sqrt{(Xc-X)^2+(Yc-Y)^2}}{2*sqrt(Dt)})) + E_{min} \qquad (33)$$

In this equation E_{max} and E_{min} are equal to 1200 and 240 Pa, respectively, with (X¬c, Yc) being the coordinate of the center of the hydrogel. The diffusion times chosen are 6, 18.5, and 37.5 hours, in order to increase the maximum distance of perfusion from the center by 1 mm increments.

In a third model we explore using the sensor array to pinpoint the spatial displacement of the vasculature in x. We offset the central point of a radial gradient with a diffusion time of 6 hours and compare the deformation of the device strip in these environments to its deformation in a uniform modulus environment of 240 Pa. The mechanical properties used to define each material in this FEM are shown in Table 1. The strain in the PDMS strip as a result of its deformation is calculated along

its arc length. The strain profile is then used to determine the displacement of the vasculature.

Table 1: Material parameters used in building a PDMS buckle-in-hydrogel FEM.

Material	PDMS	Hydrogel
Young's Modulus	2.6 MPa	240-1200 Pa
Poisson's Ratio	0.495	0.495
Density (kg/m3)	0.97	1000

Some low-grade noise results from the modeling of a highly anisotropic beam in a large volume, which cannot be accounted for in the refinement of the mesh. We therefore select to smooth this noise with post-processing using weighted adjacent point averaging in Origin 2017. The averaging windows are defined as 3.2% the total number of points plotted along the arc length.

6.3.3 Results

The original and deformed shape of the symmetric buckled strip in a 240 Pa environment is shown in Figure 27A. In our first experiment, the strain at each point along the deformed structure in 240 to 1200 Pa environments is calculated. The strain experienced at points along this buckled strip in different moduli is shown in 27B. The regions of maximum relative strain are approximately ¼ and ¾ along the length of the buckle, with the second highest relative strain experienced at the midpoint.

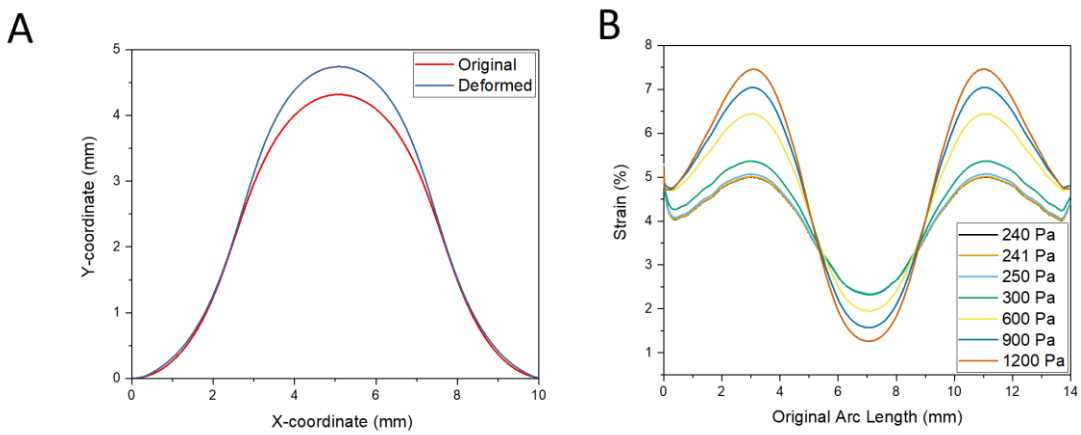

Figure 27: A) The deformation of a symmetric buckle in 240 Pa environment. B) The strain experienced at points along its arc length after deformation in different modulus materials.

Figure 28 shows the strain experienced in different modulus materials at two representative points for each of the four buckle shapes. The regions chosen are the two points undergoing the largest amount of strain due to this deformation. The maximum strain region in each buckle is typically that which is the most aligned with the direction of the strain imparted on the hydrogel. The strain in general exhibit a sub-linear dependence on the modulus of the hydrogel. The sub-linear dependence can be empirically fitted with simple exponential functions with R^2 values consistently above 0.998. From the curves for the asymmetrical buckles, especially, we observe that differences in modulus of 1 Pa lead to changes in strain between 0.006% to 0.011 % at these points, suggesting that our technique can readily identify changes in modulus throughout the hydrogel of less than 1 Pa.

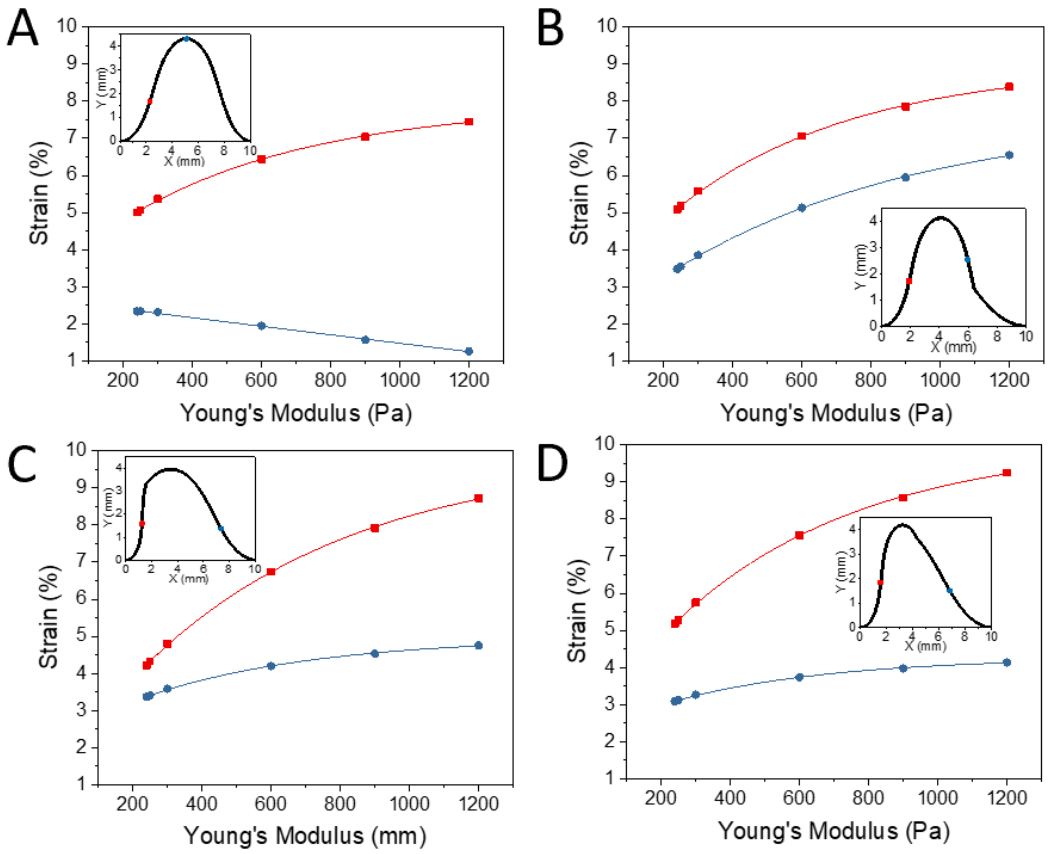

Figure 28: The strain experienced at two points along each buckle shape in different modulus materials. Insets show the shape of the buckle and the points corresponding to each set of deformations.

To determine the magnitude and position of modulus gradients throughout the gel, we compare the deformation of the symmetrically buckled strip in each environment. The strain along the buckle deformed in uniform 240 Pa hydrogel is subtracted from the strain experienced by the device in each gradient. In Figure 30 is plotted the modulus gradient alongside this normalized strain. These data are plotted vs the buckle span, X, instead of arc length in order to show the relationship between

gradient position and strain. As can be seen in this comparison, the span of the region of maximum deformation in the buckle is strongly correlated to the span of the modulus gradient.

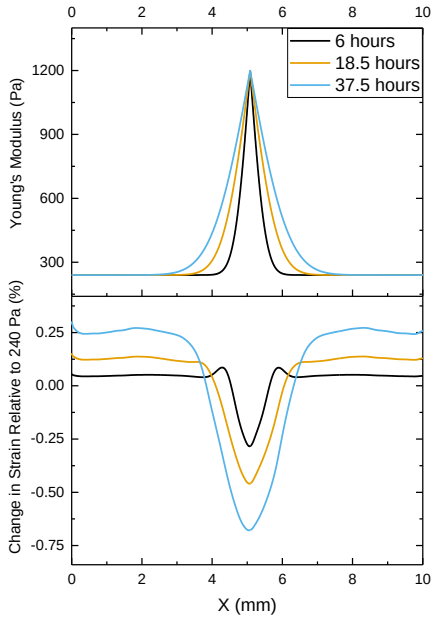

Figure 30: The gradient magnitude (Top) defined by theoretical diffusion time of growth factor, and the change in strain in a symmetric buckle normalized to its deformation in uniform 240 Pa material, versus their position in X.

To determine whether the gel has an offset gradient, we look at the symmetry of the strain in the buckle vs X. In Figure 31A is plotted these data, which again are normalized to the strain along the buckle deformed in the 240 Pa hydrogel. The position of the absolute value of maximum normalized strain is strongly correlated to

the offset of the gradient from the center point in the hydrogel. This correlation is well defined by an exponential function, shown in Figure 31B.

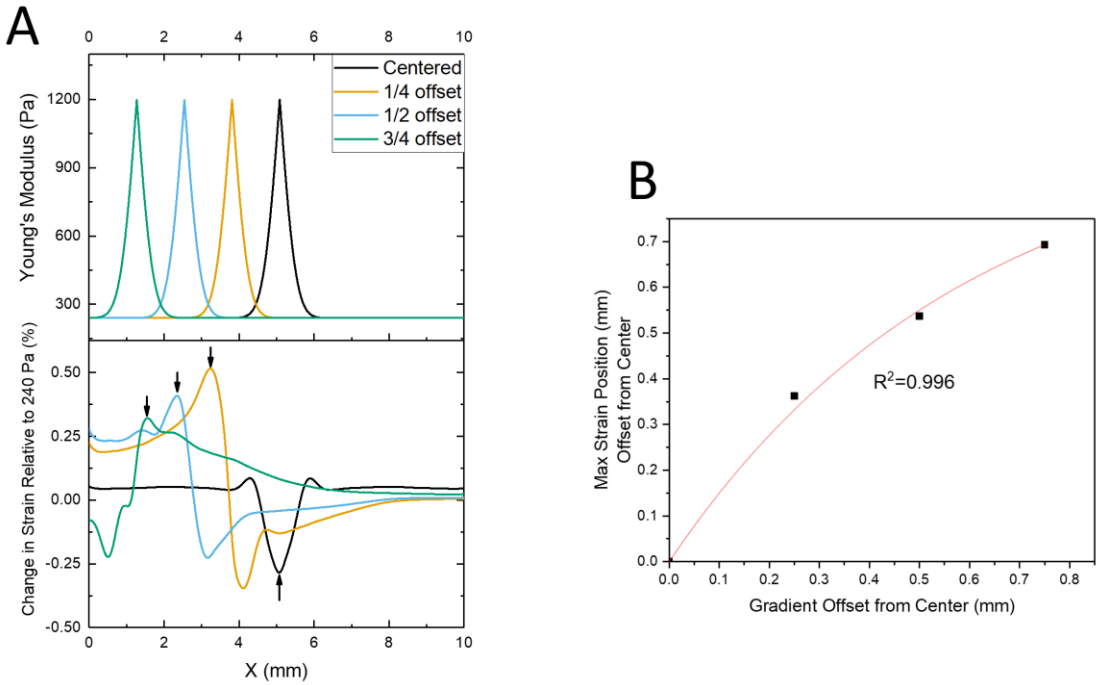

Figure 31: A) Comparison of gradient position and relative strain along a symmetric buckle, normalized to deformation in uniform 240 Pa modulus gel. B) The exponential relationship between gradient position and the position of maximum magnitude of strain along the buckle.

6.3.4 Summary

This experiment successfully demonstrates the application of our deterministically buckled sensors and their deformation in 3D *in vitro* cardiac tissue model under tension. Under this type of deformation, the primary deformation of the PDMS buckles is tensile strain, and the device may be patterned at the neutral plane without significant loss in sensitivity. In fact, the large amounts of strain, on the order

of several percent, are too great for normal waveguides. For this device we would propose the use of sub-wavelength grating waveguides, so that the waveguides themselves can be stretched on the order of the deformation of the buckle.

Chapter 7

DEVICE INTEGRATION

The theoretical determination of the devices' sensitivity to differences in strain due to stiffness gradients in *in vitro* tissue models via finite element modeling establishes the validity of this method for local strain detection. Here we verify the usefulness of a proof-of-concept device array in real-world applications.

7.1 Collagen Contraction Experiments

As discussed previously, the contraction of floating or partially tethered collagen gels has had widespread use for decades as a method to characterize the forces output by contractile cells such as fibroblasts in response to different physical, biological, or chemical cues. Typically gels in these experiments are imaged or tethered to force gauges to determine the characteristics of the cell behavior. For our experiments, in order to compare the readout of our devices to visible cell contraction, a Rat Tail Type I collagen gel system with a high population of neonatal dermal human fibroblasts (NDHF) was selected. This cell type was selected for its high doubling time (18 hours) and high contractility. Its primary nature makes these cells more sensitive to any cytotoxic factors in their environment than immortal cell lines such as NIH3T3s. Therefore we also used these cells to test the cytocompatibility of the cell culture systems developed for these studies.

For these studies, populations of 1 million NDHF/mL fibroblasts were cultured in 3-4 mg/mL collagen. First, a study showing typical changes in gel volume and

metabolic activity was performed over 24 hours. In this study, 1 million/mL NDHF was cultured in 3 mg/mL rat tail type I collagen. First, the collagen precursor was brought to the correct concentration with 0.002 M sterile Acetic Acid. Sterile 10X PBS was added to 10% of the final gel volume to maintain tonicity of the cell culture. A 100 μL aliquot of this solution was taken, and the pH slowly increased by the addition of sterile 1M NaOH in 0.5 μL increments, until the pH was brought to 7.6-7.8 according to pH test strips. The gel was observed to make sure this mixture yielded a uniform gel. This ratio of NaOH to precursor solution is used to pH the gel at a later step. The precursor solution is kept on ice in a sterile tube until needed.

Early passage (0-6) Primary NDHF from ATCC were maintained with low-growth serum media, also from ATCC. Media was changed every 2-3 days to maintain cell culture pH and oxygenation levels. For this study, cells were lifted from their culture flasks with 0.25% Trypsin and incubated for 5-10 minutes. These cells were then removed from the flask in Trypsin solution and spun down at 1500 RPM for 3 minutes. The Trypsin was removed, the pellet broken, and the cells resuspended in media. After cells were counted with a hemocytometer, the desired cell population for the study was separated and spun down. The leftover cells were passaged into a new flask. While the cells were centrifuging, the collagen mixture was brought to the proper pH with the calculated amount of 1M NaOH and gently mixed with a pipette. Some collagen was pipetted into cell culture wells before adding cells, as a control. The excess media was then removed from the cell pellet, and the pellet broken. The remaining collagen was gently mixed with this pellet before aliquoting the culture into its wells. Gels were incubated for 20 minutes to half an hour to allow gelation to

complete. Media was then added to the tops of the gels, and culture continued in the incubator. Three repeats of gels with and without cells were studied.

For the metabolic assay, the cell culture media was mixed in 10:1 ratio with prestoBlue. This was done immediately after the gel had formed, and then again at the end of a 24 hour study. The media/prestoBlue mixture was then incubated for 2-3 hours. Three 100 μL volumes of the solution were aliquoted from each well into a 98-well plate. The remaining solution was removed and replaced with normal media to continue the cell culture. A fluorescence plate reader was then used to excite fluorescence in the metabolized prestoBlue at 560 nm and read out the resulting signal at at 590 nm.

For the volume study, media was carefully aspirated from the gel, then added back slowly until the media formed a meniscus that just reached the top of the well. The volume of media was recorded, and the media volume returned to its original level.

The results of both of these studies is shown in Figure 32. No statistically significant difference was noted in the control wells, so only data from the cell culture is shown. Data is normalized to the control well volume or metabolic activity at the start of the study. It can be seen that the volume of the gels decreases by approximately 40%, while the metabolic activity more than doubles. Both of these changes are statistically significant with $p<0.05$ according to Student's TTest.

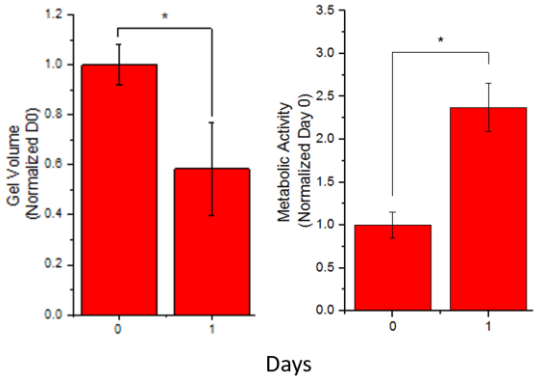

Figure 32: Change in gel volume and metabolic activity of 1 million NDHF cultured within a 3D, 3mg/mL collagen gel over 24 h. * indicates statistical significance, $p<0.05$.

7.2 Environmental Control

Typical cell culture conditions require a number of environmental controls including temperature, humidity, oxygenation and CO_2 concentration. Two environmental control systems were developed to support 3D cell culture around this sensor array. One system enabled use of multiple device arrays at a time on an optical benchtop. The other allowed devices to be used within a cell culture incubator. All components of both chambers were sterilized by soaking in 70% ethanol for several hours followed by overnight exposure to a UV lamp before initiating cell culture.

7.2.1 Gas Flow

The maintenance of humidity levels, typically 80% and above, in cell culture ensures that cell culture media does not evaporate from the surface of the hydrogel and reoxygenates the media. The delivery of 5% CO_2 to the mammalian cell culture maintains physiological pH to combat the effects of cell metabolism, which acidifies the cell environment [181]. The input gas to the cell culture system must be passed

through sterile filters in order to remove any airborne bacteria that may infiltrate the system.

In the benchtop cell culture system, a gas flow chamber was attached overtop a row of wells with an airtight gasket. These wells are designed to fit over the buckled part of the device, leaving the edges partially exposed. This design was selected for early iterations of the device arrays, in which edge coupling was used to deliver light to each waveguide. Before adding the gas flow chamber, a sterile aeraSeal adhesive filter was cut with a sterilized scalpel in a cell culture hood and stuck overtop of the wells. The aeraSeal over one well was punctured and the well filled with water to serve as a humidification reservoir. The gas flow chamber was screwed to the top of this seal, and airflow was initiated using low base pressure on the order of 5 mTorr from a cylinder of 5% CO_2, 75% N_2, 20% O_2 cylinder purchased from Keen Compressed Gas. In addition to the humidity from the water-filled cell culture well, the gas was humidified by pumping it through a sealed glass bottle filled with DI water. A second line collected the humidified gas expelled from this bottle and delivered it to the gas flow chamber through a sterile syringe filter. The port that allowed gas out of the chamber was also sealed with a sterile filter.

In the second iteration of the cell culture chamber, the cell culture well was capped with a sterilized cover slip. The cover slip was selected over the aeraSeal since a screwed gasket was not required for this system, and without it the aeraSeal peeled off the wells over time. The device in this chamber was interrogated by an optical fiber bundle instead of edge coupling. The fibers in the bundle, each less than 1 mm in diameter, could be passed through the doors of a cell culture chamber without impacting its performance, or the performance of the fibers. A window caulk putty

was put around the incubator door where the fibers passed through to ensure an airtight seal. Gas flow in cell culture incubators is controlled via a mass flow controller that combines pure CO_2 with air, that is then passed through sterile filters. The incubator is then humidified by a large water reservoir.

7.2.2 Temperature

Temperature regulation typically requires 37 ± 0.1 °C for mammalian cell types, including the NDHF used in these studies. An additional factor that needs to be considered in the use of photonic resonant cavities is their peak shift in response to temperature changes, which is on the order of 70-150 pm/°C as demonstrated in Chapter 4 of this thesis. In order to account for these fluctuations, we require either very high stability in terms of fluctuation in temperature of the cell culture system, or a way to calibrate the device response to temperature.

Two flexible resistive heaters soldered in series were used to maintain the temperature of the benchtop environmental control system. One was placed under the chamber and the other wrapped around the chamber. A 3216 Eurotherm was attached to the input and output leads and the PID optimized to minimize temperature fluctuations down to the order of 0.1 °C.

While maintaining physiological conditions is easier in a dedicated cell culture incubator, the temperature fluctuates similarly, on the order of ±0.1 °C, leading to visible peak shifts in our devices due to this fluctuation. In order to account for this, an additional ring resonator was added to our device design on the unbuckled edge part of the device. This ring can be used to perform temperature tracking and account for the

peak shifts seen at the other device. In Figure 33 is shown the spectra from a single waveguide bearing three resonators with radii of 30, 40, and 45 μm.

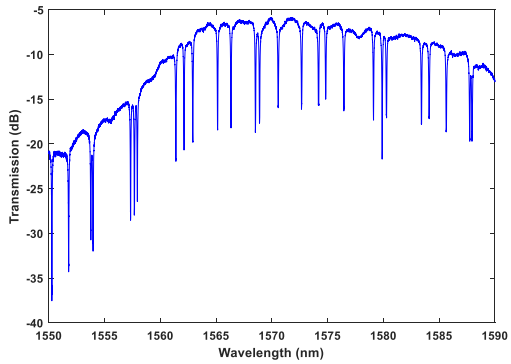

Figure 33: Spectrum from a waveguide bearing 3 ring resonators with different radii.

Figure 34 shows a comparison of the peak shifts seen at a temperature-tracking resonator versus an on-buckle resonator. The linear trend between their peak shifts can be fit with high accuracy, with an R^2 of 0.994, and fit of $\lambda_{buckle} = 1.2077 * \lambda_{T-tracking} - 326.342\ nm$.

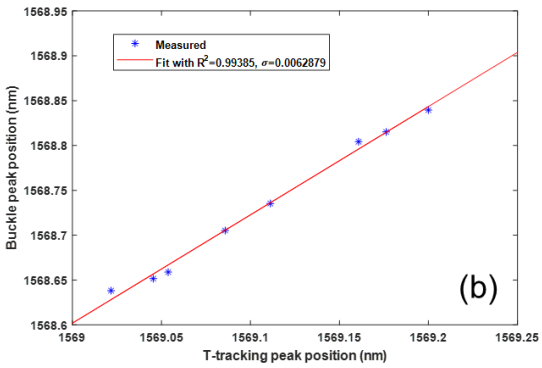

Figure 34: Linear relationship between temperature-tracking and on-buckle resonant cavities in a buckled device array

This relationship can be used to account for the temperature-induced wavelength shifts in the *in vitro* integrated devices.

7.2.3 Benchtop Cell Culture Chamber

An overview image of the benchtop culture chamber is shown in Figure 35. The base of this chamber is a machined polystyrene buckling stage, which contains lateral screws along which the stage is actuated.

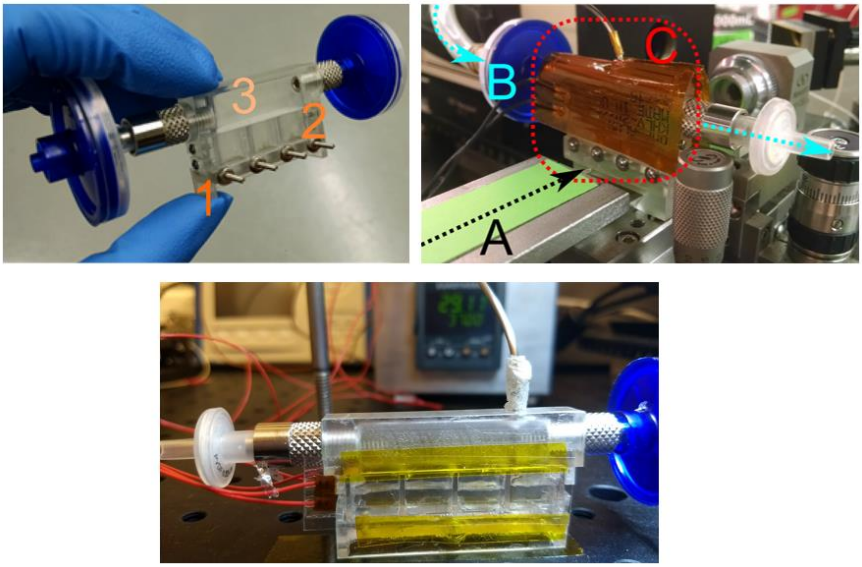

Figure 35: Benchtop cell culture system. Top Left: The components of the system are shown. 1) the base of the well serves as a handler that buckles the device, 2) wells are fixed over top of the buckles, 3) A gas flow chamber is fixed over the wells, and is accessed through sterile syringe filters. Top Right: The chamber's integration with environmental control and the optical measurement system is demonstrated. A) A lensed optical fiber interrogates the buckled devices via edge-coupling. B) A humidified 5% CO_2 gas mixture is flowed through the gas flow chamber. C) a resistive Kapton heater maintains temperature around the device. Bottom: The Kapton heater is replaced with a transparent Minco heater.

This base can be sealed either by compressing double-sided Kapton tape between the two sections of the stage, or by coating the base with PDMS. The cell culture wells can then be fit on top of this base with a custom-cut double-sided Kapton tape gasket or other liquid-tight seal such as PDMS, on top of which is fixed the AeraSeal and gas flow chamber as described previously. The well on an optical measurement stage is shown in rightmost image. This image also shows the Kapton resistive heater and gas flow inlet and outlets, as well as the optical fiber used to

interrogate the edge-coupled devices. A transparent Minco resistive heater may also be used to allow imaging of the hydrogel profile as it is contracted.

Once the temperature control of this system was optimized, a viability experiment was performed with 1 million/mL NDHF in 3 mg/mL collagen over 24 h. Three sets of three custom cell culture wells were compared under different conditions. One was maintained on the benchtop using the resistive heating and gas/humidity flow system described previously. One was covered with an AeraSeal and placed in a cell culture incubator, a positive control. The third was covered with an AeraSeal and placed on the benchtop with no environmental control, a negative control. After 24 hours of cell culture in the environmental chambers, gels were removed and placed in nunc chambers. Gels were rinsed with 1X PBS and, using standard protocols, stained with syto-13, propidium iodide, and Hoescht blue as live, dead, and nuclei stains, respectively. Maximum intensity projections of 100 μm z-stacks were at 10x magnification taken of each gel with an LSM 710 confocal microscope. Representative images of the results are shown in Figure 36.

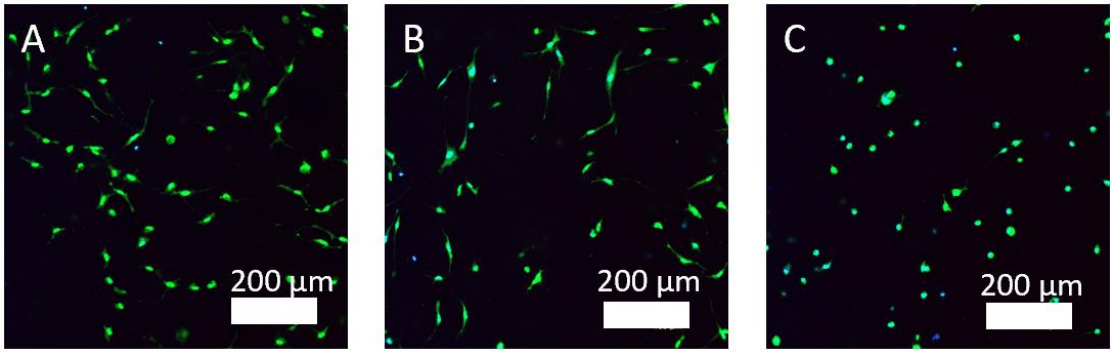

Figure 36: Maximum intensity projection of 100 µm z-stacks taken of live/dead stained NDHF cultured in 3 mg/mL collagen for 24h. The cell culture conditions utilized were: A) a custom benchtop environmental control chamber, B) a cell culture incubator, C) no environmental control.

In order to quantify this, the images taken from each culture condition were processed in FIJI, ImageJ. Each of the three color channels of each image were processed separately, each auto-thresholded with a triangle filter, converted to black and white, binary, 8-bit images. A standard watershed filter was applied to separate adjacent cells. Using the analyze particles feature in FIJI, the cell count in the whole image was calculated from the blue channel, which displayed the nuclei stain. The cell viability was calculated as the percentage of dead cells determined by the ratio of dead cells to total nuclei. No significant difference was observed in cell viability from these data, however significant differences were observed in the morphology and cell count. These data are summarized in Figure 37.

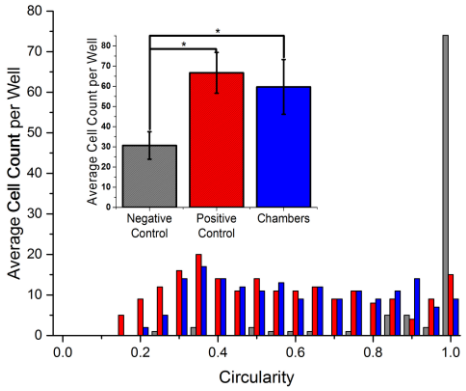

Figure 37: The number of cells with a given circularity cultured under each condition. Inset shows the cell count per well in the negative and positive control wells and the chambers with custom environmental control. The colors of the binned data in the circularity plot correspond to the meaning of the colors of the bars in the inset. $p < 0.03$, Student's TTest.

From these data we can observe that the cell cultures in both the positive control and chambers showed no statistically significant difference in cell count, however both had a statistically significantly higher cell count than in the negative control. Qualitatively, we observe that the circularity of the cells in the negative control is much higher than in the positive control and chambers. Since we observe that proliferating cells exhibit a spread morphology in this cell culture system, high circularity likely indicates that they are near apoptosis.

This experiment was followed by a replicate of this study, this time comparing the metabolic activity of the cells at the start and finish of the 24 hours (Figure 38). Here, we can observe that the metabolic activity in the chambers and positive control are not statistically significantly different from one another, while both are statistically significantly greater than metabolic activity in the negative control. This correlates

well with the first experiment, in which a more spread cell morphology and higher cell count were observed in the chambers and positive control.

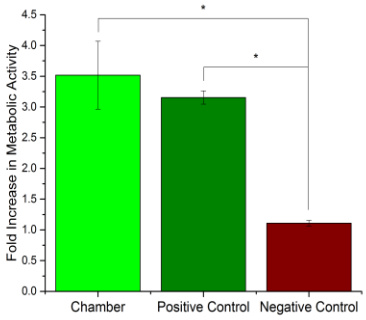

Figure 38: Metabolic activity study of 1 million/mL NDHF in 3 mg/mL collagen after 24 hours. Normalized to the metabolic activity in the negative control at the start of the study. $p < 0.01$, Student's TTest.

7.2.4 Incubator Integration

As previously mentioned, this benchtop chamber was designed for the use of the device on an optical table on which the device was aligned to distinct lensed optical fibers for input and output coupling. In practice, this alignment method was not well-suited to these devices. To help ensure that the optical fibers did not interact with the Kapton tape holding the device array onto its handler, this setup required that a part of the edge platform of the array jut out from the holder with no mechanical support. The flexibility of the SU-8 meant that in this configuration the edges of the device were effected by the air handling in the lab, making alignment unreliable.

In order to overcome this limitation, an array which was interrogated by fiber bundles bonded with epoxy to input and output grating couplers was designed (Figure 39).

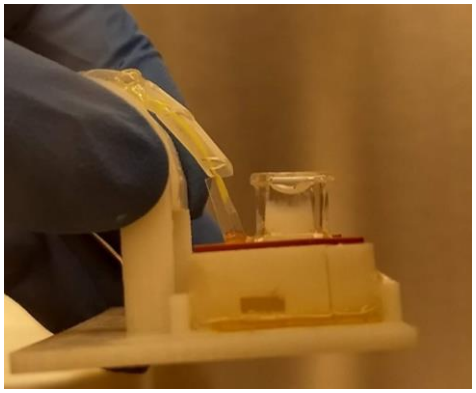

Figure 39: Fiber bundle-interrogated array encased in a hydrogel in a glass well.

Figure 39 shows this modified setup with a single well filled with hydrogel. This bundle contains 8 fibers and is therefore capable of interrogating 4 channels at once (input and output). One of these devices is a straight waveguide on the edge platform of the array only used to align the grating coupler before bonding. Each of the other 3 interrogate a waveguide strip. Other fiber bundle configurations could be used to interrogate any number of channels.

This design has the added benefit of being able to be used in a cell culture incubator. This greatly reduces the cost and time spent to optimize the environmental control around the devices and makes the device usable by any biologist familiar with 3D cell culture. With the proper laser and switching system, and programs to control them, this has the potential to be a ‘plug and play’ platform.

With this new versatility in mind, additional design modifications were made to improve the usefulness of this system. The device holder could now be 3D printed since it did not need to be machined in order to integrate it with an optical measurement stage. This allowed us to add an arm to hold the optical fiber bundle so as to not put excess strain on the epoxy bond site. Since the device did not need to be wrapped in a resistive heater to maintain temperature, the wells were refabricated from diced glass slides joined with PDMS, which was baked quickly at a high temperature (110 °C) to ensure that the PDMS did not flow into the device well before setting. These clear wells allowed qualitative observations in gel contraction to be recorded during experiments.

7.3 Contracting Collagen Experiment

Issues with reproducibility of the etching of the GSS waveguides on the ICP/RIE systems in Boston limited the reproducibility in fabricating working device arrays. However here I describe a proof-of-concept experiment utilizing single resonators on two separate arrays in order to determine the contraction of NDHF-laden collagen over 12 hours.

7.3.1 Experimental Setup

In this study, glass/PDMS wells were attached to two device arrays on 3D-printed holders as in Figure 39. Each array bore a single waveguide that interrogated two functioning ring resonators, one off of the buckle intended to function as a thermometer, and the other at the highest point on the buckle. Initial attempts to characterize the thermo-optic responses of these resonators indicated that the device's

aging behavior had not yet stabilized. An example of the sub-optimum thermo-optic response is shown in Figure 40.

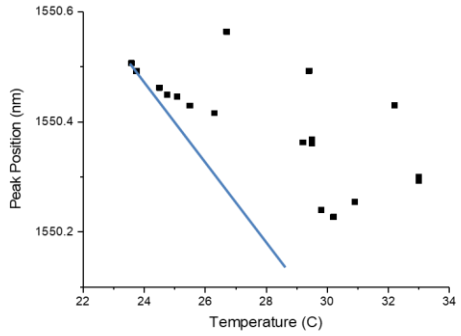

Figure 40: Poor thermo-optic response of unstabilized device. Blue line indicates expected trend.

After attaching the well to the device, the array was photo-saturated with a broadband lamp for approximately 6 weeks in order to stabilize its index shift. Photo-saturation was selected because this experiment was performed prior to the aging study performed in Chapter 4. After photo-saturation, the index shift with temperature was stable over time, however it showed some hysteresis, and the temperature shift in the edge and on-buckle devices did not correlate well. We predict that this is due to some relaxation effects in the PDMS, which partially covers the edge ‘thermometer’ resonator. Instead, we chose to place the devices in the cell culture incubator for 12 hours to observe the peak shift of the resonator on the buckle due to temperature fluctuations. The results of this study are shown in Figure 41A. We observed peaks

shifts of less than 40 pm, which from our previous studies of collagen contraction we predict would be far less than than the peak shifts due to strain in the gel.

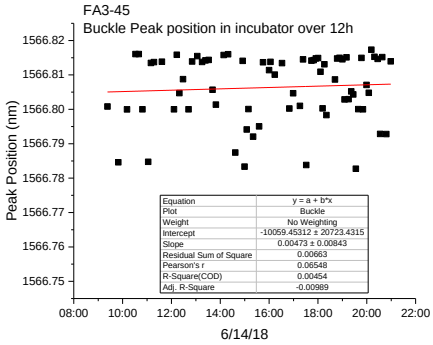

Figure 41: Temperature fluctuations in a device kept in a cell culture incubator for 12 hours.

This prediction was verified experimentally. Two device wells were filled halfway with a 3.5 mg/mL collagen gel populated. One was populated with 1 million/mL fibroblasts, and the other studied without cells as a control. Eight-well nunc chambers were filled with 3 gels each with and without cells of the same gel volume used in the device chambers (250 μL). The collagen gel adhered well to the base of the nunc chambers, but not to the base of the device wells. To prevent the gels from floating, a scalpel was used to randomly texture the base of the device wells.

The viscosity of the pre-crosslinked collagen was low enough to flow around the sensors, and it formed an opaque gel after 30 minutes of incubation. The dimensions of these nunc chambers were close to that of the device wells. After the collagen cross-linked, A scalpel was run around the edge of each gel to release it from

the sides. This was mostly done to prevent formation of a meniscus, which was more difficult to model in COMSOL for our comparison simulation.

ATTC low-growth fibroblast growth media with 1% PS was added to the device and nunc wells. The device wells were placed in one incubator, with the doors sealed with extra caulking putty to block any gaps made by the input and output optical fibers. These devices were interrogated by a HP816 NIR tunable laser controlled with a custom-made labview program. Since we did not want to introduce any large temperature fluctuations to the device wells during the study, the gels in the nunc chamber were placed in a different incubator. These were used as a semi-quantitative platform to predict the amount of strain experienced by the sensors in contracting gels. At regular timepoints throughout the study, the nunc chambers were removed from their incubator, and the gels imaged from the side and top. These images were analyzed in imageJ to determine the amount of deformation of the gels.

Over the time of the study we indeed observe that the peak shift due to strain is greater than the noise in the system (Figure 42). From the calibration study described in Chapter 6.2.2, we estimate that the total peak shift corresponds to approximately 0.06% strain in the device over the course of the experiment.

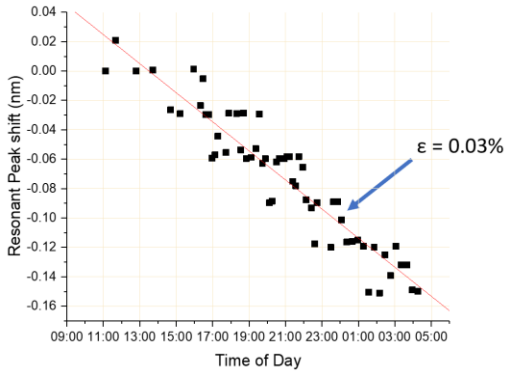

Figure 42: Resonant peak shift of device encased in 3.5 mg/mL collagen populated with 1 million/mL NDHF.

Using the deformation measured in the comparison gels, we can compare the expected strain to the actual strain in the device. We selected the timepoint at which the resonant peak shift indicated 0.03% strain at the device. A FEM was built in COMSOL 4.2 in which the symmetric SU8 buckle was embedded in a collagen gel-like environment. The change in gel geometry observed in the gel in the nunc chamber at that timepoint was imparted on the FEM gel. This deformation at this timepoint was less than 10%, and thus we approximated the gel as a linear elastic, isotropic material as we had in the previous studies. A modulus of 2 kPa was chosen based on previous studies quantifying collagen moduli containing similar fibroblast populations and collagen concentration [32]. An image showing two of the three gels imaged at this timepoint, and the FEM model built from the average deformation in all three images, is shown in Figure 43. The strain at the center of the buckle in this system was 0.016%, approximately half of what was observed.

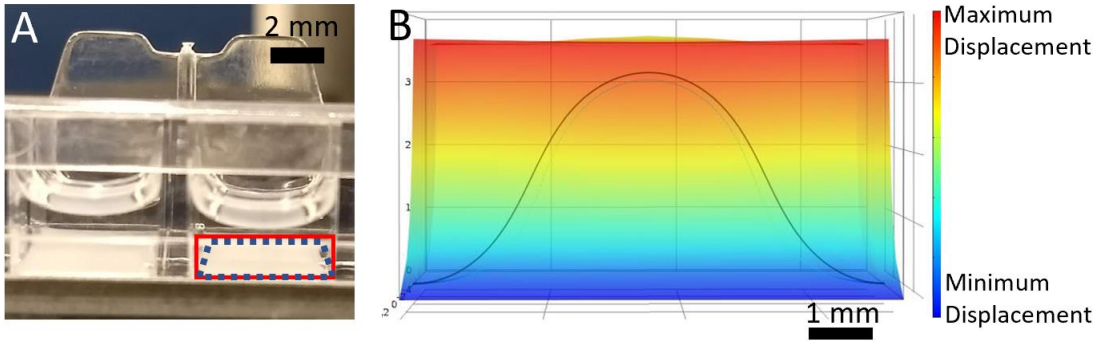

Figure 43: Deformation of a collagen hydrogel tethered to the bottom of its well A) *in vitro*, and B) in a finite element model. In A), the red box indicates the original gel geometry, and the blue dotted trapezoid shows the deformed gel geometry.

There are a number of limitations to this proof-of-concept experiment that could have led to this higher strain in the buckle. Both the experimental and control wells containing devices in this study leaked. The control leak was likely due to improper sealing, as the strain in this buckle decreased linearly throughout the whole study. The leak in the experimental well likely occurred when the well tipped over partway through the study, however it cannot be confirmed that this well was not also dehydrating previously. We believe the well tipped over at 17 hours after the start of the study, due to some abrupt fluctuations in the device peak shifts at that time. Figure 42 only shows data previous to that event. Dehydration would have increased the modulus of the hydrogel beyond the value predicted and used for the FEM and would have more rapidly deformed the gel.

More optimization and leak tests of these chambers have been performed that show excellent stability over 24 hours. More generous application of the PDMS sealant or use of silicone gaskets are good options for making these wells. In future

experiments with these devices, physically attaching the device holders to the incubator shelves would also be advisable. Placement of the temperature tracking device farther off the buckle would also ensure that it was not being affected by the well adhesive during the experiment, which should allow us to use it as a thermometer. We could then open the incubator doors during the experiment to check the device and account for the large temperature fluctuations using that calibrated thermometer.

Overall, this proof-of-concept experiment showed deformation of the buckled device on the same order of magnitude as that predicted by Finite Element Modeling. The initial integration of the devices with the collagen was successful, and the measurements and setup were facile to implement and compatible with traditional 3D cell culture methods.

Chapter 8

SUMMARY AND FUTURE WORK

This work describes the design, fabrication, and integration of polymer or deterministically buckled silicone-clad GSS ChGs resonant cavity arrays that may be applied in the detection of relevant local cell- to tissue-scale strains in 3D tissue models. This is in response to the need for non-destructive, highly strain-sensitive platforms to study thick *in vitro* systems that can pave the way toward the development of wound healing therapies.

8.1 Summary

The use of chalcogenide glass resonant cavities for strain detection *in vitro* has distinct challenges that were addressed in this work. Firstly, the sub-T_g relaxation of chalcogenide glasses negatively impacts the reliability of our devices, as their record sensitivity to strain-induced index change also means that they are extremely sensitive to aging-induced index changes. In Chapter 4, we addressed this issue with the development of a novel, high-precision refractometry technique with which the aging mechanisms in the glass was determined with high accuracy. Further, this technique was used to compare annealed and photo-saturated devices to a control sample to determine the post-processing techniques that best stabilize GSS relaxation before use.

In Chapter 5, the careful selection of the device array design parameters in order to meet our target resolutions is discussed. In particular the development of robust fabrication methods to ensure reproducibility and compatibility with our

devices' final application was discussed. We then demonstrate the fabrication of a proof-of-concept SU8-clad buckled ring resonator array.

In Chapter 6, we demonstrate this proof-of-concept device's sensitivity to relevant strains by calibrating the device's response to compression and proposing higher accuracy calibration experiments that would allow us to characterize their strain response. A FEM of an idealized silicone-clad device in cardiac graft tissue-like environment is also developed in order to demonstrate our device's sensitivity to relevant stiffness caused by perfusion limits in a cyclically strained tissue model.

The integration of photonic devices *in vitro* requires precise environmental control, in particular the control of humidity, CO_2 concentration, and temperature around the device array. The device is submerged in a hydrated gel, and thus must be kept in a watertight container in order to support cell culture around the device. These specific challenges were addressed in Chapter 7, in which environmental control systems and device interrogation methods were optimized, and a demonstration of our proof-of-concept device as a 'plug-and-play' *in vitro* strain detection method is shown.

Table 2 provides a visual comparison of the pros and cons of a PDMS-clad buckled resonant cavity array versus other best methods of *in vitro* strain or stiffness detection discussed in Chapter 1. It is apparent that the dimensionality, strain resolution, measurable volume, and measurement speed of our platform is comparable to the best strain or force detection techniques, and the somewhat limited spatial resolution of our devices is well within the range of interest for our applications.

Table 2: Comparison of methods of tracking *in vitro* changes in strain or stiffness.

Table color ranks the characteristics of each method in three groups, with green indicating best performance, yellow intermediate, and red the least impressive. Additional references provided the values shown [182, 183]

Method	Dimensionality	Strain/force resolution	Spatial resolution	Needs Microscopy?	Measurable Volume/Area	Measurement Speed
Ours	3D	1 nN	10 µm	N	mm^3	seconds
2-D TFM [184]	2D	1 nN	1 µm	Y	mm^2	minutes-hours
3-D TFM [185]	3D	10 nN	1 µm	Y	< mm^3	minutes-hours
Collagen Contraction [159, 23]	3D	10 µN	1/sample	N	mm^3	seconds
Micropillars [17]	2D	0.01-100 nN	1 µm	Y	mm^2	seconds
DVC [33] (MRI, etc.)	3D	0.01%	1 µm	N	mm^3-cm^3	hours

8.2 Future Work

Overall, future work on this project would expand its scope beyond proof-of-concept and utilize this device array in relevant *in vitro* applications. The integration of device arrays bearing multiple functioning device strips in contracting hydrogels with uniform modulus, or with gradient mechanical or chemical properties that direct cell migration, would allow us to build maps of local strain in densely interrogated tissue models.

Some other specific aims of this project could be expanded upon. The resonant refractometry technique described in Chapter 4 could be utilized for other chalcogenide glass materials. It could also be used to compare specific annealing or

photo-saturation conditions to find the optimal post-processing treatment for ChG devices to reduce their aging-induced wavelength shift.

In order to expand the amenability of these devices to integration, the fabrication of an ‘array of arrays’ in which multiple groups of devices are accessed through the same cluster of grating couplers, or through arrayed waveguide gratings, would enable the user to perform such studies with necessary biological repeats and controls. Furthermore, these devices could find use embedded in other material systems. For example liquids for the study of fluid flow and dental filling materials or implant cements for the study of mechanical stress in fillings and implant joints. The flexibility of these devices, both literally and in terms of their adaptability to various *in vitro* applications and beyond, makes our technique a significant addition to the host of tools that already exist for 3D mapping the mechanical properties and deformations of soft and biologically relevant materials.

REFERENCES

1. Gudmundsson KG, Arngrímsson R, Sigfússon N, Björnsson Á, Jónsson T. Epidemiology of Dupuytren's disease: Clinical, serological, and social assessment. The Reykjavik Study. Journal of Clinical Epidemiology. 2000;53(3):291-6. doi:https://doi.org/10.1016/S0895-4356(99)00145-6.
2. Hurst LC, Badalamente MA, Hentz VR, Hotchkiss RN, Kaplan FTD, Meals RA et al. Injectable Collagenase Clostridium Histolyticum for Dupuytren's Contracture. 2009;361(10):968-79. doi:10.1056/NEJMoa0810866.
3. Vunjak-Novakovic G, Tandon N, Godier A, Maidhof R, Marsano A, Martens TP et al. Challenges in cardiac tissue engineering. 2009;16(2):169-87.
4. Pecha S, Eschenhagen T, Reichenspurner H. Myocardial tissue engineering for cardiac repair. J Heart Lung Transplant. 2016;35(3):294-8. doi:10.1016/j.healun.2015.12.007.
5. Ogle BM, Bursac N, Domian I, Huang NF, Menasché P, Murry CE et al. Distilling complexity to advance cardiac tissue engineering. 2016;8(342):342ps13-ps13.
6. Benninger MS, Alessi D, Archer S, Bastian R, Ford C, Koufman J et al. Vocal fold scarring: Current concepts and management. Otolaryngology-Head and Neck Surgery. 1996;115(5):474-82. doi:10.1016/s0194-5998(96)70087-6.
7. Jia XQ, Yeo Y, Clifton RJ, Jiao T, Kohane DS, Kobler JB et al. Hyaluronic acid-based microgels and microgel networks for vocal fold regeneration. Biomacromolecules. 2006;7(12):3336-44. doi:10.1021/bm0604956.
8. Tomasek JJ, Gabbiani G, Hinz B, Chaponnier C, Brown RA. Myofibroblasts and mechano-regulation of connective tissue remodelling. Nature Reviews Molecular Cell Biology. 2002;3(5):349-63. doi:10.1038/nrm809.
9. Wynn TA. Cellular and molecular mechanisms of fibrosis. Journal of Pathology. 2008;214(2):199-210. doi:10.1002/path.2277.
10. Castilho M, Hochleitner G, Wilson W, van Rietbergen B, Dalton PD, Groll J et al. Mechanical behavior of a soft hydrogel reinforced with three-dimensional printed microfibre scaffolds. Sci Rep. 2018;8(1):1245. doi:10.1038/s41598-018-19502-y.
11. Wang L, Li Y, Huang G, Zhang X, Pingguan-Murphy B, Gao B et al. Hydrogel-based methods for engineering cellular microenvironment with spatiotemporal gradients. Crit Rev Biotechnol. 2016;36(3):553-65. doi:10.3109/07388551.2014.993588.
12. Lutolf MP, Hubbell JA. Synthetic biomaterials as instructive extracellular microenvironments for morphogenesis in tissue engineering. Nat Biotechnol. 2005;23(1):47-55. doi:10.1038/nbt1055.

13. Harris AK, Wild P, Stopak DJS. Silicone rubber substrata: a new wrinkle in the study of cell locomotion. 1980;208(4440):177-9.
14. Lee J. Traction forces generated by locomoting keratocytes. The Journal of Cell Biology. 1994;127(6):1957-64. doi:10.1083/jcb.127.6.1957.
15. Wang JH, Lin JS. Cell traction force and measurement methods. Biomech Model Mechanobiol. 2007;6(6):361-71. doi:10.1007/s10237-006-0068-4.
16. Schoen I, Hu W, Klotzsch E, Vogel V. Probing cellular traction forces by micropillar arrays: contribution of substrate warping to pillar deflection. Nano Lett. 2010;10(5):1823-30. doi:10.1021/nl100533c.
17. Ghibaudo M, Saez A, Trichet L, Xayaphoummine A, Browaeys J, Silberzan P et al. Traction forces and rigidity sensing regulate cell functions. Soft Matter. 2008;4(9). doi:10.1039/b804103b.
18. Pampaloni F, Reynaud EG, Stelzer EHK. The third dimension bridges the gap between cell culture and live tissue. Nature Reviews Molecular Cell Biology. 2007;8(10):839-45. doi:10.1038/nrm2236.
19. Tibbitt MW, Anseth KS. Hydrogels as Extracellular Matrix Mimics for 3D Cell Culture. Biotechnology and Bioengineering. 2009;103(4):655-63. doi:10.1002/bit.22361.
20. Bell E, Ivarsson B, Merrill CJPotNAoS. Production of a tissue-like structure by contraction of collagen lattices by human fibroblasts of different proliferative potential in vitro. 1979;76(3):1274-8.
21. Schafer IA, Shapiro A, Kovach M, Lang C, Fratianne RBJEcr. The interaction of human papillary and reticular fibroblasts and human keratinocytes in the contraction of three-dimensional floating collagen lattices. 1989;183(1):112-25.
22. Grinnell F, Ho C-H, Lin Y-C, Skuta GJJoBC. Differences in the regulation of fibroblast contraction of floating versus stressed collagen matrices. 1999;274(2):918-23.
23. Campbell BH, Clark WW, Wang JHJJob. A multi-station culture force monitor system to study cellular contractility. 2003;36(1):137-40.
24. Legant WR, Miller JS, Blakely BL, Cohen DM, Genin GM, Chen CS. Measurement of mechanical tractions exerted by cells in three-dimensional matrices. Nature Methods. 2010;7:969. doi:10.1038/nmeth.1531 https://www.nature.com/articles/nmeth.1531#supplementary-information.
25. Steinwachs J, Metzner C, Skodzek K, Lang N, Thievessen I, Mark C et al. Three-dimensional force microscopy of cells in biopolymer networks. Nature Methods. 2015;13:171. doi:10.1038/nmeth.3685 https://www.nature.com/articles/nmeth.3685#supplementary-information.
26. Hall MS, Long R, Feng X, Huang Y, Hui C-Y, Wu M. Toward single cell traction microscopy within 3D collagen matrices. Experimental Cell Research. 2013;319(16):2396-408. doi:https://doi.org/10.1016/j.yexcr.2013.06.009.

27. Griffith CK, Miller C, Sainson RC, Calvert JW, Jeon NL, Hughes CC et al. Diffusion limits of an in vitro thick prevascularized tissue. Tissue engineering. 2005;11(1-2):257-66.
28. Serpooshan V, Julien M, Nguyen O, Wang H, Li A, Muja N et al. Reduced hydraulic permeability of three-dimensional collagen scaffolds attenuates gel contraction and promotes the growth and differentiation of mesenchymal stem cells. Acta Biomater. 2010;6(10):3978-87. doi:10.1016/j.actbio.2010.04.028.
29. Leong KF, Chua CK, Sudarmadji N, Yeong WY. Engineering functionally graded tissue engineering scaffolds. J Mech Behav Biomed Mater. 2008;1(2):140-52. doi:10.1016/j.jmbbm.2007.11.002.
30. Cox MA, Driessen NJ, Boerboom RA, Bouten CV, Baaijens FP. Mechanical characterization of anisotropic planar biological soft tissues using finite indentation: experimental feasibility. J Biomech. 2008;41(2):422-9. doi:10.1016/j.jbiomech.2007.08.006.
31. Gupta S, T G, Basu B, Goswami S, Sinha A. Stiffness- and wettability-dependent myoblast cell compatibility of transparent poly(vinyl alcohol) hydrogels. J Biomed Mater Res B Appl Biomater. 2013;101(2):346-54. doi:10.1002/jbm.b.32845.
32. Ahearne M, Wilson SL, Liu KK, Rauz S, El Haj AJ, Yang Y. Influence of cell and collagen concentration on the cell-matrix mechanical relationship in a corneal stroma wound healing model. Exp Eye Res. 2010;91(5):584-91. doi:10.1016/j.exer.2010.07.013.
33. Xu H, Othman SF, Magin RL. Monitoring tissue engineering using magnetic resonance imaging. J Biosci Bioeng. 2008;106(6):515-27. doi:10.1263/jbb.106.515.
34. Manduca A, Oliphant TE, Dresner MA, Mahowald JL, Kruse SA, Amromin E et al. Magnetic resonance elastography: Non-invasive mapping of tissue elasticity. Medical Image Analysis. 2001;5(4):237-54. doi:https://doi.org/10.1016/S1361-8415(00)00039-6.
35. Othman SF, Xu H, Royston TJ, Magin RL. Microscopic magnetic resonance elastography (μMRE). Magnetic Resonance in Medicine: An Official Journal of the International Society for Magnetic Resonance in Medicine. 2005;54(3):605-15.
36. Vappou J, Breton E, Choquet P, Goetz C, Willinger R, Constantinesco A. Magnetic resonance elastography compared with rotational rheometry for in vitro brain tissue viscoelasticity measurement. Magnetic Resonance Materials in Physics, Biology
Medicine. 2007;20(5):273. doi:10.1007/s10334-007-0098-7.
37. Kozdras A. Kinetics of light-assisted physical ageing in S-rich arsenic sulphide glasses. Bulletin of Materials Science. 2016;39(4):997-1000. doi:10.1007/s12034-016-1252-5.
38. Li L, Lin H, Qiao S, Zou Y, Danto S, Richardson K et al. Integrated flexible chalcogenide glass photonic devices. Nature Photonics. 2014;8:643. doi:10.1038/nphoton.2014.138
https://www.nature.com/articles/nphoton.2014.138#supplementary-information.

39. Li L, Lin H, Qiao S, Huang Y-Z, Li J-Y, Michon J et al. Monolithically integrated stretchable photonics. 2018;7(2):17138.
40. Alt MT, Fiedler E, Rudmann L, Ordonez JS, Ruther P, Stieglitz T. Let There Be Light—Optoprobes for Neural Implants. Proceedings of the IEEE. 2017;105(1):101-38. doi:10.1109/JPROC.2016.2577518.
41. Pashaie R, Anikeeva P, Lee JH, Prakash R, Yizhar O, Prigge M et al. Optogenetic Brain Interfaces. IEEE Reviews in Biomedical Engineering. 2014;7:3-30. doi:10.1109/RBME.2013.2294796.
42. Yetisen AK, Martinez-Hurtado JL, Unal B, Khademhosseini A, Butt H. Wearables in Medicine. Adv Mater. 2018:e1706910. doi:10.1002/adma.201706910.
43. Ok JG, Seok Youn H, Kyu Kwak M, Lee K-T, Jae Shin Y, Jay Guo L et al. Continuous and scalable fabrication of flexible metamaterial films via roll-to-roll nanoimprint process for broadband plasmonic infrared filters. Applied Physics Letters. 2012;101(22):223102.
44. Bruck R, Muellner P, Kataeva N, Koeck A, Trassl S, Rinnerbauer V et al. Flexible thin-film polymer waveguides fabricated in an industrial roll-to-roll process. Appl Opt. 2013;52(19):4510-4. doi:10.1364/AO.52.004510.
45. Aikio S, Hiltunen J, Hiitola-Keinanen J, Hiltunen M, Kontturi V, Siitonen S et al. Disposable photonic integrated circuits for evanescent wave sensors by ultra-high volume roll-to-roll method. Opt Express. 2016;24(3):2527-41. doi:10.1364/oe.24.002527.
46. Cai SS, Han ZY, Wang FL, Zheng KW, Cao Y, Ma YJ et al. Review on flexible photonics/electronics integrated devices and fabrication strategy. Sci China-Inf Sci. 2018;61(6):27. doi:10.1007/s11432-018-9442-3.
47. Shneidman AV, Becker KP, Lukas MA, Torgerson N, Wang C, Reshef O et al. All-Polymer Integrated Optical Resonators by Roll-to-Roll Nanoimprint Lithography. Acs Photonics. 2018;5(5):1839-+. doi:10.1021/acsphotonics.8b00022.
48. Abaya TVF, Diwekar M, Blair S, Tathireddy P, Rieth L, Solzbacher F, editors. Deep-tissue light delivery via optrode arrays2014: SPIE.
49. Jain A, Yang AHJ, Erickson D. Gel-based optical waveguides with live cell encapsulation and integrated microfluidics. Optics Letters. 2012;37(9):1472-4. doi:10.1364/OL.37.001472.
50. Shabahang S, Kim S, Yun SH. Light-Guiding Biomaterials for Biomedical Applications. Advanced Functional Materials. 2018;28(24):17. doi:10.1002/adfm.201706635.
51. Manocchi AK, Domachuk P, Omenetto FG, Yi HM. Facile Fabrication of Gelatin-Based Biopolymeric Optical Waveguides. Biotechnology and Bioengineering. 2009;103(4):725-32. doi:10.1002/bit.22306.
52. Choi M, Choi JW, Kim S, Nizamoglu S, Hahn SK, Yun SH. Light-guiding hydrogels for cell-based sensing and optogenetic synthesis in vivo. Nature Photonics. 2013;7:987. doi:10.1038/nphoton.2013.278 https://www.nature.com/articles/nphoton.2013.278#supplementary-information.

53. Choi M, Humar M, Kim S, Yun SH. Step-index optical fiber made of biocompatible hydrogels. Advanced Materials. 2015;27(27):4081-6.
54. Applegate MB, Brenckle MA, Marelli B, Tao H, Kaplan DL, Omenetto FG. Silk: a different kind of “fiber optics”. Optics Photonics News. 2014;25(6):28-35.
55. Choi C, Lin L, Yujie L, Jinho C, Li W, Haas D et al. Flexible optical waveguide film fabrications and optoelectronic devices integration for fully embedded board-level optical interconnects. Journal of Lightwave Technology. 2004;22(9):2168-76. doi:10.1109/JLT.2004.833815.
56. Bhola B, Song H-C, Tazawa H, Steier WH. Polymer microresonator strain sensors. IEEE Photonics Technology Letters. 2005;17(4):867-9.
57. Kim K-J, Seo J-K, Oh M-C. Strain induced tunable wavelength filters based on flexible polymer waveguide Bragg reflector. Opt Express. 2008;16(3):1423-30.
58. Li RZ, Zhang LJ, Hu W, Wang LD, Tang J, Zhang T. Flexible TE-Pass Polymer Waveguide Polarizer With Low Bending Loss. Ieee Photonics Technology Letters. 2016;28(22):2601-4. doi:10.1109/lpt.2016.2606505.
59. Maeda Y, Hashiguchi Y, editors. Flexible film waveguides with excellent bending properties. Photonics Packaging, Integration, and Interconnects VIII; 2008: International Society for Optics and Photonics.
60. Kinoshita R, Suganuma D, Ishigure T. Accurate interchannel pitch control in graded-index circular-core polymer parallel optical waveguide using the Mosquito method. Opt Express. 2014;22(7):8426-37.
61. Cai DK, Neyer A. Polysiloxane based flexible electrical–optical-circuits-board. Microelectronic Engineering. 2010;87(11):2268-74. doi:https://doi.org/10.1016/j.mee.2010.02.014.
62. To C, Hellebrekers T, Jung J, Yoon SJ, Park Y. A Soft Optical Waveguide Coupled With Fiber Optics for Dynamic Pressure and Strain Sensing. IEEE Robotics and Automation Letters. 2018;3(4):3821-7. doi:10.1109/LRA.2018.2856937.
63. Lostutter CK, Hodge MH, Marrapode TR, Swatowski BW, Weidner WK, editors. Assembly and performance of silicone polymer waveguides. SPIE OPTO; 2016: SPIE.
64. al. RSEJe. "Thermally Stable, Low Loss Optical Silicones: A Key Enabler for Electro-Optical Printed Circuit Boards,". Journal of Lightwave Technology.33(4):814-9.
65. Reddy JW, Chamanzar M. Low-loss flexible Parylene photonic waveguides for optical implants. Optics Letters. 2018;43(17):4112-5. doi:10.1364/OL.43.004112.
66. Ma H, Jen AY, Dalton LR. Polymer-based optical waveguides: materials, processing, and devices. Advanced materials. 2002;14(19):1339-65.
67. Fan L, Varghese LT, Xuan Y, Wang J, Niu B, Qi M. Direct fabrication of silicon photonic devices on a flexible platform and its application for strain sensing. Opt Express. 2012;20(18):20564-75. doi:10.1364/OE.20.020564.
68. Vernoux C, Chen Y, Markey L, Spârchez C, Arocas J, Felder T et al. Flexible long-range surface plasmon polariton single-mode waveguide for optical interconnects. Opt Mater Express. 2018;8(2):469-84. doi:10.1364/OME.8.000469.

69. Chen Y, Li H, Li M. Flexible and tunable silicon photonic circuits on plastic substrates. Scientific reports. 2012;2:622.
70. Ghaffari A, Hosseini A, Xu X, Kwong D, Subbaraman H, Chen RT. Transfer of micro and nano-photonic silicon nanomembrane waveguide devices on flexible substrates. Opt Express. 2010;18(19):20086-95.
71. Li L, Zhang P, Wang W-M, Lin H, Zerdoum AB, Geiger SJ et al. Foldable and cytocompatible sol-gel TiO_2 photonics. Scientific reports. 2015;5:13832.
72. Du Q, Luo Z, Zhong H, Zhang Y, Huang Y, Du T et al. Chip-scale broadband spectroscopic chemical sensing using an integrated supercontinuum source in a chalcogenide glass waveguide. Photon Res. 2018;6(6):506-10. doi:10.1364/PRJ.6.000506.
73. Su P, Han Z, Kita D, Becla P, Lin H, Deckoff-Jones S et al. Monolithic on-chip mid-IR methane gas sensor with waveguide-integrated detector. Applied Physics Letters. 2019;114(5):051103.
74. Serna S, Lin H, Alonso-Ramos C, Yadav A, Le Roux X, Richardson K et al. Nonlinear optical properties of integrated GeSbS chalcogenide waveguides. Photon Res. 2018;6(5):B37-B42. doi:10.1364/PRJ.6.000B37.
75. Asobe M. Nonlinear Optical Properties of Chalcogenide Glass Fibers and Their Application to All-Optical Switching. Optical Fiber Technology. 1997;3(2):142-8. doi:https://doi.org/10.1006/ofte.1997.0214.
76. Ta'eed VG, Baker NJ, Fu L, Finsterbusch K, Lamont MRE, Moss DJ et al. Ultrafast all-optical chalcogenide glass photonic circuits. Opt Express. 2007;15(15):9205-21. doi:10.1364/OE.15.009205.
77. Tremblay J-É, Malinowski M, Richardson KA, Fathpour S, Wu MC. Picojoule-level octave-spanning supercontinuum generation in chalcogenide waveguides. Opt Express. 2018;26(16):21358-63. doi:10.1364/OE.26.021358.
78. Petersen CR, Prtljaga N, Farries M, Ward J, Napier B, Lloyd GR et al. Mid-infrared multispectral tissue imaging using a chalcogenide fiber supercontinuum source. Optics Letters. 2018;43(5):999-1002. doi:10.1364/OL.43.000999.
79. Yu Y, Gai X, Wang T, Ma P, Wang R, Yang Z et al. Mid-infrared supercontinuum generation in chalcogenides. Opt Mater Express. 2013;3(8):1075-86. doi:10.1364/OME.3.001075.
80. Chen F, Aldana JRV. Optical waveguides in crystalline dielectric materials produced by femtosecond-laser micromachining. Laser & Photonics Reviews. 2014;8(2):251-75. doi:10.1002/lpor.201300025.
81. Vázquez MR, Sotillo B, Rampini S, Bharadwaj V, Gholipour B, Fernández P et al. Femtosecond laser inscription of nonlinear photonic circuits in Gallium Lanthanum Sulphide glass. Journal of Physics: Photonics. 2018;1(1):015006. doi:10.1088/2515-7647/aade60.
82. Arriola A, Gross S, Ams M, Gretzinger T, Le Coq D, Wang RP et al. Mid-infrared astrophotonics: study of ultrafast laser induced index change in compatible materials. Opt Mater Express. 2017;7(3):698-711. doi:10.1364/OME.7.000698.

83. Lapointe J, Ledemi Y, Loranger S, Iezzi VL, Soares de Lima Filho E, Parent F et al. Fabrication of ultrafast laser written low-loss waveguides in flexible As_2S_3 chalcogenide glass tape. Optics Letters. 2016;41(2):203-6. doi:10.1364/OL.41.000203.
84. Huang CC, Hewak DW, Badding JV. Deposition and characterization of germanium sulphide glass planar waveguides. Opt Express. 2004;12(11):2501-6. doi:10.1364/OPEX.12.002501.
85. Stone A, Jain H, Dierolf V, Sakakura M, Shimotsuma Y, Miura K et al. Direct laser-writing of ferroelectric single-crystal waveguide architectures in glass for 3D integrated optics. Scientific Reports. 2015;5:10391. doi:10.1038/srep10391.
86. Sabapathy T, Ayiriveetil A, Kar AK, Asokan S, Beecher SJ. Direct ultrafast laser written C-band waveguide amplifier in Er-doped chalcogenide glass. Opt Mater Express. 2012;2(11):1556-61. doi:10.1364/OME.2.001556.
87. Hu J, Tarasov V, Carlie N, Petit L, Agarwal A, Richardson K et al. Exploration of waveguide fabrication from thermally evaporated Ge–Sb–S glass films. Optical Materials. 2008;30(10):1560-6. doi:https://doi.org/10.1016/j.optmat.2007.10.002.
88. Mittal V, Aghajani A, Carpenter LG, Gates JC, Butement J, Smith PGR et al. Fabrication and characterization of high-contrast mid-infrared $GeTe_4$ channel waveguides. Optics Letters. 2015;40(9):2016-9. doi:10.1364/OL.40.002016.
89. Morris JM, Mackenzie MD, Petersen CR, Demetriou G, Kar AK, Bang O et al. $Ge_{22}As_{20}Se_{58}$ glass ultrafast laser inscribed waveguides for mid-IR integrated optics. Opt Mater Express. 2018;8(4):1001-11. doi:10.1364/OME.8.001001.
90. Gutierrez-Arroyo A, Baudet E, Bodiou L, Lemaitre J, Hardy I, Faijan F et al. Optical characterization at 7.7 µm of an integrated platform based on chalcogenide waveguides for sensing applications in the mid-infrared. Opt Express. 2016;24(20):23109-17. doi:10.1364/OE.24.023109.
91. Gai X, Han T, Prasad A, Madden S, Choi D-Y, Wang R et al. Progress in optical waveguides fabricated from chalcogenide glasses. Opt Express. 2010;18(25):26635-46. doi:10.1364/OE.18.026635.
92. Vigreux C, Thi MV, Maulion G, Kribich R, Barillot M, Kirschner V et al. Wide-range transmitting chalcogenide films and development of micro-components for infrared integrated optics applications. Opt Mater Express. 2014;4(8):1617-31. doi:10.1364/OME.4.001617.
93. Shokooh-Saremi M, Ta'eed VG, Baker NJ, Littler ICM, Moss DJ, Eggleton BJ et al. High-performance Bragg gratings in chalcogenide rib waveguides written with a modified Sagnac interferometer. J Opt Soc Am B. 2006;23(7):1323-31. doi:10.1364/JOSAB.23.001323.
94. Saliminia A, Villeneuve A, Galstyan TV, LaRochelle S, Richardson K. First- and Second-Order Bragg Gratings in Single-Mode Planar Waveguides of Chalcogenide Glasses. Journal of Lightwave Technology. 1999;17(5):837.
95. Hu J, Carlie N, Petit L, Agarwal A, Richardson K, Kimerling L. Demonstration of chalcogenide glass racetrack microresonators. Optics letters. 2008;33(8):761-3.

96. Q. Du YH, J. Li, D. Kita, J. Michon, H. Lin, L. Li, S. Novak, K. Richardson, W. Zhang, and J. Hu. Low-loss photonic device in Ge-Sb-S chalcogenide glass. Optics Letters. 2016;41:3090-3.
97. Lin H, Li L, Zou Y, Danto S, Musgraves JD, Richardson K et al. Demonstration of high-Q mid-infrared chalcogenide glass-on-silicon resonators. Optics Letters. 2013;38(9):1470-2. doi:10.1364/OL.38.001470.
98. Ma P, Choi D-Y, Yu Y, Yang Z, Vu K, Nguyen T et al. High Q factor chalcogenide ring resonators for cavity-enhanced MIR spectroscopic sensing. Opt Express. 2015;23(15):19969-79. doi:10.1364/OE.23.019969.
99. Levy S, Klebanov M, Zadok A. High-Q ring resonators directly written in As_2S_3 chalcogenide glass films. Photon Res. 2015;3(3):63-7. doi:10.1364/PRJ.3.000063.
100. Choi JH, Cha D-H, Kim J-H, Kim H-J. Development of thermally stable and moldable chalcogenide glass for flexible infrared lenses. Journal of Materials Research. 2016;31(12):1674-80. doi:10.1557/jmr.2016.199.
101. Sanchez EA, Waldmann M, Arnold CB. Chalcogenide glass microlenses by inkjet printing. Appl Opt. 2011;50(14):1974-8. doi:10.1364/AO.50.001974.
102. Zhou W, Zhang L, Yi AY. Design and fabrication of a compound-eye system using precision molded chalcogenide glass freeform microlens arrays. Optik. 2018;171:294-303. doi:https://doi.org/10.1016/j.ijleo.2018.06.033.
103. Sachan P, Singh R, Dwivedi PK, Sharma A. Infrared microlenses and gratings of chalcogenide: confined self-organization in solution processed thin liquid films. RSC Advances. 2018;8(49):27946-55.
104. Zhou T, Zhu Z, Liu X, Liang Z, Wang X. A Review of the Precision Glass Molding of Chalcogenide Glass (ChG) for Infrared Optics. Micromachines. 2018;9(7):337.
105. DeCorby RG, Ponnampalam N, Nguyen HT, Clement TJ. Robust and Flexible Free-Standing All-Dielectric Omnidirectional Reflectors. Advanced Materials. 2007;19(2):193-6.
106. Kondakci HE, Yaman M, Koylu O, Dana A, Bayindir M. All-chalcogenide glass omnidirectional photonic band gap variable infrared filters. Applied Physics Letters. 2009;94(11):111110. doi:10.1063/1.3103279.
107. Wang J, Zens T, Hu J, Becla P, Kimerling LC, Agarwal AM. Monolithically integrated, resonant-cavity-enhanced dual-band mid-infrared photodetector on silicon. Applied Physics Letters. 2012;100(21):211106. doi:10.1063/1.4722917.
108. Kohoutek T, Orava J, Sawada T, Fudouzi H. Inverse opal photonic crystal of chalcogenide glass by solution processing. Journal of Colloid and Interface Science. 2011;353(2):454-8. doi:https://doi.org/10.1016/j.jcis.2010.10.011.
109. Freeman D, Madden S, Luther-Davies B. Fabrication of planar photonic crystals in a chalcogenide glass using a focused ion beam. Opt Express. 2005;13(8):3079-86. doi:10.1364/OPEX.13.003079.

110. Lin H, Li L, Deng F, Ni C, Danto S, Musgraves JD et al. Demonstration of mid-infrared waveguide photonic crystal cavities. Optics Letters. 2013;38(15):2779-82. doi:10.1364/OL.38.002779.
111. Zhang P, Zhao Z, Zeng J, Zhang Q, Wang X, Chen F et al. Fabrication and characterization of $Ge_{20}As_{20}Se_{15}Te_{45}$ chalcogenide glass for photonic crystal by nanoimprint lithography. Opt Mater Express. 2016;6(6):1853-60. doi:10.1364/OME.6.001853.
112. Hu J, Carlie N, Feng N-N, Petit L, Agarwal A, Richardson K et al. Planar waveguide-coupled, high-index-contrast, high-Q resonators in chalcogenide glass for sensing. Optics letters. 2008;33(21):2500-2.
113. Lin H, Li L, Deng F, Ni C, Danto S, Musgraves JD et al. Demonstration of mid-infrared waveguide photonic crystal cavities. 2013;38(15):2779-82.
114. Li L, Zou Y, Lin H, Hu J, Sun X, Feng N et al. A Fully-Integrated Flexible Photonic Platform for Chip-to-Chip Optical Interconnects. Journal of Lightwave Technology. 2013;31(24):4080-6. doi:10.1109/JLT.2013.2285382.
115. Li L, Lin H, Michon J, Huang Y, Li J, Du Q et al. A new twist on glass: A brittle material enabling flexible integrated photonics. International Journal of Applied Glass Science. 2016;8(1):61-8. doi:10.1111/ijag.12256.
116. Li L, Zhang P, Wang W-M, Lin H, Zerdoum AB, Geiger SJ et al. Foldable and cytocompatible sol-gel TiO 2 photonics. 2015;5:13832.
117. Collins A. Nanotechnology cookbook: practical, reliable and jargon-free experimental procedures. Elsevier; 2012.
118. Mata A, Fleischman AJ, Roy S. Characterization of polydimethylsiloxane (PDMS) properties for biomedical micro/nanosystems. Biomedical Microdevices. 2005;7(4):281-93. doi:10.1007/s10544-005-6070-2.
119. Cai D, Neyer A, Kuckuk R, Heise HM. Raman, mid-infrared, near-infrared and ultraviolet–visible spectroscopy of PDMS silicone rubber for characterization of polymer optical waveguide materials. Journal of Molecular Structure. 2010;976(1):274-81. doi:https://doi.org/10.1016/j.molstruc.2010.03.054.
120. Fuard D, Tzvetkova-Chevolleau T, Decossas S, Tracqui P, Schiavone P. Optimization of poly-di-methyl-siloxane (PDMS) substrates for studying cellular adhesion and motility. Microelectronic Engineering. 2008;85(5-6):1289-93.
121. Welch RC, Smith JR, Potuzak M, Guo X, Bowden BF, Kiczenski T et al. Dynamics of glass relaxation at room temperature. Physical review letters. 2013;110(26):265901.
122. Nemilov SV. Physical Ageing of Silicate Glasses at Room Temperature: General Regularities as a Basis for the Theory and the Possibility of a priori Calculation of the Ageing Rate. Glass Physics and Chemistry. 2000;26(6):511-30. doi:10.1023/A:1007168712556.
123. Priestley RD. Physical aging of confined glasses. Soft Matter. 2009;5(5):919-26. doi:10.1039/B816482G.

124. V Nemilov S. Structural relaxation in oxide glasses at room temperature. Physics and Chemistry of Glasses-European Journal of Glass Science and Technology Part B. 2007;48(4):291-5.
125. Joule JP. The Scientific Papers of Joule J.P. London Physical Society. 1884;1:558.
126. Phillips J. Microscopic theory of the Kohlrausch relaxation constant β_K. Journal of non-crystalline solids. 1994;172:98-103.
127. Phillips J. Stretched exponential relaxation in molecular and electronic glasses. Reports on Progress in Physics. 1996;59(9):1133.
128. Macdonald JR, Phillips JC. Topological derivation of shape exponents for stretched exponential relaxation. 2005;122(7):074510. doi:10.1063/1.1850901.
129. Phillips JC. Microscopic aspects of Stretched Exponential Relaxation (SER) in homogeneous molecular and network glasses and polymers. Journal of Non-Crystalline Solids. 2011;357(22):3853-65. doi:https://doi.org/10.1016/j.jnoncrysol.2011.08.001.
130. Lucas P. Energy landscape and photoinduced structural changes in chalcogenide glasses. Journal of Physics: Condensed Matter. 2006;18(24):5629.
131. Golovchak RY, Kozyukhin SA, Kozdras A, Shpotyuk OI, Novotortsev VM. Physical Aging of Chalcogenide Glasses. Inorganic Materials. 2010;46(8):1016-9.
132. Shpotyuk O, Kozdras A, Balitska V, Golovchak R. On the compositional diversity of physical aging kinetics in chalcogenide glasses. Journal of Non-Crystalline Solids. 2016;437:1-5.
133. Saiter J. Physical ageing in chalcogenide glasses. Journal of Optoelectronics and Advanced Materials. 2001;3(3):685-94.
134. Golovchak R, Kozdras A, Shpotyuk O. Optical signature of structural relaxation in glassy $As_{10}Se_{90}$. Journal of Non-Crystalline Solids. 2010;356(23):1149-52. doi:https://doi.org/10.1016/j.jnoncrysol.2010.04.008.
135. Choi D-Y, Madden S, Bulla D, Wang R, Rode A, Luther-Davies B. Thermal annealing of arsenic tri-sulphide thin film and its influence on device performance. Journal of Applied Physics Letters. 2010;107(5):053106.
136. Knotek P, Kutálek P, Vlasová M, Černošková E, Janíček P, Černošek Z et al. Ageing of $Ge_{24.9}Sb_{11.6}S_{63.5}$ thin films under various conditions. Materials Chemistry. 2017;195:236-46.
137. Mouawad O, Vitry P, Strutynski C, Picot-Clémente J, Désévédavy F, Gadret G et al. Atmospheric aging and surface degradation in As_2S_3 fibers in relation with suspended-core profile. Optical Materials. 2015;44:25-32. doi:https://doi.org/10.1016/j.optmat.2015.02.026.
138. Puri RK, Vijaya K, Karekar RN. Effect of minute's-scale aging on refractive index of chopped and non-chopped optical films. Pramana. 1983;21(5):311-22. doi:10.1007/BF02875536.

139. Zou Y, Lin H, Ogbuu O, Li L, Danto S, Novak S et al. Effect of annealing conditions on the physio-chemical properties of spin-coated As_2Se_3 chalcogenide glass films. Opt Mater Express. 2012;2(12):1723-32.
140. Churbanov M, Shiryaev V, Gerasimenko V, Pushkin A, Skripachev I, Snopatin G et al. Stability of the optical and mechanical properties of chalcogenide fibers. Inorganic materials. 2002;38(10):1063-8.
141. Richardson K, Lopez C, Schulte A, Rivero C, Saliminia A, Galstian T et al., editors. Aging Behavior of Photo-Induced As_2S_3 Gratings. Conference on Lasers and Electro-Optics; 2001: Optical Society of America.
142. Lubchenko V, Wolynes PG. Theory of aging in structural glasses. The Journal of chemical physics. 2004;121(7):2852-65.
143. Dyre JC. Source of non-Arrhenius average relaxation time in glass-forming liquids. Journal of Non-Crystalline Solids. 1998;235-237:142-9. doi:https://doi.org/10.1016/S0022-3093(98)00502-X.
144. Dyre JC. Heirs of liquid treasures. Nature Materials. 2004;3:749. doi:10.1038/nmat1247.
145. Saiter JM, Arnoult M, Grenet J. Very long physical ageing in inorganic polymers exemplified by the GexSe1−x vitreous system. Physica B: Condensed Matter. 2005;355(1):370-6. doi:https://doi.org/10.1016/j.physb.2004.11.057.
146. Golovchak R, Kovalskiy A, Shpotyuk O, Jain H. In search of energy landscape for network glasses. Applied Physics Letters. 2011;98(17):171905. doi:10.1063/1.3583531.
147. Hu J. Unpublished Results.
148. Åslund M, Canning J. Annealing properties of gratings written into UV-presensitized hydrogen-outdiffused optical fiber. Optics Letters. 2000;25(10):692-4. doi:10.1364/OL.25.000692.
149. Smith C, Jackson J, Petit L, Rivero-Baleine C, Richardson K. Processing and characterization of new oxy-sulfo-telluride glasses in the Ge–Sb–Te–S–O system. Journal of Solid State Chemistry. 2010;183(8):1891-9. doi:https://doi.org/10.1016/j.jssc.2010.06.009.
150. Ping C, Boolchand P, Georgiev DG. Long term aging of selenide glasses: evidence of sub-T_g endotherms and pre-T_g exotherms. Journal of Physics: Condensed Matter. 2010;22(6):065104.
151. Musgraves JD, Carlie N, Hu J, Petit L, Agarwal A, Kimerling LC et al. Comparison of the optical, thermal and structural properties of Ge–Sb–S thin films deposited using thermal evaporation and pulsed laser deposition techniques. Acta Materialia. 2011;59(12):5032-9. doi:https://doi.org/10.1016/j.actamat.2011.04.060.
152. Geiger S, Du Q, Huang B, Shalaginov MY, Michon J, Lin H et al. Understanding aging in chalcogenide glass thin films using precision resonant cavity refractometry. Opt Mater Express. 2019;9(5):2252-63. doi:10.1364/OME.9.002252.

153. Zhang L, Ding J, Zheng H, An S, Lin H, Zheng B et al. Ultra-thin high-efficiency mid-infrared transmissive Huygens meta-optics. Nature communications. 2018;9(1):1481.
154. Robinson JT, Preston K, Painter O, Lipson M. First-principle derivation of gain in high-index-contrast waveguides. Opt Express. 2008;16(21):16659-69. doi:10.1364/OE.16.016659.
155. Yang G, Jain H, Ganjoo A, Zhao D, Xu Y, Zeng H et al. A photo-stable chalcogenide glass. Opt Express. 2008;16(14):10565-71. doi:10.1364/OE.16.010565.
156. Tang HY, Wong WH, Pun EYB. Long period polymer waveguide grating device with positive temperature sensitivity. Applied Physics B. 2004;79(1):95-8. doi:10.1007/s00340-004-1489-3.
157. Lin H, Song Y, Huang Y, Kita D, Deckoff-Jones S, Wang K et al. Chalcogenide glass-on-graphene photonics. Nature Photonics. 2017;11(12):798.
158. Toyjanova J, Bar-Kochba E, Lopez-Fagundo C, Reichner J, Hoffman-Kim D, Franck C. High resolution, large deformation 3D traction force microscopy. PLoS One. 2014;9(4):e90976. doi:10.1371/journal.pone.0090976.
159. Legant WR, Pathak A, Yang MT, Deshpande VS, McMeeking RM, Chen CSJPotNAoS. Microfabricated tissue gauges to measure and manipulate forces from 3D microtissues. 2009;106(25):10097-102.
160. Halir R, Bock PJ, Cheben P, Ortega-Monux A, Alonso-Ramos C, Schmid JH et al. Waveguide sub-wavelength structures: a review of principles and applications. Laser & Photonics Reviews. 2015;9(1):25-49. doi:10.1002/lpor.201400083.
161. Bloch F. Über die quantenmechanik der elektronen in kristallgittern. Zeitschrift für physik. 1929;52(7-8):555-600.
162. Gan X, Clevenson H, Englund D. Polymer Photonic Crystal Nanocavity for Precision Strain Sensing. ACS Photonics. 2017;4(7):1591-4. doi:10.1021/acsphotonics.7b00030.
163. Tung BT, Dao DV, Ikeda T, Kanamori Y, Hane K, Sugiyama S. Investigation of strain sensing effect in modified single-defect photonic crystal nanocavity. Opt Express. 2011;19(9):8821-9. doi:10.1364/OE.19.008821.
164. Quan Q, Deotare PB, Loncar M. Photonic crystal nanobeam cavity strongly coupled to the feeding waveguide. Applied Physics Letters. 2010;96(20):203102.
165. Hauck T, Müller W, editors. Large deformation of beam columns-a closed form solution and design guide for vertical buckling probe needles. 2010 11th International Thermal, Mechanical & Multi-Physics Simulation, and Experiments in Microelectronics and Microsystems (EuroSimE); 2010: IEEE.
166. Takahashi H, Suzuki S, Kato K, Nishi I. Arrayed-waveguide grating for wavelength division multi/demultiplexer with nanometre resolution. Electronics letters. 1990;26(2):87-8.
167. Takahashi H, Oda K, Toba H, Inoue Y. Transmission characteristics of arrayed waveguide N/spl times/N wavelength multiplexer. Journal of Lightwave Technology. 1995;13(3):447-55.

168. Weinberger F, Mannhardt I, Eschenhagen T. Engineering Cardiac Muscle Tissue. 2017;120(9):1487-500. doi:doi:10.1161/CIRCRESAHA.117.310738.
169. Akhyari P, Fedak PW, Weisel RD, Lee T-YJ, Verma S, Mickle DA et al. Mechanical stretch regimen enhances the formation of bioengineered autologous cardiac muscle grafts. 2002;106(12_suppl_1):I-137-I-42.
170. Eschenhagen T, Fink C, Remmers U, Scholz H, Wattchow J, Weil J et al. Three-dimensional reconstitution of embryonic cardiomyocytes in a collagen matrix: a new heart muscle model system. The FASEB journal. 1997;11(8):683-94.
171. Radisic M, Yang L, Boublik J, Cohen RJ, Langer R, Freed LE et al. Medium perfusion enables engineering of compact and contractile cardiac tissue. 2004;286(2):H507-H16. doi:10.1152/ajpheart.00171.2003.
172. Carrier RL, Rupnick M, Langer R, Schoen FJ, Freed LE, Vunjak-Novakovic GJTe. Perfusion improves tissue architecture of engineered cardiac muscle. 2002;8(2):175-88.
173. Pimentel CR, Ko SK, Caviglia C, Wolff A, Emneus J, Keller SS et al. Three-dimensional fabrication of thick and densely populated soft constructs with complex and actively perfused channel network. Acta Biomater. 2018;65:174-84. doi:10.1016/j.actbio.2017.10.047.
174. Griffith CK, Miller C, Sainson RC, Calvert JW, Jeon NL, Hughes CC et al. Diffusion limits of an in vitro thick prevascularized tissue. 2005;11(1-2):257-66.
175. Issa RI, Engebretson B, Rustom L, McFetridge PS, Sikavitsas VI. The effect of cell seeding density on the cellular and mechanical properties of a mechanostimulated tissue-engineered tendon. Tissue Eng Part A. 2011;17(11-12):1479-87. doi:10.1089/ten.TEA.2010.0484.
176. Sadeghi AH, Shin SR, Deddens JC, Fratta G, Mandla S, Yazdi IK et al. Engineered 3D Cardiac Fibrotic Tissue to Study Fibrotic Remodeling. Adv Healthc Mater. 2017;6(11). doi:10.1002/adhm.201601434.
177. Galie PA, Stegemann JP. Simultaneous application of interstitial flow and cyclic mechanical strain to a three-dimensional cell-seeded hydrogel. Tissue Eng Part C Methods. 2011;17(5):527-36. doi:10.1089/ten.TEC.2010.0547.
178. Galie PA, Russell MW, Westfall MV, Stegemann JP. Interstitial fluid flow and cyclic strain differentially regulate cardiac fibroblast activation via AT1R and TGF-beta1. Exp Cell Res. 2012;318(1):75-84. doi:10.1016/j.yexcr.2011.10.008.
179. Kensah G, Gruh I, Viering J, Schumann H, Dahlmann J, Meyer H et al. A novel miniaturized multimodal bioreactor for continuous in situ assessment of bioartificial cardiac tissue during stimulation and maturation. 2011;17(4):463-73.
180. Mabry KM, Lawrence RL, Anseth KS. Dynamic stiffening of poly(ethylene glycol)-based hydrogels to direct valvular interstitial cell phenotype in a three-dimensional environment. Biomaterials. 2015;49:47-56. doi:10.1016/j.biomaterials.2015.01.047.
181. Eagle HJS. Buffer combinations for mammalian cell culture. 1971;174(4008):500-3.

182. Roca-Cusachs P, Conte V, Trepat X. Quantifying forces in cell biology. Nature cell biology. 2017;19(7):742.
183. Polacheck WJ, Chen CS. Measuring cell-generated forces: a guide to the available tools. Nature methods. 2016;13(5):415.
184. Oliver T, Jacobson K, Dembo MJCm, cytoskeleton t. Traction forces in locomoting cells. 1995;31(3):225-40.
185. Franck C, Maskarinec SA, Tirrell DA, Ravichandran G. Three-dimensional traction force microscopy: a new tool for quantifying cell-matrix interactions. PLoS One. 2011;6(3):e17833. doi:10.1371/journal.pone.0017833.

Appendix A

COPYRIGHT PERMISSIONS

Work presented in Chapter 4 has been published in:
Sarah Geiger, Qingyang Du, Bin Huang, Mikhail Y. Shalaginov, Jérôme Michon, Hongtao Lin, Tian Gu, Anupama Yadav, Kathleen A. Richardson, Xinqiao Jia, and Juejun Hu, "Understanding aging in chalcogenide glass thin films using precision resonant cavity refractometry," Opt. Mater. Express 9, 2252-2263 (2019)

Work presented in Section 3.2.2 has been published in:
Li, L. *et al.* Foldable and Cytocompatible Sol-gel TiO_2 Photonics. *Sci. Rep.* **5**, 13832; doi: 10.1038/srep13832 (2015).

Dear Sarah Geiger,

Thank you from contacting The Optical Society.

For the use of material from Sarah Geiger, Qingyang Du, Bin Huang, Mikhail Y. Shalaginov, Jérôme Michon, Hongtao Lin, Tian Gu, Anupama Yadav, Kathleen A. Richardson, Xinqiao Jia, and Juejun Hu, "Understanding aging in chalcogenide glass thin films using precision resonant cavity refractometry," Opt. Mater. Express 9, 2252-2263 (2019):

> Because you are the author of the source paper from which you wish to reproduce material, OSA considers your requested use of its copyrighted materials to be permissible within the author rights granted in the Copyright Transfer Agreement submitted by the requester on acceptance for publication of his/her manuscript. It is requested that a complete citation of the original material be included in any publication. This permission assumes that the material was not reproduced from another source when published in the original publication.

While your publisher should be able to provide additional guidance, OSA prefers the below citation formats:

> For citations in figure captions:
>
> [Reprinted/Adapted] with permission from ref [x], [Publisher]. (with full citation in reference list)
>
> For images without captions:
>
> Journal Vol. #, first page (year published) An example: Opt. Mater. Express 9, 2252 (2019)

Please let me know if you have any questions.

Kind Regards,

Rebecca Robinson

Rebecca Robinson
May 28, 2019
Authorized Agent, The Optical Society

The Optical Society (OSA)
2010 Massachusetts Ave., NW
Washington, DC 20036 USA
www.osa.org

Reflecting a Century of Innovation

Open access

Scientific Reports is an open access journal. Articles in the journal are free to access, download, share, and re-use.

Creative Commons Licenses

Scientific Reports articles are published open access under a CC BY license (Creative Commons Attribution 4.0 International License). The CC BY license allows for maximum dissemination and re-use of open access materials and is preferred by many research funding bodies. Under this license users are free to share (copy, distribute and transmit) and remix (adapt) the contribution including for commercial purposes, providing they attribute the contribution in the manner specified by the author or licensor (read full legal code).

In the past, some papers were published under a non-commercial license. Users may request permission to use the works for commercial purposes or to create derivative works by emailing permissions@nature.com.

Under Creative Commons, authors retain copyright in their articles.

Visit our open research site for more information about Creative Commons licensing.

Appendix B

FABRICATION SUMMARY

A silicon wafer with 3 μm oxide was cleaned, and the undercladding of 2 μm SU8 2002 was spin coated and then soft baked with a ramped bake of 1 minute at 60°C, 1 minute at 95°C, followed by an additional minute at 60°C. The resist is then patterned with a photomask and exposed at 100 mJ/cm^2 with an MA-4 photolithography system, and post-exposure baked with a ramped bake of 1 minute at 60°C, 2 minutes at 95°C, and then an additional minute at 60°C.

In order to later be able to align the Ebeam patterning of the waveguides to the thick, insulating SU-8 undercladding, droplets of 100 nm diameter gold nanoparticles were then deposited on the corners of the SU-8 undercladding layer. GSS is then deposited to 450 nm thickness via thermal evaporation with a PVD system dedicated to chalcogenide glasses. Deposition occurs at a base pressure of 5x10^{-6} Torr, with deposition rate 10-15 Å/s. These deposition conditions have been used extensively in our research group in order to achieve high quality thin film devices.

Ebeam lithography and fluorine-based ICP etching is used to define the waveguides. To improve adhesion of the Ebeam resist to the glass, the chip was exposed to 1 minute of oxygen plasma at 100W, 100 Torr. For efficient write times and compatibility with the device stack, SU8-2000.2 was initially chosen as the Ebeam resist used to define the location of the waveguide, however after extensive optimization, it was verified that this technique was not reproducible. The final

lithography process modified an established positive Ebeam resist (ZEP 520A) protocol. Prior to Ebeam resist deposition, a negative resist AZ P4110 was deposited at 1.2 μm thick, baked at 95°C for one minute, and patterned with the mask aligner at 110 mJ/cm^2. This resist could be applied as either a liftoff resist before glass deposition, or a protective resist during RIE. Here I describe its use as a protective layer for an RIE etch step.

In this step, the lower resolution AZ resist is patterned to protect bulk regions of glass where the waveguides are later defined with Ebeam resist. The glass around the edges of the patterned undercladding is left exposed and then removed with RIE. The following RIE conditions for GSS on a Cobra ICP system were optimized for low sidewall roughness of the waveguides: CHF_3/Ar 15/35 sccm, 5 mTorr, 300 W ICP power, 60 W HF power. The excess AZ resist was removed with acetone, and high-resolution ZEP 520A Ebeam resist is deposited, baked at 180°C, and then patterned with 2000 μC/cm^2 exposure dose to define the device location. After RIE of the exposed glass, the ZEP was stripped with NMP and the device cladding layers were patterned in SU-8 2002 as previously described. Figure 21 shows a schematic of this processing procedure.

Appendix C

DERIVATION OF SENSITIVITY RELATIONSHIP

The strain energy (W_s) over the buckle segment defined in Figure 21 can be calculated as:

$$W_S = \int_0^t \frac{1}{2} E_{clad} \left(\frac{x}{R}\right)^2 Lwdx = \frac{E_b Lwt^3}{24R^2} \tag{C.1}$$

Here E_{clad} is the modulus of the device cladding material, x the span of the buckled strip, R the radius of curvature of the segment, L the length of the segment, and w with width of the strip. The force applied to one end of the buckle that gives it its radius of curvature is:

$$F_{applied} = \frac{dW_S}{dL_a} = \frac{dW_S}{dR} \cdot \frac{dR}{dL_A} \tag{C.2}$$

Where dL_A/dR, the change in span of the buckle, can be calculated as:

$$L_A = 2R \sin\left(\frac{\theta}{2}\right) = 2R \sin\left(\frac{L}{2R}\right) \tag{C.3}$$

$$\frac{dL_A}{dR} = -\frac{L}{R} \cos\left(\frac{L}{2R}\right) + 2 \sin\left(\frac{L}{2R}\right) \tag{C.4}$$

Substituting C.4 and the derivative of C.1 into C.2:

$$F_{applied} = \frac{-E_b Lwt^3}{12R^3[-\frac{L}{R}\cos\left(\frac{L}{2R}\right)+2\sin\left(\frac{L}{2R}\right)]} \tag{C.5}$$

In order to determine the minimum detectable force that changes the radius of curvature of the buckled strip. First, we can rewrite equation (17) to solve for the bending radius:

$$R = \frac{y}{\varepsilon} \tag{C.6}$$

Which can be related to the relationship between peak shift and bending strain experimentally determined in Section 6.2.2:

$$\Delta\varepsilon = \frac{\Delta\lambda}{\alpha} \rightarrow \Delta R = \frac{y}{\Delta\varepsilon} = \frac{y\alpha}{\Delta\lambda} \tag{C.7}$$

Selecting a system in which $L \approx L_A \approx 1\ mm$ for simplicity, the force on the buckle can be approximated:

$$F \approx \frac{E_b w t^3}{L^2} \tag{C.8}$$

As can C.4:

$$\frac{dL_A}{dR} \approx -L^3/12R^3 \tag{C.9}$$

And the change in F with radius:

$$\frac{dF}{dR} \approx -\frac{E_b w t^3}{10R^3} \tag{C.10}$$

The force applied to the buckle as a result of a change in curvature ($\kappa = \frac{1}{R}$) is then:

$$\Delta F_{bend} = \frac{dF}{d\kappa} \cdot \Delta\kappa = \frac{dF}{dR} \cdot (-R^2) \cdot \Delta\kappa = \frac{E_b w t^3}{10R} \cdot \frac{\Delta\lambda}{\alpha\delta} \tag{C.11}$$

And finally to an increase in strain in the matrix:

$$\Delta\epsilon_{matrix} = \frac{\Delta F_{buckle}}{A \cdot E_m} = \frac{4}{5}\frac{t^3}{\delta L^2} \cdot \frac{E_{buckle}}{E_{matrix}} \cdot \frac{\Delta\lambda}{\alpha} \tag{I. 16}$$

In order to determine the minimum modulus of gel that can efficiently transfer force to the = buckle as the gel experiences strain $\epsilon_{matrix} = \Delta L_A / L_A$ we can calculate:

$$\Delta F_{buckle} = \frac{dF}{dR} \cdot \frac{dR}{dL_A} \cdot L_A \epsilon_{matrix} \approx -\frac{6E_b w t^3}{5L^2} \cdot \epsilon_{matrix} \tag{C.11}$$

The force transferred from the gel to the buckle is:

$$\Delta F_{matrix} = A \cdot E_{matrix} \cdot \epsilon_{matrix} \tag{C.12}$$

Where A, the area of the gel under the buckle is:

$$A = w \cdot R\left[1 - \cos\left(\frac{L}{2R}\right)\right] \approx wL^2/8R \tag{C.13}$$

And the modulus of the gel capable of transferring force to the buckle is:

$$E_{matrix} \geq \frac{48}{5}\frac{Rt^3}{L^4}E_{buckle} \tag{C.14}$$